Influences of Meteoric Aerosol Particles on the lower Ionosphere

Carsten Baumann

München 2016

Influences of Meteoric Aerosol Particles on the lower Ionosphere

Carsten Baumann

Dissertation
an der Fakultät für Physik
der Ludwig–Maximilians–Universität
München

vorgelegt von
Carsten Baumann
aus Grevesmühlen

München, den 24.10. 2016

Erstgutachter: Prof. Markus Rapp
Zweitgutachter: Prof. Jörg Gumbel
Tag der mündlichen Prüfung: 19.12. 2016

Zusammenfassung

Die Erde ist einem permanenten Beschuss durch Meteoroide ausgesetzt. Man nimmt an, dass diese Meteoroiden zwischen 10 und 100 t an extraterrestrischem Material pro Tag in die Atmosphäre eintragen, wenn sie in einer Höhe von 80 bis 110 km verdampfen. Das verdampfte Material reagiert mit der umgebenden Atmosphäre und kann daraufhin zu neuen Aerosolpartikeln rekondensieren, sogenannte Meteorstaubpartikel (MSP). Die MSP befinden sich im gleichen Höhenbereich wie die D-Schicht Ionosphäre. In dieser Umgebung sind verschiedenste MSP-Ladungs-Prozesse möglich. Darunter sind beispielsweise der Einfang von Elektronen durch neutrale MSP und das Elektronen-Photodetachment von negativ geladener MSP. Auch ist die Emission von Sekundär-Elektronen von MSP, hervorgerufen durch Niederschlag energetischer Elektronen aus der Magnetosphäre, ein möglicher Ladungs-Prozess in polaren Breiten.

Das Ziel dieser Arbeit ist die Untersuchung inwieweit diese Aufladungsprozesse der MSP den Zustand der D-Schicht ändern. Jüngste in-situ Untersuchungen der Ladungsbilanz in der D-Schicht zeigen, dass negativ geladene MSP vor allem nachts eine wichtige Rolle spielen. Diese Experimente stellen den Startpunkt für Modell-Studien der Ladungsbilanz und kompletten Ionenchemie der D-Schicht dar. Dazu wurden MSP Größenverteilungen für den Höhenbereich von 50 bis 100 km in das Ionen Reaktionsschema des Sodankylä Ion and Neutral Chemistry (SIC) Modell eingebaut. Die Modellergebnisse zeigen, dass insbesondere der Einfluss von MSP auf die freie Elektronendichte die Ionen Zusammensetzung der D-Schicht verändert. In der Nacht werden freie Elektronen besonders gut durch MSP eingefangen, was in einer reduzierten Elektronen-Ionen Rekombinationsrate resultiert. Dadurch wird einer der wichtigsten Verlustprozesse, vor allem von positiven Wassercluster-Ionen, stark unterdrückt. Infolgedessen können diese Wassercluster-Ionen in Anzahl und Größe anwachsen. Am Tage kann solare Strahlung die negativ geladenen MSP durch Photodetachment entladen. Dadurch gibt es während Sonnenschein weniger negativ geladene MSP als während Dunkelheit. Bei der Untersuchung des Tagesganges der Elektronendichte zeigen sich ein plötzlicher Abfall während des Sonnenunterganges und ein plötzlicher Anstieg während des Sonnenaufganges, hervorgerufen durch Aus- bzw. Einsetzen des Elektronen-Photodetachments negativ geladener MSP. Der Einfang von Ionen durch MSP ist nur bei langlebigen Ionen ein relevanter Verlustprozess. Der Einfluss von MSP auf die Ionenchemie hat auch Auswirkung auf die Komposition der neutralen Atmosphäre, ebenfalls vor allem nachts. Besonders die Spurengase des reaktiven Wasserstoffs und Stickstoffs werden durch MSP indirekt beeinflusst. Diese Spurengase können durch Reaktionen mit Ionen, die durch MSP beeinflusst sind, in verschiedenen Höhen mehr oder auch weniger zahlreich vorkommen.

Abstract

The Earth atmosphere is subject to a permanent bombardment by meteoroids which are supposed to inject extraterrestrial material into the Earth atmosphere in the order of 10 to 100 t per day when they evaporate between 80 and 110 km. The evaporated material reacts with the ambient atmosphere and recondensates into new nanometer-sized aerosol particles, so called Meteoric Smoke Particles (MSPs). The layer of MSPs coincides with the D-region ionosphere of the Earth. Here, MSPs are subject to different kinds of charging processes. Among these are, for example, the attachment of free electrons or ions to the surface of MSP and the photodetachment of electrons from negatively charged MSPs. Even secondary electron emission induced by energetic electron precipitation from within the magnetosphere is possible at polar latitudes.

The aim of this thesis is to investigate how these charging processes of MSPs change the nature of the background D-region. Recent in-situ studies of the nighttime charge balance of the D-region indicate negatively charged MSPs to play a significant role. These experiments have been the starting point for modeling studies of not only the D-region charge balance but also the overall ion chemistry of the D-region. This has been accomplished by implementing a MSP size distribution for a altitude region between 50 and 100 km into the ion reaction scheme of the Sodankylä Ion and Neutral Chemistry (SIC) model. The results show, that especially the influence of MSPs on the electron density is important to characterize the D-region ion composition. During nighttime, electrons are effectively attached to the surface of MSPs resulting in reduced electron-ion recombination. Thus, the main loss process of positive water cluster ions nearly vanishes and these ions can grow to higher numbers of water ligands and also increase in number density. The capture of ions by MSPs is a significant loss process for long-lived ions only. During daytime, solar photons effectively photodetach electrons from the negatively charged MSPs. This results in a lower abundance of negatively charged MSPs during sunlit conditions. When investigating the diurnal variation of the electron density, there is a sudden drop in electron density during sunset and a sudden increase during sunrise due to the absence of/sudden onset of effective photodetachment of electrons from negative MSPs. The influence of MSPs on the ion chemistry also affects the neutral background composition through ion-neutral reactions. Especially reactive hydrogen and reactive nitrogen are affected. E.g., there are reduced abundances of reactive hydrogen at 60 km altitude and of reactive nitrogen ($N/N(^2D)$) at 90 km. Similar to the ion chemistry, MSP affect the neutral composition mainly during nighttime.

Contents

1 Introduction

The start of ionospheric research is marked by the 12th December 1901, when Guglielmo Marconi established the first trans-atlantic radio transmission from Cornwall to Newfoundland. During experiments with a mobile receiver onboard the USS Philadelphia, Marconi (1902) identified diurnal variations in received signal power. He detected strong signals in the morning and rather disturbed signals during nighttime. Marconi's experiments gave rise to theories of Kennelly (1902) and Heaviside (1902) to explain these long range telegraphy experiments. They postulated the existence of a conducting layer at which the radio waves would reflect before their detection at the receiving site. This conducting layer was named after them as the Kenelly-Heaviside layer. Already in 1909, Marconi and Ferdinand Braun were rewarded with the Nobel Prize in Physics for their contributions to wireless telegraphy.

The ionospheric research took a leap as Appleton and Barnett (1925) experimentally verified the existence of this conducting layer. They interpreted the diurnal variation of signal strength in long range telegraphy by interference of two radio waves, one direct radio wave and a reflected radio wave from the ionosphere. The reflected wave travels a certain longer way then the direct wave and their difference has to be an integral multiple of the wavelength in order to receive a strong signal. By variation of the radio wavelength the altitude of the conducting layer was determined to be around 80 km. In consecutive studies Appleton discovered also a higher and a lower ionospheric layer and introduced a nomenclature which is still used today. That is the D-region ionosphere between 60–90 km, the E-region between 90–150 km and the F-region between 150–400 km. These contributions to the understanding of the ionosphere were recognized with the Nobel Prize in Physics in 1947.

The most important property of the ionosphere is the amount of free electrons which can exist. The electron number density of the ionosphere has a distinct diurnal cycle, especially the electrons of the D- and E-region nearly vanish during nighttime. A mathematical description for the shape of ionospheric regions is given by Chapman (1931a,b). He pointed out that monochromatic light of certain wavelengths is the source of each ionospheric region. In case of the D-region, this is the solar Ly-α line at 121,6 nm which can penetrate deep into the Earth's atmosphere due to a local minimum in the O_2 absorption spectrum. Here, the solar photons have enough energy to ionize atmospheric nitric oxide and give rise to the free electrons of the D-region. NO^+ is also the most abundant positive ion within the lower ionosphere.

The current understanding of the nature and ionic composition of the D-region originates from Nicolet and Aikin (1960) who indicated that the D-region is highly variable due its direct link to the solar activity. This work motivated rocket-borne mass spectrometric

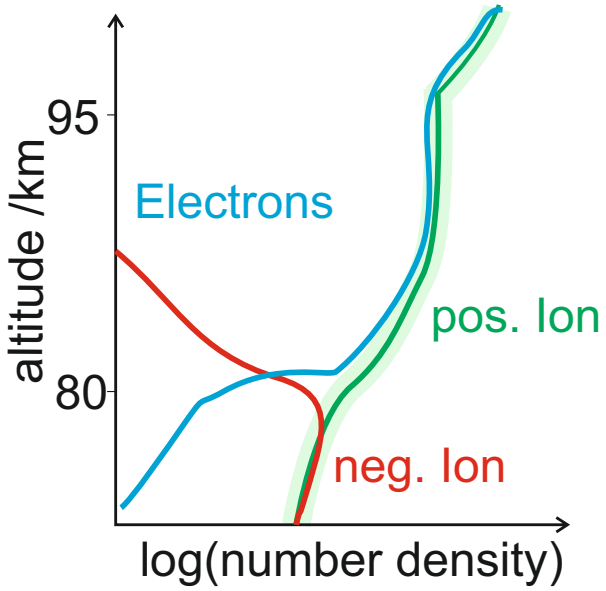

Figure 1.1: State of the lower ionosphere as it is supposed after Nicolet and Aikin (1960) and successive studies.

investigations of the D-region (e.g., Narcisi and Bailey, 1965; Arnold et al., 1977) which verify the existence of a large number of different ions.

Figure 1.1 shows a schematic of the D-region ionosphere with the three components free electrons, positive and negative ions. One specific feature of the D-region is the possibility that free electrons can attach to neutral atmospheric components and form negative ions. This process, however, is inhibited if atomic oxygen exists as it effectively collisional detaches electrons from neagtive ions (Fehsenfeld et al., 1966). The altitude region where atomic oxygen starts to be abundant enough to act as a negative ion sink is around 80 km and is usually called atomic oxygen 'ledge'. Above 80 km atomic oxygen is effectively produced by the photodissociation of ozone. As a result, there are no negative ions present above this altitude and only positive ions and free electrons exist. Below 80 km, the free electrons are more and more removed by attaching to neutral components to form negative ions. In general, the attachment of electrons to small particles, so called aerosol particles, can be an additional sink for free electrons too (Natanson, 1960; Rapp, 2000). The following paragraphs show in short, how this can also happen in Earth's D-region.

Already Benzenberg and Brandes (1800) found meteors, visible as shooting stars, to occur at 10.2-12.9 Prussian miles above ground, corresponding to 80–100 km, above the Earth surface. Their measurements were based on bistatic optical observations of the point where shooting stars vanished. Furthermore, devices using the method of RAdio Detection And Ranging (Radar) experienced a golden age after the discovery of Marconi. Radars are powerful tools for remote sensing of the atmosphere and they can also be used to detect the trails of meteors (e.g., McKinley, 1961). Relying on these radar and optical methods to detect meteors, it can be assessed that material in the order of 10–100 t per

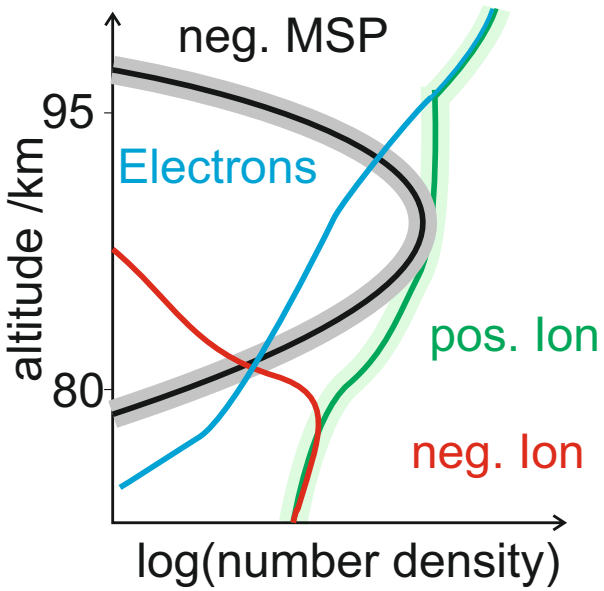

Figure 1.2: State of the D-region during nighttime after Friedrich et al. (2012) with negatively charged MSP conserving the charge balance together with positive ions between 85 and 95 km.

day is injected into an altitude region of the atmosphere (e.g., Ceplecha et al., 1998; Plane, 2012) which coincides with the D-region ionosphere. That gave rise to the assumption of Rosinski and Snow (1961) that this material can be processed within the atmosphere to form so called secondary particulate matter. Successive studies included the quantitative modelling (Hunten et al., 1980) as well as initial in-situ evidence of these particles by means of mass spectrometric measurements (Schulte and Arnold, 1992) of large cluster ions. However, a direct influence of these MSPs on the D-region ionosphere has not been proved until the study of Friedrich et al. (2012). They brought measurements of charged MSPs together with positive ion number density and free electron number density onboard the same sounding rocket. Their findings are shown by a schematic within Fig. 1.2.

Friedrich et al. (2012) actually found, that due to a lack of free electrons, the charge balance cannot be preserved by positive ions and free electrons alone. They expect negatively charged MSP to be the other negative charge carrier and explicitly not negative ions as they are effectively destroyed by the atomic oxygen above 80 km as demonstrated by dedicated rocketborne in-situ experiments (Plane et al., 2014). Different to the D-region depicted in Fig. 1.1, Fig. 1.2 also includes negatively charged MSPs between 80 and 95 km. Here, the free electrons have been scavenged by the present MSPs to form a layer of negatively charged MSPs. Therefore, the charge balance in this altitude region is preserved by positive ions and negative MSPs rather than free electrons. This is at least the case during nighttime as no significant ionization source is present and the free electron number density is relatively low.

1.1 Hypothesis and Outline

Based on the findings of Friedrich et al. (2012) the following hypothesis can be formulated which will be investigated within this thesis:

> Meteoric smoke particles exist within the D-region ionosphere and can be charged by different ionospheric processes. They have an effect on the D-region charge balance. Therefore also the nature of the D-region ion chemistry is different from its previously expected state.

In order to approach the above stated hypothesis, this dissertation has been structured into six chapters. After the introduction in Chapter 1, the other chapters have the following content.

Chapter 2 contains a review of the MSP formation process together with modeling results of their global abundance. The chapter also reviews experimental evidence of the MSP existence at D-region altitudes.

Chapter 3 introduces all charging mechanisms that MSPs are subject to. This also includes a study of secondary electron emission from MSP during electron precipitation.

Chapter 4 investigates the experimental results of Friedrich et al. (2012) using a model approach. It is shown that a simplified ionospheric model with MSPs as active ionospheric components can qualitatively verify the assumption that negatively charged MSP play a significant role in the nightly charge balance.

In Chapter 5, MSPs are implemented into the Sodankylä Ion and Neutral chemistry model. By doing so the influence of MSPs on the lower ionosphere is assessed not only for a single time but for the full diurnal cycle. A detailed study of the ion chemistry differences due to the presence of MSPs is presented in this section. Finally, in addition to the direct influence on ions, an indirect MSP effect on neutral trace gases is discussed in this chapter.

In Chapter 6, a summary of this work is given. This includes a statement to which extent the hypothesis has been verified. In addition, an outlook is given to follow up studies which emerge from the results of this thesis.

2 Meteor smoke particles in Earth's atmosphere

The Earth is constantly hit by meteoroids from within the solar system, which have generally two different origins. Firstly, shower meteors, comet remnants dispersed in a dust cloud intersect the Earth orbit annually. Secondly, sporadic meteors, asteroid remnants from the asteroid belt between Mars and Jupiter are a continuous source of meteorids. The asteroids collide and generate fragments which are gravitationally disturbed to reach the Earth orbit. Love and Brownlee (1993) used a clever way to determine the so-called terrestrial mass accretion rate, the mass flux of meteorides hitting the Earth. They counted craters on a satellite which originated from impacting micrometeors for a time period of six years. In addition, the analyzed satellite surface was oriented during the satellite mission in many different directions pointing into space. Therefore, it was possible to determine a directional averaged mass accretion rate directly. By deriving the meteoroid mass from the measured crater sizes and depths and using a mean impact velocity of 16.9 km/s, they were able to determine the terrestrial mass accretion rate to be ∼110 t per day. However, there are many different studies on the determination of this rate (e.g., Cziczo et al., 2001; Gabrielli et al., 2004). The mass influx of extraterrestrial material into the Earth atmosphere needs to be integrated from meteoroid events of reasonable occurence rate. Rare events of extremely heavy meteoroids impacting Earth increase this influx substantially but taking them into account for atmospheric science is not useful. That is, because big meteoroids deposit only a small fraction of their mass into the atmosphere and the events occur on timescales greater than one per year. An intelligible review on the mass influx into the Earth's atmosphere is given by Plane (2012).

When meteoroids enter the atmosphere they are heated by collision with atmospheric molecules and start to vaporize at temperatures around 2500 K (Ceplecha et al., 1998). The size and speed of the meteoroid determines whether complete disintegration occurs or remnants can reach the Earth's surface. Therefore, it is also important to know what fraction of this meteoroid mass influx is deposited into the Earth's atmosphere rather than impacting the surface. For that question lidar (light detection and ranging) studies are state of the art, as they can relate measured metal layers in the middle atmosphere to a meteoroid mass influx deposited into that altitude region. A study from Gardner et al. (2014) used a sodium lidar to determine the extraterrestrial mass influx to be 60 t per day into the Mesosphere/Lower Thermosphere (MLT). This study uses a global model of the sodium distribution to constrain the mass influx from these lidar measurements (Plane, 2004; Marsh et al., 2013). There is also effort made to determine how the mass influx is distributed over the globe and its diurnal and seasonal variation. This is can be done

by means of radar measurements, as characteristics of individual meteor phenomena can be detected and the meteor events can be related to different meteoroid source regions (Fentzke and Janches, 2008). The recent review of Plane et al. (2015) gives an overview over the ablation mechanisms of extraterrestrial material into Earth's atmosphere, the different metals injected and their behaviour within the dynamic MLT region.

The dispersion of meteoric matter within the Earth atmosphere and its deposition on the Earth surface is not yet fully understood. There are reports of meteoric matter found in ice cores from Greenland and Antarctica (e.g., Gabrielli et al., 2004), but how it got there and why the deposited amount changes with geographical location is not thoroughly understood. Dhomse et al. (2013) tried to shed light onto this diverse problem by analyzing the deposition of ^{238}Pu after a satellite failed to reach its orbital velocity and disintegrated in 1964. With the help of ground deposition measurements of this unique isotope on the Earth's surface, a chemistry-climate model has been validated in order to reproduce the measured geographical distribution of this fallout event. This model was then used to determine the dispersion of MSPs injected at higher altitudes. The authors concluded that the measured deposition of meteoric matter within ice cores can be reproduced, but the used meteor mass influx rate is too high in order to represent the metal layers in the MLT region.

Direct detection of particles from metoric origin within the atmosphere is ambitious. There are various balloon-borne and air-borne sampling experiments which were able to collect particles with sizes around one micrometer. Rietmeijer et al. (2016) found μm particles at 38 km altitude and analyzed them using electron microscopy and X-ray dispersion analysis to gather information about the particle composition. They found the particles to consist of oxides of metals and silicon, which are present in meteoroid bodies as well as in mesospheric metal layers. Additionally, they found metal remnants of meteor fragmentation events of bigger meteors (so-called bolides and fireballs). Particle instruments mounted onboard of the M55-Geophysica, a research aircraft, detected also particles with optical properties which exclude sulfuric aerosol or stratospheric ice particles (Weigel et al., 2014). These particles where sampled at 20 km altitude using a condensation particle counter. Weigel et al. (2014) detected a particle size distribution in the sub micron regime and concluded that these particles are supposed to be meteoric smoke particles (MSPs).

There are generally two different hypotheses on the origin of meteoric smoke particles in the stratosphere: On the one hand, the atmospheric science community follow the theory of Rosinski and Snow (1961), where most meteors disintegrate fully and evaporated meteoric material is processed by the atmosphere and recondensates into new particles. On the other hand, the astrophysics community rather follows the explanation that meteors also fragment during atmospheric entry and these fragments are the source of stratospheric as well as mesospheric aerosol particles of meteoric origin.

This chapter aims at reviewing the MSP formation concept of Rosinski and Snow (1961) and the current understanding of MSP dispersion within Earth's atmosphere in Sect. 2.1. In addition, the different experiments which prove the existence of MSPs in the mesosphere and lower thermosphere region, which coincides with the lower ionosphere, are discussed in Sect. 2.2.

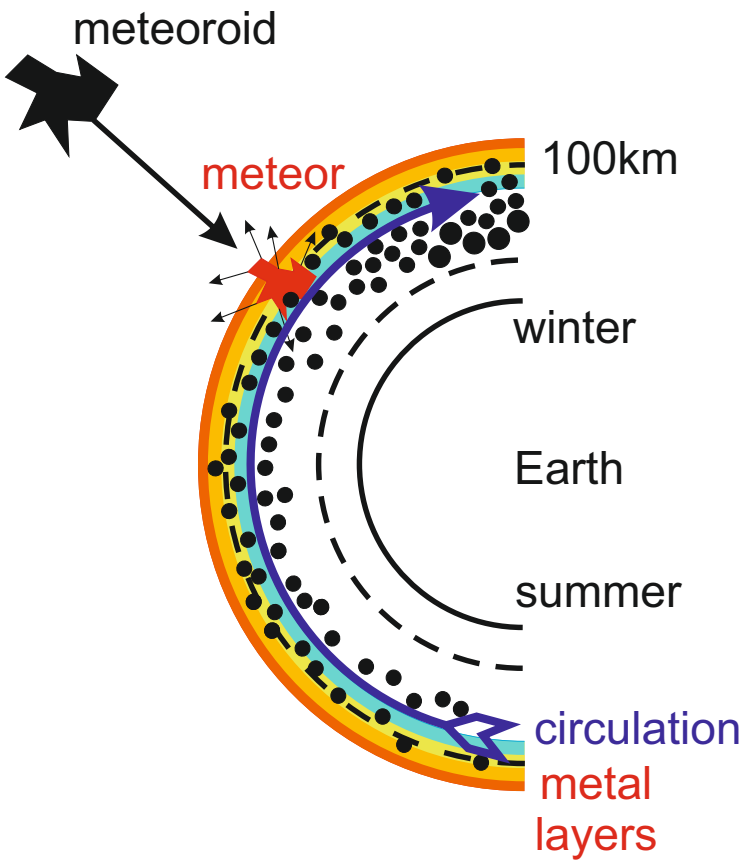

Figure 2.1: Schematic for the formation and dispersion of meteoric smoke particles within the Earth's atmosphere.

2.1 MSP formation and abundance

MSPs contribute to various phenomena in the Earth's atmosphere, e.g., MSPs are supposed to serve as condensation nuclei for stratospheric NAT (Nitric Acid Trihydrate) particles in the polar stratosphere (Voigt et al., 2005) or for ice particles within the polar summer mesopause visible as noctilucent clouds (e.g., Rosinski and Snow, 1961; Rapp and Thomas, 2006).

The microphysical properties (e.g., size, composition and abundance) of these MSPs govern the nature of these phenomena (e.g., Wilms et al., 2016, and references therein). The current understanding of MSP formation and abundance is sketched in Fig. 2.1. This Figure shows a schematic of the MSP formation processes and the dispersion within the atmosphere. When a meteoroid enters the atmosphere, it starts to evaporate and form the meteor phenomena. During this evaporation, which is also named meteor ablation, the meteor heats up to approximately 2500 K. After this temperature is reached, the rest of the meteors kinetic energy is used evaporate the meteors material (Ceplecha et al., 1998). This ablation mechanism is indicated in Fig. 2.1 by the arrows of the red meteor. During this ablation process, the meteor loses its atoms in a sequence according to the volatileness

of the species within the meteor. This so-called differential ablation mechanism (Vondrak et al., 2008) is the origin of different metal layers which have their maximum abundance at different altitudes around 100 km. Sodium and potassium evaporate earlier than iron, magnesium and silicon. This differential ablation is depicted in Fig. 2.1 by a color gradient within the metal layer.

As discussed above, these metallic layers can be detected by means of lidar techniques, where the transmitted wavelength is set to a resonance line of a metal species of interest (e.g., 589 nm for the sodium D2-line). It is also possible to retrieve metal density profiles from different satellites. This is done by applying iterative radiative transfer modelling in order to represent the scattered solar radiances measured by spectrometers onboard the satellites (e.g., Gumbel et al., 2007, for sodium). Marsh et al. (2013) have modelled the global distribution of sodium with the Whole Atmosphere Community Climate model (WACCM) by including sodium chemistry (Plane, 2004) and the meteor input function of Janches et al. (2006) and find reasonable agreement with the observations. The same climate model has been used to model the abundance of other meteoric material like iron (Feng et al., 2013), potassium (Dawkins et al., 2015) and silicon (Plane et al., 2016). A recent review of the nature of meteoric metals can be found within Plane et al. (2015).

The evaporated extraterrestrial metals and silicon undergo follow-up reactions with the background atmosphere. According to laboratory experiments of Saunders and Plane (2006) the species undergo reactions with atmospheric oxygen, water vapour and carbon dioxide to form hematite (Fe_2O_3), iron hydroxide and different silicate compounds. There is also a reaction pathway that requires the presence of solar UV radiation to form olivine ($Mg_{2x}Fe_{2-2x}SiO_4$) particles (Saunders and Plane, 2011). From insitu quantifications of the MSP work function (Rapp et al., 2012), it is also possible to further constrain the MSP composition. Rapp et al. (2012) state that iron and magnesium hydroxide clusters fit to the measured MSP workfunction (4 to 4.6 eV). There have also been attempts for direct MSP sampling at formation altitude (Hedin et al., 2014). Unfortunately, these experiments suffer from contamination which prevent reliable statements on the MSP composition.

The formation of these MSP precursor molecules was initially thought to occur within the trails of meteors (Hunten et al., 1980) on time scales in the order of minutes. However, the diffusion within meteor trails is so high, that the high number concentration cannot persist long enough to enable direct coagulation (Plane, 2003). More recent understanding expects that the ablated metals undergo reaction within the background atmosphere to form the precursor molecules (e.g., Plane, 2003). Subsequently, the precursor molecules grow by coagulation and form nanometer-sized particles which sediment down to lower altitudes as they grow. Megner et al. (2006) investigated the formation of particles by performing a large number of sensitivity studies using a microphysical MSP-model. Ablation height, vertical diffusion and wind, coagulation efficiency and meteoric mass influx are all relevant parameters for modelling MSPs in the Earth's atmosphere. However, this study also showed that transport by the atmospheric wind is likely the most important factor affecting the MSP distribution in the atmosphere.

This was further investigated by Megner et al. (2008) and Bardeen et al. (2008) who proved independently, that MSPs are affected by the residual circulation leading to an

effective transport of MSPs from the summer mesosphere to the winter mesosphere. The blue arrow within the sketch of Fig. 2.1 indicates the meridional branch of the residual circulation. The removal of MSPs from the summer mesosphere occurs on a timescale that is shorter than the formation of large MSPs, therefore MSPs with radii greater than 1 nm are much more abundant in the winter hemisphere. Typical number densities of MSPs larger than 1 nm reach values of up to 4000 cm^{-3} in the winter hemisphere while only values of 100 cm^{-3} are reached in the summer hemisphere at high latitudes and 80 km altitude. Down to lower altitudes the MSP grow to radii greater than 10 nm, but their number densities are much smaller. That is, values of 200 cm^{-3} can be reached in the winter polar hemisphere at 40 km altitude and only 10 cm^{-3} in the summer hemisphere. At 20 km the model results predict number densities of MSPs greater 10 nm of around 10 cm^{-3} on the winter hemisphere at high latitudes. These model results compare very well with the Geophysica particle measurements of Weigel et al. (2014) who also find 8 cm^{-3} with sizes between 10 nm and about 1 μm within the polar vortex at 20 km.

2.2 Experimental evidence of MSP existence

MSPs are supposed to be involved in different kinds of phenomena within the upper atmosphere, e.g., radar echoes from evaporating meteors in a nonspecular trail (Chau et al., 2014) or are even thought to be subject to levitation due to magneto-photophoretic effects (Rohatschek and Horvath, 2010; Cheremisin et al., 2011). This section reviews the experimental evidence that MSPs exist at mesospheric altitudes. This is done by introducing corresponding measurement techniques which may be ground based (Sect. 2.2.1) or satellite based (Sect. 2.2.3). In addition, direct measurements of MSPs onboard sounding rockets are described in Sect. 2.2.4. A certain effect of artificial electron heating experiments in the vicinity of Polar Mesospheric Winter Echoes (PMWE) which can only be explained by the presence of MSPs is described in more detail in Sect. 2.2.2.

2.2.1 Ground-based MSP detection by incoherent scatter radar

Incoherent Scatter Radars are powerful tools for atmospheric remote sensing. These instruments work by transmitting electromagnetic radiation in the MHz to GHz range, which scatters from electrons themselves (incoherent) or from ordered structures (coherent). The scattered radiation is detected at a receiving site, which is usually identical with the transmitter.

The spectral shape of the backscattered signal contains information about the partially ionized plasma of the ionosphere. Until a study of Cho et al. (1998), it was thought that the spectral width of backscattered signals from the D-region is only governed by properties of ions. However, Cho et al. introduced nanometer sized charged particles into the theory of incoherent scattering of radar signals. By taking into account MSPs, the received spectrum gains a narrowing effect which is superimposed on a broad spectrum due to ionic components.

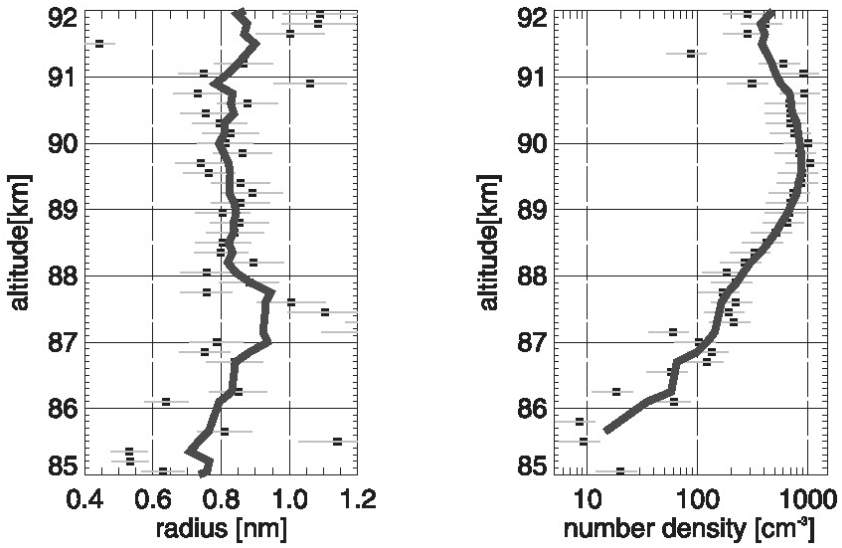

Figure 2.2: Radar measurement of MSP radii (left) and number density (right), derived from the spectral shape of the backscattered signal. Reprinted Fig. 4 from Strelnikova et al. (2007) with permission of John Wiley and Sons.

The first application of this new theory to a practical experiment was presented by Rapp et al. (2007). They used the EISCAT UHF radar in Tromsø, Norway and were able to identify MSP signatures in the ISR spectra. However, a lack of sensitivity prohibited quantitative statements on the abundance and size of the MSPs. A follow-up study by Strelnikova et al. (2007) used the more sensitive Arecibo radar in Puerto Rico with its 305 meter dish and its 2 MW transmitter at 430 MHz to find signatures of charged MSPs in the D-region. Figure 2.2 shows the results of their experiment. It was indeed possible to determine mean MSP radii (left panel) and MSP number densities (right panel). The results show mean MSP radii of 0.8 nm, which seem to be constant over the altitude range from 85 to 92 km. The number density of MSPs increase dramatically from 10 cm^{-3} at 85 km to 1000 cm^{-3} at 90 km. These results lie within the modelled results (e.g., Megner et al., 2006).

This method has been adapted also to the PFISR radar at Poker Flat, Alaska (Fentzke et al., 2012) at polar latitudes. These experiments show a higher diurnal variability in the MSP size as at equatorial latitudes at the Arecibo radar. This difference is accounted to a different transport at high latitudes. Another study by Fentzke et al. (2009) investigated the seasonal variation of MSP at the Arecibo location. They find no significant variablity in MSP size and abundance which is expected from the MSP-model studies (Megner et al., 2008; Bardeen et al., 2008).

2.2.2 The role of MSPs in radarechoes within the polar winter mesosphere

Polar Mesospheric Winter Echoes (PMWE), as the name suggests, are radar echoes within the polar winter mesosphere (e.g., Balsley et al., 1983). They can occur in the northern hemisphere (Latteck and Strelnikova, 2015) and the southern hemisphere (Nishiyama et al., 2015). The radar echoes are observable in the VHF (Very High Frequency) range and also in the UHF range (Strelnikova and Rapp, 2013) between 50 and 80 km. In general, radars need a sharp gradient in the electron density profile (i.e., the refractive index) in order to receive radar signals like the PMWE. Their occurrence is in some extent also linked to the availability of sunlight and enhanced ionization levels due to energetic particle precipitation during geomagnetic storms.

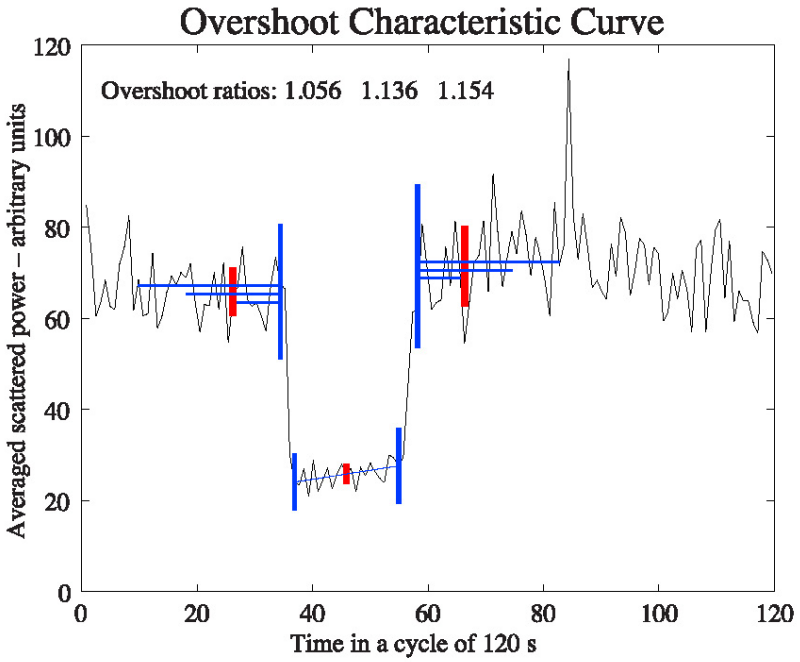

Figure 2.3: Timeseries of a PMWE experiment, radar signal of a PMWE with a 20 seconds HF heating phase in between, PMWE signal after heating phase shows a overshoot effect. Reprinted Fig. 3 from La Hoz and Havnes (2008) with permission of John Wiley and Sons.

In general, there are three different theories which aim to explain the PMWE phenomenon:

1. Infrasound waves. Kirkwood et al. (2006) propose, based on a PMWE measurements measured at 52 MHz and 225 MHz simultaneously, infrasound waves emitted from the ocean surface as a PMWE explanation.

2. Neutral air turbulence only. The study of Lübken et al. (2006) showed that in the particular case studied, only neutral air turbulence can account for the observed

PMWE. They relate in-situ ion density measurements which show turbulent features inside a PMWE volume and no indication of turbulence outside of the PMWE layer.

3. Neutral air turbulence with large Schmidt-number (as in polar mesospheric summer echoes PMSE (Rapp and Lübken, 2004)). The existence of charged particles in the vicinity of mesospheric radar echoes (ice particles in PMSE, MSPs in PMWE) reduces the diffusivity of the ambient electrons. This reduced diffusivity enables the survival of turbulent structures for long times (see also Rapp et al., 2011).

The third explanation of PMWE is also supported by the study of La Hoz and Havnes (2008). They observed PMWE during periods of artificially heated electrons. Free electrons in the mesosphere can be heated with a special radar heater. This device is a transmitter of continous radiation in the HF band (few MHz) with transmitting powers of several MW. A radar heater can increase the electron temperature by approximately one order of magnitude above the neutral/ion temperature in the D-region. La Hoz and Havnes (2008) described an observation of PMWE with a 52 MHz radar, during which the heater was repeatedly activated for 20 sec and turned off for 100 sec in order to establish undisturbed conditions in between two heating pulses. Figure 2.3 shows a sumperimposed timeseries of several cycles of the heated and non-heated PMWE signal. The authors call this timeseries an Overshoot Characteristic Curve. It shows an instantaneous drop in signal power just when the heater is turned on, followed by a heating phase in which the PMWE signal slightly recovers. The next phase is when the heater is turned off again, in that moment the PMWE recovers to its original power and even overshoots to higher signal power compared to the initial PMWE level.

La Hoz and Havnes (2008) interpreted their overshoot curve with a particle charging model (Havnes et al., 2004), which has already been used to verify an ice particle influence within the polar mesospheric summer echo phenomenon (Rapp and Lübken, 2004). By using MSPs within this model the overshoot characteristic curve can be reproduced. The explanation is as follows: due to the heater transmission the electron temperature is increased by a factor of five or more, the MSPs remain unaffected. As a consequence, the diffusivity of the free electrons is strongly enhanced and the electrons diffuse out of the PMWE layer. Therefore, the detectable electron gradient and PMWE is immediately weaker. During the heating phase the attachment rate of free electrons is increased and the MSPs carry much more electrons as under normal conditions. This enhanced charging of MSPs increases the PMWE signal slightly as the heater is still on. When the heater is turned off, the temperature and diffusivity of the electrons relax rapidly to background levels, but the MSPs remain highly charged. Hence, the electrons diffuse back and show larger gradients within the stronger charged MSP-structures, i.e., the PMWE overshoot.

Follow up studies (Havnes and Kassa, 2009; Havnes et al., 2011) refined the particle charging model and included the photodetachment process into the charging scheme. They identified photodetachment of negative MSPs to be important, as this effect has to be overcome by the attachment of free electrons at the same time in order to charge MSPs negatively. This requires elevated ionization levels during particle precipitation and solar radiaton, which is the case during during most PMWE events. However, Kero et al. (2008)

showed that also the temperature dependence of the negative ion chemistry is related to the results of PMWE heating experiments, but this cannot explain the overshoot effect. They suggested to also represent the ion chemistry together with the charged particle model in order to explain PMWE thoroughly.

2.2.3 Space-based spectrometers reveal atmospheric transport of MSPs

Another possibility to detect MSPs is to use observations from space. In 2007 a specialized satellite mission was launched for the investigation of nanometer-sized ice particles in the mesosphere, the Aeronomy of Ice in the Mesosphere (AIM) satellite. This satellite carries two instruments, firstly the CIPS device images mesospheric ice clouds using four cameras at 265 nm in a nadir observation mode (Russell III et al., 2009). Secondly, the Solar Occultation for Ice (SOFIE) instrument, which is a spectrometer sensitive to 16 spectral bands between 0.29 and 5.32 μm working in the solar occultation geometry (Gordley et al., 2009). The measurements are available between $65° - 82°$ in both hemispheres with a vertical resolution of 2 km and a few kilometers along the line of sight (limb geometry).

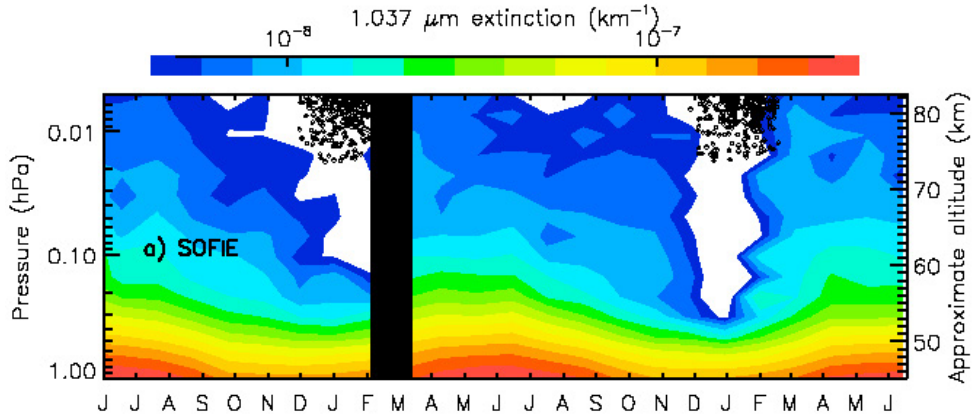

Figure 2.4: Results of the SOFIE instrument onboard the AIM satellite showing the annual variation of solar absorption at 1.037 μm which is related to the MSP abundance within the atmosphere, from June 2007 to June 2009. Reprinted Fig. 3a from Hervig et al. (2009) with permission of John Wiley and Sons.

In order to identify MSPs with the SOFIE instrument, Hervig et al. (2009) used the measured extinction in the 1.037 μm channel. After separating the Rayleigh extinction and MSP-related extinction, it is possible to detect MSPs at high latitudes on a continuous basis. Figure 2.4 shows the MSP-related extinction from 45 to 85 km for a two year period in the southern hemisphere. There is a pronounced seasonal variation in this extinction due to MSP. During the summer period the extinction is so low that it can't be measured anymore. This is because MSPs are transported to the winter hemisphere. During winter the extinction is much stronger, which indicates more abundant MSPs. Unfortunately, the measured MSP-related extinction cannot be related to MSP properties as number density

or size since their composition and hence their optical properties are not known. It has also been possible to derive the MSP extinction from the MSP-circulation models by assuming a MSP composition of olivine. Corresponding results compare very well with the observed extinctions of SOFIE (Hervig et al., 2009). In addition to SOFIE, also observations from the SAGE II satellite show extinctions at altitudes between 30–40 km which can only be modelled when incorporating MSPs as an additional aerosol component (Neely et al., 2011). At higher altitudes the SAGE II satellite lacks the sensitivity of SOFIE, but due to a different orbit also detects the MSP related extinction at low latitudes in the 30–40 km region.

Furthermore, the SOFIE instrument has been able to even detect small quantities of MSPs within noctilucent ice particles (Hervig et al., 2012). The measured extinction ratios from the UV to the infrared are not compatible with the optical properties of pure ice. Hervig et al. (2012) derived the optical parameters of ice mixed with different kinds of possible MSP types. They found that the SOFIE observations indicate that the NLC ice particles likely contain carbon, wüstite, or magnesiowüstite with volume fractions between 0.01–3 %.

2.2.4 Charged MSP signatures in rocket-borne measurements

The first signatures of charged MSP were found by Schulte and Arnold (1992). They used a quadrupole mass spectrometer mounted on a sounding rocket. In an integral mode, the mass spectrometer counted significant numbers of heavy negative ions above 400 amu in an altitude range between 78–90 km. Based on these results Schulte and Arnold (1992) suggested that these ions were actually negatively charged MSP.

The next major step in the investigation of charged aerosol particles in the mesopause region was taken by Havnes et al. (1996) who were the first to use a Faraday cup to measure charged ice particles inside radar returns from the vicinity of mesospheric ice clouds, also known as polar mesospheric summer echoes (e.g., Rapp and Lübken, 2004). This technique uses two biased entrance grids to shield the electrode at the bottom of the Faraday cup from ambient light ions and electrons and only allows heavy charged particles to be measured.

Havnes et al. (2014) reported results of a new Faraday-Cup version with a possibility to fragment mesospheric ice particles. The so called MUDD detector (MUltiple Dust Detector) contains a third grid that consists of slanted ramps. When ice particles impact the third grid, they are fragmented and the charged remnants are detected on the bottom plate using an electrometer. The bias between bottom plate and the third grid is varied between 0 V, 10 V and 20 V in order to determine the energy of the fragments. Havnes et al. (2014) concluded that the detected remnants consist partly of ice and partly of water-coated MSPs. By assuming a ten percent MSP fraction of the detected particles and a charging probability of these MSPs in the range of 10 to 100 % they find similar MSP volume fractions in mesospheric ice particles as the study of Hervig et al. (2012).

In this study we concentrate on the standard Faraday cup measurements and corresponding plasma observations on the same sounding rocket (see Table 2.1 for details of the rocket flights). These listed flights took mainly place at winter polar latitudes during nighttime.

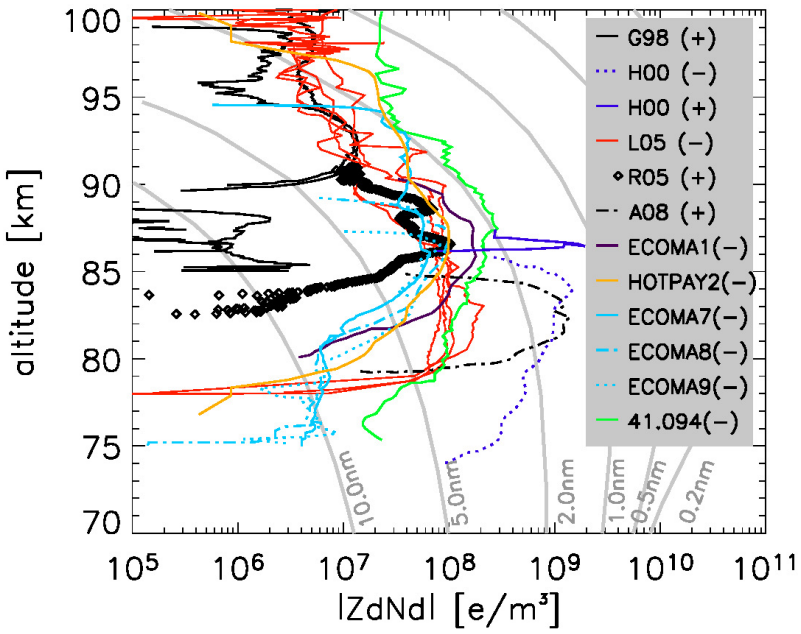

Figure 2.5: Rocket-borne charged MSP density measurements during nighttime, updated from Rapp et al. (2007) and Friedrich and Rapp (2009), grey contours show MSP number densities after Hunten et al. (1980), legend entries are explained in Tab. 2.1, +/- indicate the charge sign of the measured MSP. Reprinted from Baumann et al. (2013).

Table 2.1: Collection of in-situ measurements of charged MSP during darkness; the labels are used for the MSP height profiles in Fig. 2.5, the last five flights measured plasma densities simultaneously, mean values are shown in Fig. 4.1. Reprinted from Baumann et al. (2013).

Label	Lat. (° N)	Date	Technique/Comments	Reference
G98	18	19 Feb 1998	Faraday cup	Gelinas et al. (1998)
H00	32	02 Nov 1998	Magnet. shield. probe	Horanyi et al. (2000)
L05	65	07 Mar 2002 15 Mar 2002	Faraday cup, Four rocket flights	Lynch et al. (2005)
R05	68	28 Oct 2004	Faraday cup	Rapp et al. (2005)
A08	69	10 Jan 2006	Magnet. shield. probe	Amyx et al. (2008)
ECOMA1	69	08 Sep 2006	Faraday cup	Strelnikova et al. (2009)
HOTPAY2	69	31 Jan 2008	Faraday cup	Friedrich et al. (2012)
ECOMA7	69	04 Dec 2010	Faraday cup	Rapp et al. (2012)
ECOMA8	69	13 Dec 2010	Faraday cup	Rapp et al. (2012)
ECOMA9	69	19 Dec 2010	Faraday cup	Rapp et al. (2012)
41.094	69	11 Oct 2011	Aerosol MS (MASS), 500–2000 amu chann.	Robertson et al. (2013), Friedrich et al. (2012)

Gelinas et al. (1998) were the first to use such a device during dark conditions outside the polar summer mesopause. Other versions of such MSP detectors, which were able to distinguish between positive and negative charges, were later flown between 2002 and 2008 (Lynch et al., 2005; Rapp et al., 2005; Enell et al., 2011; Friedrich et al., 2012). Lately, the technique of the Faraday cup MSP detection has been combined with active photoionization by a xenon flash lamp (Rapp and Strelnikova, 2009; Strelnikova et al., 2009; Rapp et al., 2010, 2012) and was flown several times.

Additionally, Table 2.1 lists experiments that differ slightly from the original detector design. The probes from Horanyi et al. (2000) and Amyx et al. (2008) use magnetic instead of electrostatic fields to avoid contamination from ambient plasma. The MASS experiment (see Robertson et al., 2009, 2013, for details) on the other hand is an electrostatic filter with rather crude mass resolution. It gives results comparable to Faraday cup observations, when only considering the 500–2000 amu mass channel (data taken from Friedrich et al., 2012).

In Fig. 2.5 all MSP height profiles of the experiments discussed briefly above are shown. We note that most of the measurements gave evidence for negatively charged particles. Note, however, that this does not necessarily mean that only negatively charged particles exist during darkness. Robertson et al. (2009) showed with the MASS experiment, that negatively and positively charged particles might coexist. The character of Faraday cup measurements is that the sum of all detectable positively and negatively charged MSP is recorded (i.e., the net charge density). That means the measurement of a negative signal shows that an excess of negative MSP compared to positive MSPs exists. The predominant negative charge of MSP is likely caused by the fact that the capture rate of plasma constituents by aerosol particles is proportional to the thermal velocity of the plasma constituents ($\sim \sqrt{\frac{kT}{m}}$), which means that the mass of the plasma constituent is important. Since electrons are much lighter than ions, this results in a higher capture rate for electrons compared to positive ions. During nighttime, photoionization of neutral MSP by scattered Ly-α radiation from the geocorona (e.g., Meier, 1991, and references therein) as an additional source of positively charged MSP is possible, but not expected to be dominant.

3 Charging processes of MSP in the D-region ionosphere

Meteor smoke particles are subject to various charging mechanisms within the Earth's atmosphere. An overview of these mechanisms is shown Fig. 3.1. Relevant processes are attachment of ionospheric plasma species, detachment of electrons from negatively charged MSPs and photoemission of electrons from neutral MSPs due to solar radiation and secondary electron emission from MSPs caused by energetic electron precipitation from the magnetosphere. These charging processes cannot be generalized as the ionosphere, the solar radiation and electron precipitation vary strongly with altitude. The D-region composition changes with altitude, from a plasma containing only electrons and positive ions above 90 km, to a plasma also containing negative ions around 80 km and finally to a plasma containing only ions of both charge sign and no free electrons at 60 km altitude and below. This changing ionospheric background limits the available ions and electrons to attach to MSPs. Also the solar radiation and electron precipitation cannot be generalized for the whole D-region. The penetration depth of solar photons is determined by the abundance of atmospheric species (e.g., O_2 and N_2) and their absorption cross sections. At D-region altitudes, the absorption of solar photons occurs only in the wavelength range below 200 nm, just these energetic photons are important in order to ionize MSPs. Energetic electrons are, similarly to the absorption of solar photons, also absorbed within the atmosphere. However, precipitating electrons with high energies can penetrate deep into the atmosphere while low energy electrons are absorbed already at higher altitudes. Both absorption processes reduce the available flux of solar photons and energetic electrons to charge MSPs. On top of this changing backround of MSP charging sources also the MSP distribution shifts to greater radii as the particles sediment to lower altitudes and grow by coagulation.

This chapter contains a detailed description of the interaction processes of MSPs with the ambient ionosphere. The first type of MSP charging is the attachment of free electrons and ions to MSPs which can be neutral or charged (Section 3.1). The second type contains the electron detachment from negatively charged MSPs and photoionization of neutral MSPs, both induced by solar photons (Sect. 3.2). The third type is the charging of MSP by impact of energetic electrons from the magnetosphere, i.e., which may cause secondary electron emission (Sect. 3.3). In order to determine the relevance of charging secondary electron emission, Sect. 3.3 also contains a comparative study of the above mentioned MSP charging processes. The results of Sect. 3.3 have already been published in Baumann et al. (2016), also Sect. 3.1 and 3.2 are partly published within Baumann et al. (2013) and Baumann et al. (2015).

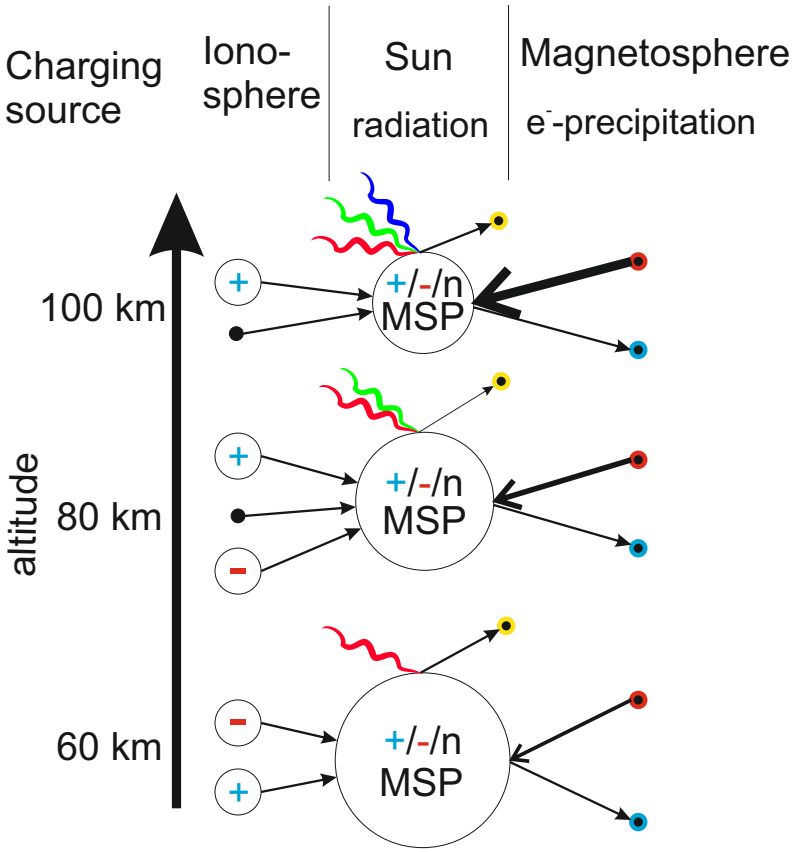

Figure 3.1: Schematic of the different charging processes of MSPs at 60, 80 and 100 km altitude. Firstly, attachment of ionospheric positive ions (circles with +), free electrons (black dots) and negative ions (circles with -) to MSPs. Secondly, detachment and emission of photoelectrons (black/yellow dots) from negative MSPs respectively neutral MSPs by solar photons, ray colors indicate available photon energy. Thirdly, secondary electron emission (black/blue dots) induced by energetic electrons (black/red dots) from the magnetosphere, arrow thickness indicate available energetic electron flux. Mean MSP size is indicated by circle diameter. Description see text.

3.1 Plasma Attachment to MSP

Attachment of ions of both polarity to the surface of particles is a well described process in the lower atmosphere (Natanson, 1960; Fuchs, 1963). The awareness that the MSPs are important key players within the aeronomy of the mesosphere and D-region ionosphere made it necessary to obtain a formalism in this regime. Rapp (2000) adapted the formalism of Natanson (1960) for the charging of particles through the attachment of free plasma components in this altitude region which has hitherto been applied to the conditions of ice particles in the polar summer mesopause (e.g., Reid, 1990; Jensen and Thomas, 1991; Rapp and Lübken, 2001). This Section describes the formalism as it is used in this thesis.

The plasma attachment to MSPs can be divided into three sub groups accounting for the different charge states of MSPs and the charge sign of the attaching plasma component. Firstly, the MSP carries no charge and the attaching plasma component can be of negative or positive charge, i.e., the charging of a neutral MSP. Secondly, the MSP already carries a charge and the attaching plasma component has an opposed charge, i.e., the recombination of a charged MSP resulting in a neutral MSP. Thirdly, the MSP carries a charge and the attaching plasma component has the same charge sign, i.e., the MSP is multiply charged.

Charging of neutral MSPs

The attachment charging process works as follows. The ion or electron attaches to a neutral MSP and is removed from the D-region, i.e., the ion/electron is bound to the MSP and transfers the charge to it. The charging process of neutral MSPs is represented by the rate coefficient k_{charging} as follows:

$$k_{\text{charging}} = \gamma_{charging} \cdot \pi \cdot r_p^2 \cdot c_{e/i^+/i^-} \cdot \left(1 + \sqrt{\frac{e^2}{8 \cdot \epsilon_0 \cdot k_B \cdot T_{e/i^+/i^-}(h) \cdot r_p}}\right). \tag{3.1}$$

The radius of the MSP is given by r_p, T is the temperature depending of the altitude h which is the same for electrons and ions in the D-region, ϵ_0 is the permittivity of free space, e is the elementary charge and k_B is the Boltzmann constant. $c_{e/i^+/i^-}$ represents the thermal velocity of the plasma components and is given by the formula $c_{e/i^+/i^-} = \sqrt{8kT_{e/i^+/i^-}/\pi m_{e/i^+/i^-}}$. Here, $m_{e/i^+/i^-}$ denotes the mass of a charge carrier, which can be an electron, a positive ion or a negative ion. The dimensionless prefactor $\gamma_{charging}$ represents a charging efficiency of particles by plasma components which is a function of particle size and composition, as introduced by Megner and Gumbel (2009). This charging efficiency $\gamma_{charging}$ is not very well known and laboratory data for the expected MSP composition is not available. Nevertheless, Megner and Gumbel (2009) provide a valuable information about this prefactor by analyzing laboratory data of the electron attachment efficiency of CO_2 and H_2O clusters (Vostrikov and Dubov, 2006a,b). For the nature of γ_{charging} Megner and Gumbel (2009) find a vanishing charging probability for particles with radii smaller than 0.25 nm and assured charging for particles with radii larger than 1.5 nm with a linear

increase of probability in between these radii. For quantitative use in this thesis, $\gamma_{charging}$ has been adapted from their Figure 6 in the following form:

$$\gamma_{charging}(r_p) = \begin{cases} 0, & \text{for } r_p < 0.25 \text{ nm}, \\ 0.8\,\text{nm}^{-1} \cdot r_p - 0.2, & \text{for } 0.25 \leq r_p \leq 1.5 \text{ nm}, \\ 1, & \text{for } r_p > 1 \text{ nm}. \end{cases} \tag{3.2}$$

Equation 3.1 represents the process where the plasma components induce an image charge within the MSP particle. That leads to an attractive force for the electrons and ions, i.e., the second term within the parentheses. This attractive force leads to an increase of the thermal flow of plasma onto the surface of the MSP, i.e., the term outside the parentheses of Eq. 3.1.

It has to be noted that this is a classical representation of a quantum process. The study of Plane et al. (2014) contains quantum chemical calculations of electron attachment coefficients to the surface of the $FeMgSiO_4$ molecule, which is supposed to be an initial MSP nucleus molecule. Actually, they found excellent agreement to the attachment coefficient for 0.25 nm MSPs derived by the formalism of Natanson (1960). However, the results of Plane et al. show that also the smallest MSPs are effectively charged within the D-region. If that would be the case, the D-region would contain substantial less free electrons as it does. The only exit of this contradiction would be a significantly lower amount of smallest MSPs as expected from current MSP modeling. To account for that, γ_{charging} can be interpreted as a correction factor.

Recombination of charged MSPs with oppositely charged plasma

The attachment of ionospheric constituents to MSPs can also occur when these MSPs are already charged. In case a charged MSP captures an oppositely charged plasma constituent and recombines to a neutral MSP, the reaction rate coefficient of this process is given by Eq. (3.3).

$$k_{recomb} = \gamma_{recomb} \cdot \pi \cdot r_p^2 \cdot c_{e/i^+/i^-} \cdot \left(1 + \frac{|q| \cdot e^2}{4 \cdot \pi \cdot \epsilon_0 \cdot k \cdot T_{e/i^+/i^-}(h) \cdot r_p}\right) \tag{3.3}$$

In addition to equation (3.1), q is here the absolute value of the charge number of the MSP. For the recombination probability γ_{recomb} we again follow the argumentation of Megner and Gumbel (2009) and set $\gamma_{\text{recomb}} = 1$. The difference between this Equation and Eq. 3.1 is that direct Coulomb forces instead of image charge forces enhance the thermal flow of plasma onto the MSP surface.

Multiple Charging of MSPs

Finally, it is also possible that a charged MSP captures an ionospheric constituent which carries a charge of the same sign. The occurence of this process is of course limited, as the

ionospheric constituent has to overcome the Coulomb barrier of MSP in order to reach its surface.

$$k_{repuls} = \pi \cdot r_p^2 \cdot c_{e/i^+/i^-} \cdot g^2 \cdot exp(-\frac{|q|\, e^2}{g \cdot k \cdot T_{e/i^+/i^-}(h) \cdot r_P}) \tag{3.4}$$

In addition to the attachment coefficients of ionospheric electrons and ions to neutral or oppositely charged MSP, this reaction rate coefficient contains a factor g which depends on the MSP charge number q. This g is the fraction of a distance r_0 from the particle center and the MSP radius. The distance r_0 indicates the location away from the MSP where the ionospheric constituent has overcome the repulsive Coulomb potential and enters the attractive image charge potential.

3.2 Charging and Discharging of MSP by solar radiation

As MSPs consist of absorbing material, it is also possible that they interact with solar photons. Detachment of electrons from negatively charged particles and ionization of neutral particles are the processes which can be induced by solar photons. It is evident that the photo ionization of MSPs requires photons of high energy. Therefore, the absorption of solar radiation within the atmosphere has to be taken into account, in order to derive reliable photo reaction rates.

By using absorption cross sections of different atmospheric constituents one can calculate the optical thickness τ and derive from that the attenuation of the solar spectrum following the Lambert-Beer law (e.g., Rees, 1989). These absorbing species are mainly O_2, N_2, Ar and O. Corresponding solar spectra at different atmospheric altitudes are shown in Fig. 3.2, as derived within the SIC model. This shows that the available solar spectrum below 200 nm is a strong function of altitude. Already at 100 km height, the solar X-Rays below 100 nm are completely absorbed. Solar radiation with wavelengths between 110 and 130 nm and above 170 nm penetrates down an altitude of 90 km. But only the Ly-α photons (121.6 nm) can penetrate deep down into the atmosphere, as there are still photons available at 70 km altitude. However, at 60 km altitude, which is the lower boundary of the D-region, there is no solar irradiance below 180 nm left. The absorption of solar radiation above 180 nm is negligible at these altitudes.

Ly-α photons are actually the source of the daytime D-region, as they contain enough energy to ionize nitric oxide (NO). The reason is that the absorption cross section of O_2 is very variable between the ionization treshold of O_2 (102.6 nm) and the Schumann-Runge continuum (135 nm). Moreover, right at the wavelength of the Ly-α-line there is a deep local absorption minimum allowing a deep penetration of these photons into the Earth's atmosphere. At wavelengths' below 102 nm, N_2 molecules can still absorb photons down to its ionization treshold at 79.6 nm. Below that wavelength, the absorption originates mainly from ionization of O_2, N_2 and O.

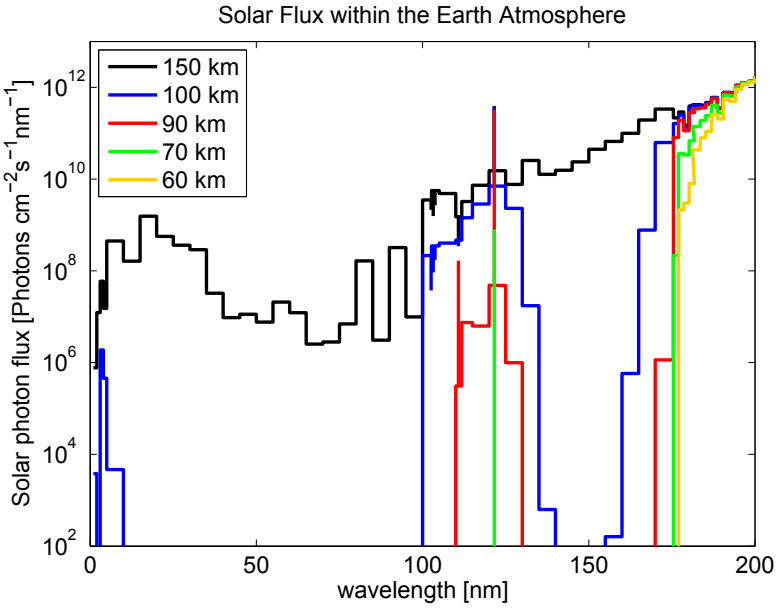

Figure 3.2: Solar photon spectrum including individual spectral lines (102.6 nm, 103,2 nm, 103.8 nm, 110,8 nm, 121.6 nm) available at different altitudes above the ground, the 150 km spectrum, absorption derived within the SIC model.

Following Rapp (2009), the reaction rate coefficient for the photo reactions of MSPs are derived using Mie theory, i.e.,

$$k_{photo} = \int_{\lambda_0}^{\lambda^*_{1/2}} F(\lambda, \chi) \cdot \sigma_{1/2}(r_\mathrm{p}, m, Y_{1/2}, \lambda) \cdot \mathrm{d}\lambda. \tag{3.5}$$

Here, $F(\lambda, \chi)$ is the solar irradiance which is dependent on the wavelength λ and solar zenith angle χ. $\sigma_{1/2}(r_\mathrm{p}, m, Y_{1/2}, \lambda)$ is the absorption cross section of MSPs. The integral is taken over the wavelength from a starting point λ_0 to the wavelengths $\lambda^*_{1/2}$. In an ideal case $\lambda_0 = 0$, but since spectroscopic material data is only available in a limited wavelength region, we have chosen λ_0 to be 100 nm. During nighttime the most important light source is Ly-α radiation scattered from the geocorona with a wavelength of 121.6 nm. λ^*_1 corresponds to the lowest photon energy that can detach an electron from a negatively charged MSP (i.e., the electron affinity), while λ^*_2 corresponds to the lowest energy of a photon that can ionize neutral MSP (i.e., the work function). We follow the argumentation of Rapp et al. (2010) that $\lambda^*_1 = 2.2\,\mathrm{eV}$ ($\cong 560\,\mathrm{nm}$) and $\lambda^*_2 = 5.5\,\mathrm{eV}$ ($\cong 225\,\mathrm{nm}$). However, we want to indicate that these values are not very well known and are subject to major uncertainties. The solar irradiance is taken from the SOLAR2000 model (Tobiska and Bouwer, 2006) and the SIC model derives height resolved spectra as described above. The MSP cross section for photodetachment/photoemission is then given by the following

equation using Mie theory:

$$\sigma_{1/2}(r_\mathrm{p}, m, \lambda) = \pi r_\mathrm{p}^2 \cdot Q_\mathrm{abs}(r_\mathrm{p}, m, \lambda) \cdot Y_{1/2}. \tag{3.6}$$

The photo emission/detachment cross section is a function of MSP composition. This composition dependence is described by Q_abs. Q_abs is the absorption efficiency in the Mie scattering theory and a function of the complex refractive index $m = n - i \cdot k$, where n is the refractive index and k is the absorption coefficient. To the authors' knowledge, n-k data in the range from 100 to 600 nm exists only for hematite (Fe_2O_3) as a reasonable MSP material (Triaud, 2013). Since MSP particles have sizes much smaller than 100 nm, the Mie calculation can be approximated in the Rayleigh regime as follows (Eidhammer and Havnes, 2001):

$$Q_\mathrm{abs} = 4X \frac{6nk}{(n^2 - k^2 + 1)^2 + (2nk)^2}, \tag{3.7}$$

where $X = 2\pi r_p/\lambda$ denotes the Mie parameter from the Mie theory. In Eq. (3.6) the quantity Y is the photoemission yield, which we have derived using the Fowler–Nordheim law (Fowler and Nordheim, 1928; Schmidt-Ott et al., 1980).

$$Y_{1/2}(\lambda) = C \left(\phi_{1/2} - \frac{h \cdot c}{\lambda} \right)^2 \tag{3.8}$$

Here, $\phi_{1/2}$ is the corresponding electron affinity / work function (photodetachment or photoionization) of MSPs and C is a material constant which we set in our calculations to 0.01 (Schmidt-Ott et al., 1980).

The electron affinity and work function of small particles can differ substantially from their bulk values; Wood (1981) and Burtscher et al. (1982) use a classical approach to describe the behavior of nanoparticles.

$$\phi = \phi_0 + \frac{e^2(q+1)}{4\pi\epsilon_0 r_p} - \frac{5}{8}\frac{e^2}{4\pi\epsilon_0 r_p} \tag{3.9}$$

Here, ϕ_0 is the electron affinity or work function of the bulk material. This formalism has been applied by Rapp et al. (2010) and will be used to describe photoelectric properties of MSPs in this thesis.

3.3 Secondary Electron Emmission from Meteoric Smoke Particles

This section has already been published within Baumann et al. (2016).

Secondary electron emission (SEE) occurs when an energetic electron hits and enters a material. Consequently, a secondary electron may be excited with enough energy to leave the material (Austin and Starke, 1902). This physical effect has been studied in various

fields, e.g., material sciences (e.g., Bruining, 1954, and references therein), astrophysics (e.g., Goertz, 1989; Walch et al., 1995; Abbas et al., 2012) and space applications (e.g., Katz et al., 1986; Balcon et al., 2012). Also the Earth's atmosphere is subject to energetic electron precipitation, which is the reason for the well-studied phenomenon of the aurora (e.g., Rees, 1969). Furthermore, Anderson and Koons (1996) reported that SEE also has effects on the charge state of satellites when they orbit low over the poles within the auroral regions. There have also been studies covering SEE from atmospheric molecules in the context of auroral excitation mechanisms (e.g., Rees et al., 1969).

This work, however, aims at investigating whether SEE is also a relevant charging process for meteoric smoke particles (MSPs). Furthermore, MSPs are present in the mesosphere which coincides with the altitude region where much of the energy of the precipitating electrons is deposited and therefore are likely to be affected by SEE. These MSPs are particles, which originate from extraterrestrial matter that is injected into the atmosphere by evaporating meteors (Rosinski and Snow, 1961; Megner et al., 2006). The existence of these MSPs was proven by in-situ measurements on sounding rockets (e.g., Havnes et al., 1996; Rapp et al., 2012), by spectrometers on board satellites (Hervig et al., 2009) and by means of incoherent-scatter radars (Strelnikova et al., 2007). MSPs have effects on the nucleation of ice particles in the mesosphere (e.g., Wilms et al., 2016, and references therein) and influences on the ionospheric charge balance (Friedrich et al., 2012; Baumann et al., 2013; Plane et al., 2014; Asmus et al., 2015) and ion chemistry (Baumann et al., 2015) of the D region.

This study of the SEE from MSPs in the polar atmosphere investigates its relevance by comparing the rates of SEE with other MSP-related charging rates. The paper is structured as follows: Sect. 3.3.1 covers the formalism to derive SEE rates. Section 3.3.2 is divided into two parts: Sect. 3.3.2 examines the in-situ differential flux of the energetic electrons and its impact on the D-region ionosphere for three different precipitation cases; Sect. 3.3.2 contains the comparison of the derived SEE rates with the other MSP-related charging rates for the different precipitation cases and at the altitudes 70 and 90 km. Finally, in Sect. 3.3.3 we draw conclusions.

3.3.1 Secondary Electron Emission from Particles

This section describes the fundamentals of secondary electron emission (SEE) from particles as it is widely used within the dusty plasma physics community (e.g., Meyer-Vernet, 1982). The SEE yield, i.e., the number of secondary electrons generated by one incoming electron, is a crucial parameter within the derivation of the SEE electron flux leaving particles which are subject to high-energy electron bombardement. The formalism of the SEE yield for nanometer-sized particles used in this study has been derived by Chow et al. (1993). In the following, we want to recapitulate the most important formula which has been used to derive the flux of secondary electrons generating from MSPs in the Earth's polar atmosphere where auroral electron precipitation is present.

The SEE yield was experimentally studied in the beginning of the last century but only for solid materials (e.g., Austin and Starke, 1902; Bruining, 1954). Chow et al. (1993) were

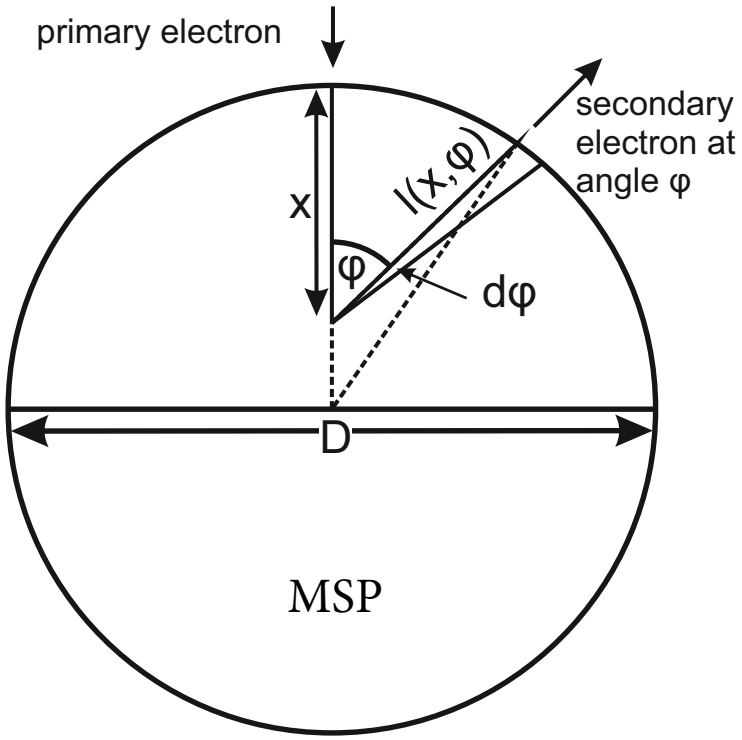

Figure 3.3: Principle of secondary electron emission in particles after Chow et al. (1993) (description see text). Reprinted from Baumann et al. (2016).

the first to develop a SEE yield formalism for particles, which not only shows high yields for smaller particles but also reproduces the bulk SEE yield when applying larger particle radii ($r > 1$ μm). In Fig. 3.3 the basic principle of the SEE process within particles is described. Here, a primary electron enters a particle of radius $D/2$ and penetrates a depth x from the surface. On its way to the depth x secondary electrons can be stimulated by the deposited energy of the primary electron. This secondary electron travels through the particle and is emitted in a direction under an angle ϕ with respect to the path of the primary electron. The distance a secondary electron has to travel to reach the surface of the particle is $l(\phi, x)$. This distance can be derived by applying the law of cosine and sine to the triangle in Fig. 3.3.

$$l(x,\phi) = \left\{ \left(\frac{D}{2}\right)^2 + \left(\frac{D}{2} - x\right)^2 - 2\left(\frac{D}{2}\right)\left(\frac{D}{2} - x\right) \cdot \right. \\ \left. \cdot\cos\left(\phi - \sin^{-1}\left[\left(\frac{2}{D}\right)\left(\frac{D}{2} - x\right)\sin(\phi)\right]\right)\right\} \tag{3.10}$$

The secondary yield δ for a primary electron with energy E_P is now the double integral covering the primary energy deposition and its use for secondary electron emission, as well as the absorption of secondaries traveling within the particle to its surface. The integration

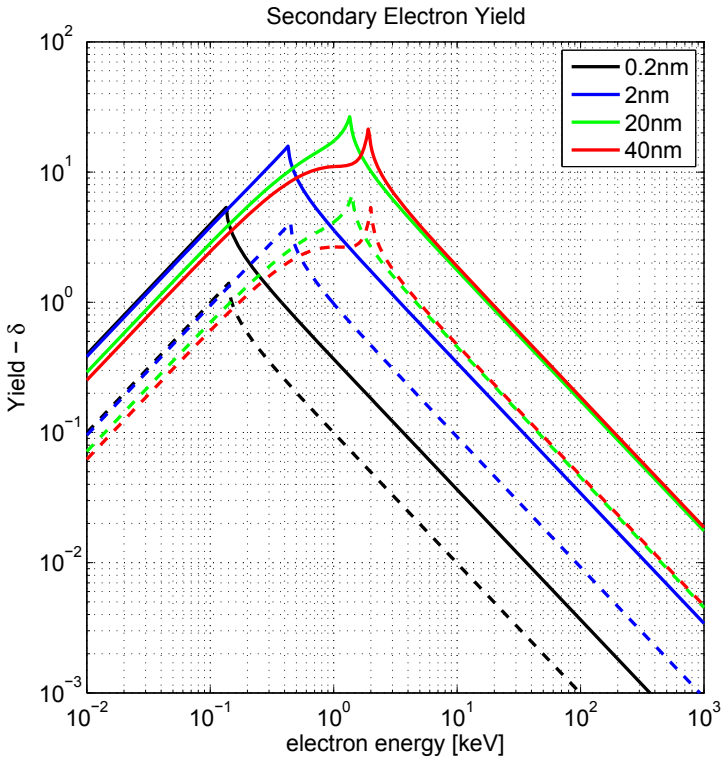

Figure 3.4: Secondary electron yield as a function of primary electron energy for metallic (dashed lines) and isolator (solid lines) particle with different size. Reprinted from Baumann et al. (2016).

is carried out over the penetration depth x and the angle ϕ.

$$\delta(E_\mathrm{P}) = \frac{1}{2} \int_0^{\min[D,x_\mathrm{max}]} K\ a\ [(E_\mathrm{P})^2 - a\ x]^{-1/2} \int_0^{\pi} \frac{1}{2}\sin(\phi) e^{-\alpha l(x,\phi)} \mathrm{d}\phi\ \mathrm{d}x \tag{3.11}$$

Here, a is the Whiddington constant ($1.0{\cdot}10^{14}\,\mathrm{eV^2\,m^{-1}}$ for metal particles, $0.92{\cdot}10^{14}\,\mathrm{eV^2\,m^{-1}}$ for insulator particles), K is the efficiency of using primary electron energy to excite secondary electrons (0.01 for metal particles, 0.04 for insulator particles) and α is the inverse absorption length of secondary electrons ($1.0 \times 10^8\ 1\,\mathrm{m^{-1}}$ within metal particles, 0.93×10^8 $1\,\mathrm{m^{-1}}$ within insulator particles). The numerical values for these parameters originate from calculations of Chow et al. (1993), which are based on experimental data from Bruining (1954) (metals) and Kanaya et al. (1978) (isolators). The integration over the penetration depth x is carried out up to the minimum of either the maximum penetration depth $x_\mathrm{max} = \frac{E_\mathrm{P}^2}{a}$ or the particle diameter D. In the case of small primary electron energies, the electron is fully stopped within the particle and the integration is carried out up to x_max. Though primary electrons with high energies can pass through the particle, in this case the integration limit is the particle diameter D.

Figure 3.4 shows the secondary electron yield as a function of primary electron energy for

insulator and metal material. In this study we have used the yield for insulator particles, as MSPs most likely consist of insulator material (e.g., Rapp et al., 2012). The yield shows maximum values up of to 20 at characteristic energy levels. These energy values correspond to maximum penetration depths in the region of the particle diameter. At lower energies the primary electron is still stopped within the particle and the yield still shows relatively high values. Above these characteristic energies the secondary yield decays exponentially, as the primary electrons deposit only a small fraction of their energy into the excitation of secondary electrons.

The number of secondary electrons leaving a particle of radius r per second depends on the charge of the particle. If the particle carries a negative charge of $Z \cdot e$, the flux of secondary electrons J_{sec} is given by the following (Meyer-Vernet, 1982):

$$J_{\text{sec}} = \pi r^2 \int_{-e\Phi}^{\infty} \frac{\partial j_e}{\partial E} \left(1 + \frac{e\Phi}{E}\right) \delta(E) \mathrm{d}E. \tag{3.12}$$

Here, the integration is carried out over the energy range of the differential flux of primary electrons $\frac{\partial j_e}{\partial E}$ and the secondary yield δ. Φ is the surface potential of the particle of radius r and with charge number Z. The lower limit of the integration is the kinetic energy a primary electron needs to reach the surface of the negatively charged particle.

In the case of positively charged particles, the emitted secondary electrons have to overcome an attractive Coulomb force and the above equation J_{sec} changes as follows:

$$J_{\text{sec}} = e^{-\Phi/k_{\text{B}}T_s} \left(1 + \frac{\Phi}{k_{\text{B}}T_s}\right) \pi r^2 \int_{0}^{\infty} \frac{\partial j_e}{\partial E} \left(1 + \frac{e\Phi}{E}\right) \delta(E) \mathrm{d}E. \tag{3.13}$$

Here, $k_{\text{B}}T_s$ is the kinetic energy of a secondary electron after leaving a particle. The velocity distribution of the secondaries is Maxvellian, and they are in the range of 1 to 5 eV (Goertz, 1989); we have arbitrarily used 3 eV in this study. This value only has an impact on the SEE rate of multiple positively charged particles.

In the following, the SEE formalism for particles is applied to MSPs. These MSPs are not only subject to SEE induced by polar electron precipitation but are also charged within the D-region ionosphere by processes like electron and ion attachment as well as photodetachment and photoionization. The process of ion attachment to MSPs depicts a generalization of different processes on the atomic scale depending on the ion type, i.e., electron transfer, proton transfer, cation attachment and anion attachment. These processes are approached classically by, e.g., Natanson (1960), Fuchs (1963) and Hoppel and Frick (1986) and are generalized into one reaction rate coefficient dependent on temperature, ion mass and charge and MSP charge state (Rapp, 2000).

3.3.2 SEE Application to MSP within the Polar Ionosphere

Secondary electron emission is only relevant at polar latitudes. Here, the Earth's magnetic field lines penetrate into the atmosphere and allow energetic electrons from the magneto-

sphere to enter. These high-energy electrons contribute significantly to the ionization in the lower ionosphere (e.g., Frahm et al., 1997).

In order to make reliable statements on the importance of SEE for the charge state of MSPs within the D region, we model the polar ionosphere with the Sodankylä Ion and Neutral Chemistry (SIC) model (Verronen et al., 2005; Turunen et al., 2009) and compare standard MSP-related charging processes with SEE. The model derives the concentrations of 44 positive ion species, 28 negative ion species and 35 neutral species from 20 to 150 km. The SIC model enables the implementation of different electron precipitation spectra as a source of ionization additional to solar UV and EUV radiation. This study uses the SIC model version with MSPs included into the full ion reaction scheme as recently described in Baumann et al. (2015).

The following analysis is carried out at 90 and 70 km altitude. We have chosen these altitudes for investigating the effectiveness of SEE on the charging of MSPs, because they represent two different states of the lower ionosphere. At 90 km the ionosphere is governed by the presence of free electrons and positive ions only. At 70 km, negatively charged ions can exist in addition to free electrons as another type of negative charge carriers. In addition, the size distributions of MSPs are different at both altitudes. Just after their formation at 90 km altitude, the radii of MSPs are rather small (< 1 nm). During sedimentation down to 70 km, MSPs grow through coagulation to radii > 1 nm (e.g., Megner et al., 2006).

Electron precipitation and D-region conditions

Electron precipitation is often described by the differential flux of electrons $\partial j_e / \partial E$ entering the atmosphere from the magnetosphere. This quantity can be derived from measurements of incoherent-scatter radars and by instruments on board satellites and sounding rockets (e.g., Rees, 1969; Miyoshi et al., 2015, and references therein) and is usually given for the top of the atmosphere. While penetrating the atmosphere, energetic electrons collide with atmospheric molecules; they lose energy and can get absorbed completely. The altitude of complete absorption of the energetic electron depends on electron energy and the density of the atmosphere. Fang et al. (2010) derived a normalized energy deposition f to describe the altitude region where electrons with a certain energy are absorbed. We have adapted this formalism to derive in-situ energetic electron spectra for 70 and 90 km. These spectra are then used in Eqs. (3.12) and (3.13) to derive the secondary electron flux J_{sec}.

In the left panel of Fig. 3.5 the spectra for three different cases of electron precipitation are plotted (different line shapes), namely at the top of the atmosphere, at 90 km altitude and 70 km altitude (different colors). The three cases are defined as follows: the "weak" electron precipitation case is the spectrum measured during a pulsating aurora event over Tromsø (Miyoshi et al., 2015). The "medium" precipitation case corresponds to the "Hard" spectra shown in Osepian and Kirkwood (1996). The electron precipitation of the "strong" case is the medium precipitation case increased by a factor of 100; i.e., this is an unrealistically strong precipitation used as a test case. The medium and strong cases are

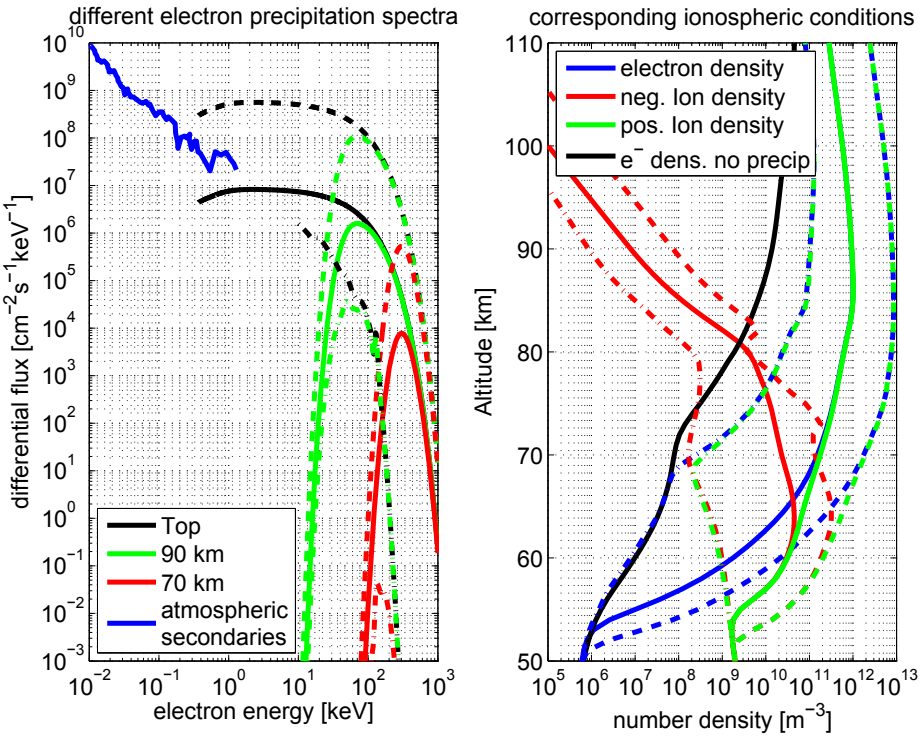

Figure 3.5: (Left) Electron precipitation spectra for weak (dash-dotted, data published in Miyoshi et al. (2015)), medium (solid) and strong (dashed) conditions, spectra at the top of the atmosphere (black) and remnants at 90 km (green) and 70 km (red) and atmospheric secondary electron spectrum measured at 105 km by Doering (data taken from Fig 4. of Pfister, 1967), (Right) corresponding to the precipitation cases the electron density (blue), negative ion density (red) and positive ion density (green) has been modeled using the SIC model together with the electron density (black) for a model run without electron precipitation. Reprinted from Baumann et al. (2016).

Maxwellian spectra of the form

$$\frac{\partial j_e}{\partial E}(E) = \frac{Q_0}{2E_0^3}\exp\left(\frac{-E}{E_0}\right). \tag{3.14}$$

Here Q_0 is the total energy flux of the precipitating electrons and E_0 is the characteristic energy of the spectrum.

In order to get a complete view of the energetic electrons in the Earth's atmosphere, we also consider the fraction of secondary electrons emitted in-situ from the atmospheric species oxygen and nitrogen. As the primary electrons are absorbed within the atmosphere, their kinetic energy is degraded through elastic collision with atmospheric molecules, leading to the emission of atmospheric secondary electrons (Rees et al., 1969). According to laboratory measurements of Opal et al. (1971), the energy distribution of secondary electrons from O_2 and N_2 does not depend on the energy of the primary electrons and is within the sub-kiloelectronvolt energy range. To study the "tertiary" electron emission

(TEE) from MSPs, we have used an atmospheric secondary differential electron flux measured at 105 km altitude under auroral conditions (see Fig. 3.5, data collected by Doering, published within Fig. 4 of Pfister, 1967). Pfister (1967) also shows similar atmospheric secondary differential fluxes for higher altitudes. We assume that this atmospheric secondary electron differential flux is typical at auroral latitudes and also applies to lower altitudes as long as primary electrons are absorbed within these altitudes. The causal primary electron flux for the atmospheric secondary flux shown in Fig. 3.5 is only comparable to the differential flux measured by Miyoshi et al. (2015) within a pulsating aurora (cf. Fig. 2 of Pfister, 1967). This atmospheric secondary flux cannot be used for the other precipitation cases as it depends on the strength of the initial electron precipitation (Rees, 1969). To the author's knowledge, there are no atmospheric secondary electron spectra available whose initial electron precipitation corresponds to the other precipitation cases used in this study.

These three different precipitation cases have been used within the SIC model to determine the state of the lower ionosphere. The aim of this calculation is to put the secondary electron emission into a context of MSP-related charging processes within the D-region ionosphere. In the right panel of Fig. 3.5 the results of these model runs are shown. Here the electron, positive and negative ion densities are plotted in the corresponding line shape of the different precipitation cases of the left panel. The positive and negative ion number density is the the sum of the number densities of the various ion species derived by SIC. In addition, there we also show one electron density profile for comparison, which has been modeled for quiet ionospheric conditions, i.e., in the absence of electron precipitation.

Comparison of MSP-related charging rates and Discussion

The abovementioned three electron precipitation cases are compared to each other, in order to identify whether SEE is an important charging process for MSPs. This comparison includes the discussion of the SEE rates and other MSP-related charging rates, i.e., plasma attachment and charging by solar photons. To derive plasma attachment rates which are equivalent to the SEE rate, the electron and ion number densities modeled with the SIC model are multiplied with the attachment reaction rate coefficients (Natanson, 1960; Rapp, 2000). In addition to the SEE and plasma attachment we also consider photodetachment and photoionization of MSPs in this study. According to Rapp (2009) we assumed Fe_2O_3 (Hematite) to be a plausible MSP analogue and derived the detachment and ionization rates for solar radiation at a solar zenith angle of 66° at the location Tromsø (69° N). Nevertheless, research on the material properties of MSPs is still ongoing and is needed to further constrain the optical characteristics of MSPs.

In the panels of Fig. 3.6 the rates for different MSP sizes are plotted for the processes of plasma attachment to neutral MSPs, photodetachment of negatively charged MSPs, photoionization of neutral MSPs and the secondary electron emission from neutral MSPs induced by primary electrons (secondary) and atmospheric secondary electrons (tertiary). As discussed earlier, the rates for these processes are derived on the basis of three different precipitation cases and the corresponding ionospheric modeling. The process rates have been derived for the altitudes 90 and 70 km.

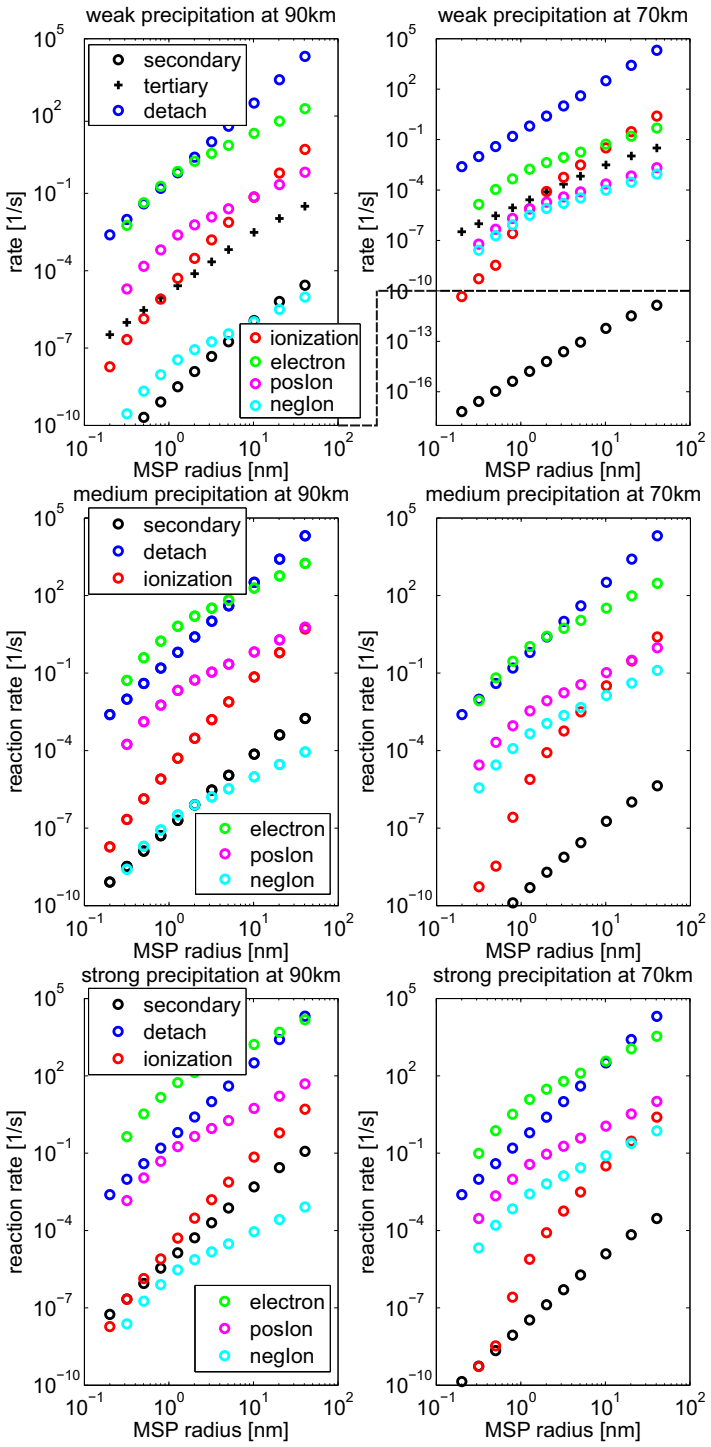

Figure 3.6: Charging rates of different particle sizes corresponding to the weak (top), medium (middle) and strong (bottom) electron precipitation case for secondary electron emission (black), particle ionization (red), electron detachment from negatively charged particles (blue) as well as electron (green), negative (cyan) and positive ion attachment (magenta) for ionospheric conditions at 90 km (left) and 70 km (right) altitude. Reprinted from Baumann et al. (2016).

For the case of SEE induced by primary electron precipitation the energy of the energetic electrons is so high that they pass through the MSP and deposit only a small fraction of their energy into the MSP; here the SEE yields are far below one (compare Fig. 3.4). Moreover, the SEE rate from MSPs shows in general a size dependency. The huge difference of several orders of magnitude of the SEE rate between the smallest (0.2 nm) and biggest particles (40 nm) has two main reasons. Firstly, the SEE yield is a function of particle size for high primary electron energies; namely it is more then one order of magnitude smaller for 0.2 nm MSPs then for 40 nm particles.

Secondly, the SEE rate grows with the square of the MSP radii (compare Eq. 3.12).

Concerning electron precipitation, the absorption of energetic electrons is already strong down to 90 km; only electrons with energies higher than 10 keV can reach this altitude. For 70 km altitude this value is 100 keV. This absorption limits the available number of energetic electrons for SEE from MSPs, resulting in significantly lower SEE rates at 70 km compared to 90 km.

There is also absorption of solar photons within the Earth's atmosphere that leads to different solar spectra available for photodetachment and photoionization of MSPs at 70 and 90 km. This UV photon absorption leads to a reduction of the photoionization rates at 70 km by a factor of 3 compared to 90 km. For the photodetachment this reduction is even smaller, since also photons of lower energies within the visible spectrum can detach electrons from negatively charged MSPs. These photons are not at all absorbed by the atmosphere, and as a consequence the photodetachment rate shows only a small reduction at the second decimal place, i.e., due to UV absorption (e.g., Rapp, 2009). The photodetachment and photoionization of MSPs do not change for different electron precipitation cases.

The attachment rate of ions and electrons to neutral MSPs varies with every precipitation case and altitude; i.e., the rate is given by the product of reaction rate coefficient and plasma number density (see Fig. 3.5 right panel). We have decided to show only the neutral case of the possible attachment of plasma to neutral MSPs. The reaction rate coefficients for the repulsive case of plasma attachment to identically charged particles are many orders of magnitude smaller compared to the reaction rate coefficients for the charging of neutral MSPs and hence can be neglected. Moreover, the reaction rate coefficient of the attractive case of plasma attachment to MSPs is of the same order of magnitude as the neutral case (Rapp, 2000). Showing these in Fig. 3.6 does not provide additional information.

The general comparison of the process rates concerning charging of MSPs in Fig. 3.6 shows that in all studied precipitation cases and at both altitudes the rates of the electron attachment to neutral MSPs and the photodetachment of negatively charged MSPs are the governing processes for the charge state of MSPs. The process rates of secondary electron emission, neither induced by primary electrons (i.e., SEE) nor induced by atmospheric secondary electrons (i.e., TEE), are several orders of magnitude below these attachment and detachment processes.

A detailed comparison at 90 km for the weak and medium precipitation cases shows that the SEE rate from neutral MSPs is of the same magnitude as the attachment rate of negative ions to MSPs. In the strong precipitation case the SEE rate even overcomes the

negative ion attachment rate to MSPs. As the additional ionization by electron precipitation grows from the weak case to the strong case, the additional free electrons lead to the production of more negative ions even above 80 km, where the presence of atomic oxygen usually destroys negatively charged ions effectively. At the same time the SEE rate grows as the available amount of energetic electrons present at 90 km increases with the strength of the electron precipitation. In the strong precipitation case the SEE rate reaches nearly the MSP photoionization process rate. But the SEE rate at 90 km is several orders of magnitude lower than the attachment of positive ions and electrons to MSPs as well as the very effective photodetachment of negatively charged particles in all three precipitation cases.

At 70 km the SEE rate induced by primary electrons is even smaller as there are fewer available energetic electrons. In the weak and medium precipitation case the SEE rate lies far below all other process rates. Even the attachment of negative ions is much greater, since the number density of negative ions at 70 km is much higher. The strong precipitation case shows SEE rates for small MSPs as high as the photoionization rates, but these values are not really relevant as at 70 km altitude these small MSPs exist only sparsely (e.g., Megner et al., 2006). For greater MSP sizes SEE does not reach any other MSP charging rate either in the weak and medium case or in the strong precipitation case.

The question now is how often SEE from MSPs occurs in the the polar ionosphere. We have studied three precipitation cases, of which the weak and medium cases happen in the polar atmosphere and the strong case has more the nature of a thought experiment with extraordinarily severe electron precipitation. The electron precipitation for pulsating aurora (weak case), caused by energetic electrons with tens of kiloelectronvolts of energy (Miyoshi et al., 2015), occurs frequently during minor geomagnetic activity. Furthermore, electrons trapped within the Earth's magnetosphere can be accelerated to relativistic energies (e.g., Reeves et al., 2013), which can be injected into the Earth's atmosphere during geomagnetic storms; this scenario is comparable to our medium precipitation case. This has the following consequences for the occurrence of the effect of SEE during different electron precipitation cases: the weak precipitation case causes, despite the relatively frequent occurrence, a SEE effect on MSPs that is marginal compared to other MSP-related charging processes. The medium precipitation case occurs sparsely during 1 year, and the effect of SEE on the charge of MSPs is still small. Even an unrealistic increase of the electron precipitation results in SEE rates which are still not significant for the charge state of MSPs.

The consideration to study the TEE process originated from two facts. Firstly, the secondary electron yield at energetic electron energies below 1 keV is about one order of magnitude higher than the yield at energies above 10 keV (cf. Fig. 3.4). Secondly, the atmospheric secondary differential flux is also much higher than the available primary electron flux at 90 and 70 km. It turns out that the TEE rate is higher than the SEE rate but still two orders of magnitude lower than the electron attachment to MSPs and photodetachment of negatively charged MSPs. The derived TEE rate is only valid within the weak precipitation case, because the used atmospheric secondary flux corresponds to a primary electron flux that is comparable to the weak precipitation case. Therefore,

the TEE rate is only plotted in the weak precipitation panels of Fig. 3.6. The tertiary electron emission rate shows a smaller size dependence, this is because within the sub-kiloelectronvolts electron energy range the secondary yield is independent of the MSP sizes. This is because the electrons deposit all their kinetic energy into the MSPs within this energy range. At the altitude of 90 km, the TEE rate is only comparable to the photoionization rate and exceeds the negative ion attachment rate but cannot reach the positive ion attachment rate. At 70 km, the TEE rate is of the same order of magnitude as the positive and negative ion attachment rates as well as the photoionization rate.

It has to be noted that the nature of the tertiary electron emission is unsettled at the moment. In particular, the differential flux of atmospheric secondary electrons at altitudes below 100 km and for different kinds of electron precipitation strengths is not known. In addition, we assume for TEE from MSPs that the atmospheric secondary electrons have to have at least 10 eV of kinetic energy in order to enter a MSP and excite an electron that has enough energy to leave the particle. Therefore, our quantification of the TEE rate can be seen as a rough estimate only. Furthermore, we think that MSP charging by TEE cannot be of the same importance as electron attachment to MSPs. The existence of an atmospheric secondary electron flux more than three orders of magnitude higher than used in this study, in order to come up with TEE rates comparable to the electron attachment rates, is not plausible.

3.3.3 Conclusions

Energetic particle precipitation is a common phenomenon occurring within the polar latitudes and especially affects the lower ionosphere. As shown in Fig. 3.6, electron precipitation enhances the number density of plasma components by several orders of magnitude. In this study we examined secondary electron emission from meteoric smoke particles. MSPs are produced and exist within the same altitude region of 70 to 110 km, where precipitating electrons deposit a substantial amount of their energy. Here, these MSPs can be subject to secondary electron emission induced by this energetic particle precipitation (SEE). We have studied the effect of SEE from MSPs within the polar ionosphere and compared this charging process with other MSP-related charging mechanisms in the D-region and lower E-region ionosphere. To derive realistic SEE rates, we have used in-situ energetic electron spectra and a SEE yield for particles (Chow et al., 1993). The ionosphere has been characterized by the SIC model including the weak, medium and strong electron precipitation cases which have been studied in more detail.

It is also possible that atmospheric secondary electrons from gaseous components can cause tertiary electron emission from MSPs. The TEE rates have been derived from an atmospheric secondary electron differential flux measured at 105 km altitude (Pfister, 1967) using the same yield formalism. However, the robustness of the TEE results is rather weak, as atmospheric secondary electron spectra at lower altitudes and the corresponding primary electron spectra are not available. Additional in-situ and laboratory experiments are needed for a solid quantification of the TEE effect.

Concerning the charge state of MSPs, the processes SEE and TEE do not play a sig-

nificant role in all three considered precipitation cases at the studied altitudes of 70 and 90 km. In general, the direct response of the polar ionosphere on electron precipitation, i.e., an enhancement of the number density of plasma components due to additional ionization in the ionosphere, is the main driver for the charge state of MSPs. The charging of MSPs through electron attachment and decharging through photodetachment of negatively charged MSPs are the relevant processes.

Nevertheless, there might be an influence of SEE and TEE from MSPs through the production of additional electrons in the lower ionosphere. That could be of interest to explain unresolved phenomena within the polar atmosphere during energetic electron precipitation.

4 Chargebalance in the D-region

This chapter concentrates on the role of MSPs on the charge balance of the D-region ionosphere. It contains Sect. 4.1 which describes the status of experimental measurements of the D-region charge balance. Furthermore, Sect. 4.2 describes a simplified ionospheric model of the D-region, whose processes connect MSPs with the electrons and ions of the ionosphere. The model results are analyzed especially for nighttime conditions (Sect. 4.2.2). By applying an aerodynamical filter to the modelled results (Sect. 4.2.3), a comparison with observations becomes possible. Sect. 4.3 identifies the relevant processes for the nighttime state of the D-region ionosphere. The conclusions of this model study are drawn in Sect. 4.4.

This chapter has been already published within Baumann et al. (2013), only minor editorial changes have been applied.

4.1 In-Situ Plasma Measurements - MSP influence on the charge balance

This section summarizes the results of rocket borne experiments concerning the D-region charge balance. This includes the discussion measurements of charged MSPs by Faraday Cups (see Fig. 2.5), of the electron density by the Faraday rotation method (e.g., Mechtly et al., 1967) and of the positive ion density by electrostatic probes (e.g., Thrane and Grandal, 1981).

A very interesting point is that the measured peak charge number density of negatively charged MSPs can reach values of several $10^8\,\mathrm{e\,m^{-3}}$ between 85 and 90 km (see Fig. 2.5). These values are comparable to the electron densities in this altitude region. Taking into account that the Faraday cup measurements underlie aerodynamical filtering (Hedin et al., 2007; Strelnikova et al., 2009 and Sect. 4.2.3)) it is possible that in some cases the real negative MSP number density even outnumbers the electron number density. Therefore it is possible that, negatively MSP rather than electrons conserve the charge balance together with positively charged ion in this altitude region.

To support the speculation that MSP have an influence on the D-region charge balance, we refer to simultaneous measurements of electron and positive ion number density from Friedrich et al. (2012). These measurements were conducted during the last five rocket flights listed in Table 2.1. The electron number densities were measured by the radio wave propagation method, while a fixed biased DC-probe (positive ion probe – PIP) was used to quantify the positive ion density (e.g., Mechtly et al., 1967; Friedrich et al., 2013). Due to different levels of Ly-α ionisation the plasma densities differ in some cases by up to one order of magnitude. In order to be able to better interpret these five data sets and

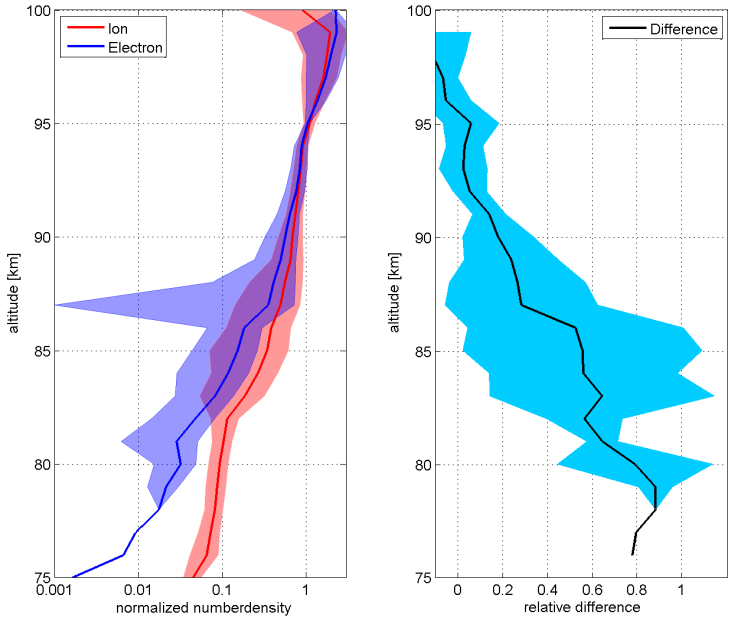

Figure 4.1: Left panel: mean normalized electron density (black) and positive ion density (red) profiles from in-situ measurements of Friedrich et al. (2012) with the corresponding standard deviation, the electron density at 95 km for each rocket flight has been used for normalization of electron and ion density. The standard deviation of the normalized electron densities exceeds the mean value at 88 km. Right panel: relative difference between electron and positive ion density. Reprinted from Baumann et al. (2013).

to demonstrate the robustness of the deviation from local charge neutrality due to the presence of MSP, we normalize the corresponding plasma densities. This means, we divide all plasma measurements by the corresponding electron density value measured at 95 km. We show the mean values of electron and positive ion number density together with their standard deviation in the left panel of Fig. 4.1 and the relative difference between electron and positive ion density in the right panel of Fig. 4.1. The variability of the electron and ion profiles (indicated by the shaded area around the means) is very large down to ∼80 km, i.e., the standard deviation of both quantities overlap. Nevertheless, there is a significant difference between the electron and positive number ion densities below ∼85 km. This is clearly seen in the right panel of Fig. 4.1, which shows the relative difference between both quantities, e.g., the difference between the normalized number densities relative to the normalized ion number density $((N_\mathrm{I}^\mathrm{R} - N_\mathrm{e}^\mathrm{R})/N_\mathrm{I}^\mathrm{R}$, the R stands for relative), along with its standard deviation.

In the Earth's D-region ionosphere the concept of quasineutrality is generally valid, i.e., the sum of all charges in a volume larger than a Debye-sphere is zero. In Fig. 4.1 (left panel) this quasineutrality is obvious above 95 km, where electron and positive ion density are the same. However, below 95 km quasineutrality is obviously no longer maintained by

electrons and positive ions alone. Other negative charge carriers have to be considered below this altitude in addition to electrons. As a first guess negative ions could possibly be this negative charge carrier. However, it is well known that negative ions are destroyed by reaction with atomic oxygen (e.g., Turunen et al., 1996) down to ∼80 km and a significant atomic oxygen concentration is regularly observed above ∼80 km by satellite, airglow and sounding rocket measurements (e.g., Russell et al., 2005; Friedrich et al., 2012). Therefore the negative ions can only explain the measured deviation between electron and positive ion density below ∼80 km. In between ∼80 km and 95 km there must be another negative charge carrier to conserve quasineutrality. And indeed, we find negatively charged MSP in this altitude range (see Fig. 2.5). In the following we want to check the assumption of Friedrich et al. (2012) that MSP are a sink for electrons. We do that by applying a simple ionospheric model where we include MSP as active constituents. The model and some initial results are described in the following sections.

4.2 Model study of the charge balance of MSP

4.2.1 Model description

Recent ionospheric models concerning the D-region, such as the Sodankylä Ion and neutrals Chemistry (SIC) model (Turunen et al., 1996), do not consider MSP in their calculations. As described above, however there is strong experimental evidence for MSP influence on the D-region charge balance. Because of this, we present a simple ionospheric model, which also covers MSP, for the altitude region 60–100 km. This model includes six species: electrons, positive ions, negative ions, neutral MSP, positive MSP and negative MSP. We note that using only six species means a significant idealization of the very complex D-region ion chemistry. However, the reaction rates and masses of molecular and cluster ions are still very different from the corresponding mass and reaction rates of MSP. Hence it appears warranted to categorize the various plasma species into electrons, positive ions and negative ions and MSP in order to study the qualitative effect of MSP on the partitioning of charge between these various species.

The reaction scheme for all six components includes thirteen different reactions overall. In the following chemical reactions P, P_p and P_n denote neutral, positive, and negative MSP, respectively, while e^-, I^+ and I^- represent electrons, positive ions and negative ions, respectively. These reactions can be divided into three different groups. The first group describes the ionospheric background covering standard plasma reactions, e.g., like the electron-ion pair production rate Q. The reaction rate coefficients $k_1^\mathrm{S} - k_5^\mathrm{S}$ are taken from the SIC model, which is – to our knowledge – one of the currently most advanced D-region models.

$$(\mathrm{M} + \mathrm{h}\nu) \xrightarrow{\mathrm{k}_1^{\mathrm{S}}} \mathrm{e}^- + \mathrm{I}^+ \quad \text{(R 4.1)}$$

$$\mathrm{e}^- + \mathrm{I}^+ \xrightarrow{\mathrm{k}_2^{\mathrm{S}}} (\mathrm{M}) \quad \text{(R 4.2)}$$

$$\mathrm{e}^-(+\mathrm{M}) \xrightarrow{\mathrm{k}_3^{\mathrm{S}}} \mathrm{I}- (+\mathrm{M}) \quad \text{(R 4.3)}$$

$$\mathrm{I}^-(+\mathrm{M}/\mathrm{h}\nu) \xrightarrow{\mathrm{k}_4^{\mathrm{S}}} \mathrm{e}- (+\mathrm{M}) \quad \text{(R 4.4)}$$

$$\mathrm{I}^+ + \mathrm{I}^- \xrightarrow{\mathrm{k}_5^{\mathrm{S}}} (\mathrm{M}) \quad \text{(R 4.5)}$$

The reaction rate coefficient k_1^{S}, k_3^{S} and k_4^{S} are already multiplied by the corresponding neutral densities (M) since the simple model does not consider neutral constituents in its calculations. In addition, it has to be noted that k_4^{S} describes the combination of photo detachment and collisional detachment of electrons from negative ions. The combination is carried out in the following way:

$$k_4^{\mathrm{S}} = k_{\mathrm{photo}} + k_{\mathrm{col.}} \cdot [\mathrm{M}]. \quad (4.1)$$

Here k_{photo} is the photo detachment rate coefficient, $k_{\mathrm{col.}}$ is the collisional detachment rate coefficient and [M] denote the density of atomic oxygen, H_2, O_3, NO and other minor species colliding with the negative ions. Note that in the height region above 80 km the collision with atomic oxygen is the main sink for negative ions. The used atomic oxygen profile is derived within the SIC model which is shown in the right panel of Fig. 4.2.

The second group of reactions are plasma capture reactions by MSP.

$$\mathrm{P} + \mathrm{e}^- \xrightarrow{\mathrm{k}_6^{\mathrm{C}}} \mathrm{P_n} \quad \text{(R 4.6)}$$

$$\mathrm{P} + \mathrm{I}^+ \xrightarrow{\mathrm{k}_7^{\mathrm{C}}} \mathrm{P_p} \quad \text{(R 4.7)}$$

$$\mathrm{P_n} + \mathrm{I}^+ \xrightarrow{\mathrm{k}_8^{\mathrm{C}}} \mathrm{P} \quad \text{(R 4.8)}$$

$$\mathrm{P_p} + \mathrm{e}^- \xrightarrow{\mathrm{k}_9^{\mathrm{C}}} \mathrm{P} \quad \text{(R 4.9)}$$

$$\mathrm{P} + \mathrm{I}^- \xrightarrow{\mathrm{k}_{10}^{\mathrm{C}}} \mathrm{P_n} \quad \text{(R 4.10)}$$

$$\mathrm{P_p} + \mathrm{I}^- \xrightarrow{\mathrm{k}_{11}^{\mathrm{C}}} \mathrm{P} \quad \text{(R 4.11)}$$

Finally, the third group of reactions are MSP photo reactions which also occur during the nighttime due to Ly-α photons resonantly scattered by the geocorona.

$$\mathrm{P_n} + \frac{h \cdot c}{\lambda\_1^*} \xrightarrow{\mathrm{k}_{12}^{\mathrm{P}}} \mathrm{P} + \mathrm{e}^- \quad \text{(R 4.12)}$$

$$\mathrm{P} + \frac{h \cdot c}{\lambda\_2^*} \xrightarrow{\mathrm{k}_{13}^{\mathrm{P}}} \mathrm{P_p} + \mathrm{e}^- \quad \text{(R 4.13)}$$

Table 4.1: Description of the thirteen reaction rate coefficients, their units in the model and reference of their origin. Reprinted from Baumann et al. (2013).

k_n	Unit	Comment	Reference
k_1^S	$m^{-3}\,s^{-1}$	ionization	SIC res.: Turunen et al. (1996)
k_2^S	$m^3\,s^{-1}$	dissociative recomb.	SIC res.: Turunen et al. (1996)
k_3^S	s^{-1}	electron attach. to neutrals	SIC res.: Turunen et al. (1996)
k_4^S	s^{-1}	electron detach. from neg. ions.	SIC res.: Turunen et al. (1996)
k_5^S	$m^3\,s^{-1}$	ion-ion recomb.	SIC res.: Arijs et al. (1987)
k_6^C	$m^3\,s^{-1}$	electron attach. to MSP	Rapp (2000), Natanson (1960)
k_7^C	$m^3\,s^{-1}$	pos. ion attach. to MSP	Rapp (2000), Natanson (1960)
k_8^C	$m^3\,s^{-1}$	pos. ion attach. to MSP-	Rapp (2000), Natanson (1960)
k_9^C	$m^3\,s^{-1}$	electron attach. to MSP+	Rapp (2000), Natanson (1960)
k_{10}^C	$m^3\,s^{-1}$	neg. ion attach. to MSP	Rapp (2000), Natanson (1960)
k_{11}^C	$m^3\,s^{-1}$	neg. ion attach. to MSP+	Rapp (2000), Natanson (1960)
k_{12}^P	s^{-1}	MSP- electron detach.	Rapp (2009)
k_{13}^P	s^{-1}	MSP ionization	Rapp (2009)

To start, Table 4.1 summarizes all relevant information about the 13 reaction rates used in this study. That is, the meaning of all reaction rate coefficients is specified, and their units together with the original references are given.

We use the output of the SIC-model for a realistic background ionosphere. SIC derives concentrations of 88 constituents, i.e., 44 positive ion species, 28 negative ion species and 16 neutral species. In Fig. 4.2 the density of important negative and positive ions in the D-region are shown. It has to be noted that the altitude range of the SIC model is 20–150 km, but in this study we focus on the region between 60–100 km where significant number densities of MSP exist (e.g., Hunten et al., 1980).

As stated above, the SIC model simulates the number density of several positive ions, negative ions and minor neutrals. As input, the SIC model uses the background neutral atmosphere from the MSISE-90 model (Hedin, 1991) and a solar spectrum from the Solar Irradiance Platform (former Solar 2000 (Tobiska et al., 2000)). The electron density N_e is deduced from the difference between the sum of all positive ions (N_{I^+}) and the sum of all negative ions (N_{I^-}).

$$N_e = N_{I^+} - N_{I^-} \tag{4.2}$$

The SIC model uses many different ion reactions, which we have summarized in the reaction rate coefficients k_1^S-k_5^S. k_1^S represents the ionization of neutrals by solar radiation and galactic cosmic rays, i.e., quiet-day conditions. Electron and proton precipitation,

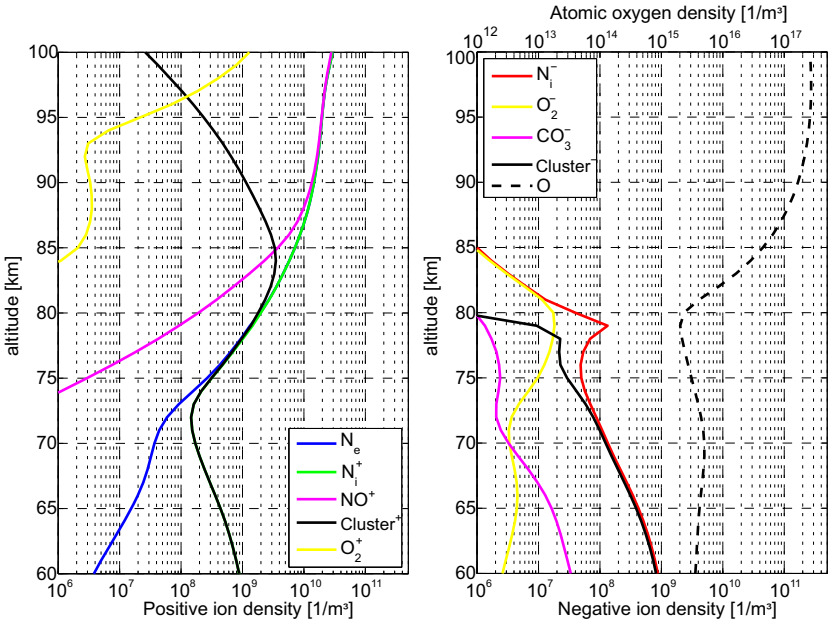

Figure 4.2: Density profiles of selected positive ions and electrons (left) and density profiles of negative ions together with the atomic oxygen profile (right); Cluster$^{+/-}$ means the sum of all cluster ions, $N_i^{+/-}$ denotes the sum of all ions, for 8th September 2010, 23:55 LT, 69°N, 16°E. Reprinted from Baumann et al. (2013).

caused by solar proton events or coronal mass ejections, can increase the ionization levels of the D-region by two orders of magnitude, but are not believed to change the qualitative correctness of our results. The generalization of reaction rate coefficients $k_2^{\mathrm{S}} - k_5^{\mathrm{S}}$ has been done by taking the means of all corresponding single ion reactions in the SIC model, which has been weighted also by each ion density. The reactions rate coefficients k_2^{S}, k_3^{S} and the collisional part of k_4^{S} are multiplied by the neutral densities corresponding to each chemical reaction in SIC. For k_4^{S} this is mainly atomic oxygen, together with some minor constituents like H_2, O_3 and NO. It has to be noted that the generalization of the electron – positive ion recombination for molecular and cluster ions, which differ significantly, might be inappropriate. As seen in Fig. 4.2, however, the transition region between the molecular ion regime and the cluster ion regime is vertically very isolated around 85 km.

The SIC model has been run for a geographical location of 69° N and 16° E (Andenes, Norway), since most of the rocket flights were conducted from there. The time frame of the SIC run was set somewhat arbitrarily to the 8 September 2010, because there are partly sunlit and dark conditions during the same day and because one of the rocket flights, ECOMA01 (see the MSP profile Fig. 2.5), was conducted on this day of the year. Since SIC is a time-dependent model intended for studying short-lived ionization events, such as energetic particle precipitation, it is standard practice to set it up for a certain date and location by running a full 24 h cycle with only sunlight and cosmic rays as ionization sources. This is repeated several times until a quasi-steady state is reached. Since rocket

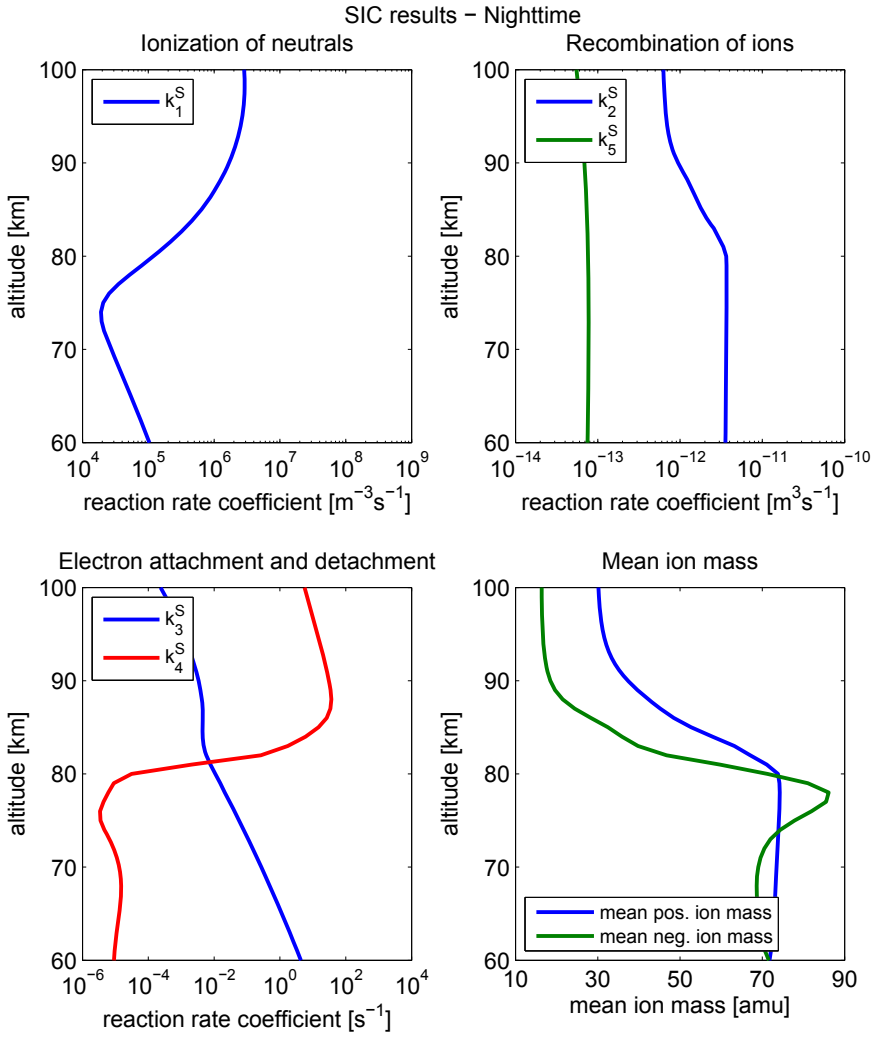

Figure 4.3: Input reaction rate coefficients $k_1^S - k_5^S$ in the appropriate form for the use in the described model (see Table 4.1 for details), note k_1^S is the absolute ionization rate due to solar radiation and galactic cosmic rays; also shown is the mean ion mass, from SIC model results, for the 8th September 2010, 23:55 LT, 69°N, 16°E. Reprinted from Baumann et al. (2013).

measurements observe variations of the electron density during the nighttime of up to two orders of magnitude (e.g., Friedrich et al., 2012), there have to be sources of additional ionization during quiet ionospheric conditions at polar latitudes. This is most likely electron and proton precipitation from the radiation belts, which is also directly linked to the solar activity. In order to provide a quantitative assessment of the error introduced by our assumption of a quiet ionosphere, additional simulations will be required which should be done in the future using the full SIC-model. In Fig. 4.3 we show output variables from this SIC model run which we will further use in the simple model containing MSP reactions below. Besides the reaction rate coefficients $k_1^{\mathrm{S}} - k_5^{\mathrm{S}}$. It is important to remark, that these reaction rate coefficients represent a quiet background ionosphere, which allows us to derive absolute number densities of all six modelled constituents in a qualitative manner. For a quantitative comparison with measurements more realistic profiles of the ionization rate, etc., would be required – corresponding information is, however, not available. Finally, we take the altitude-dependent mean ion mass from SIC, which enters the expressions for the various ion-capturing processes by MSP (see Eqs. 3.1 and 3.3).

The plasma-capturing reactions of MSP (see 3.1–3.3) were reexamined by Rapp (2000) for use in the mesosphere. Originally, these equations were presented by Natanson (1960). In general, this theory provides capture rates for all conceivable combinations of aerosol and ion/electron charges. Here we only consider the attractive case (plasma captured by oppositely charged MSP) and the neutral case (plasma captured by neutral MSP) and neglect the repulsive case. This is a reasonable simplification for the case of MSP, whose size is so small that multiply charged particles can basically not occur (e.g., Rapp and Lübken, 2001). Section 3.1 contains a description of the formulas used to derive capture rate coefficients k_6^C-k_{11}^C. These rate coefficients depend on the temperature of the captured ionospheric components. Within this study, the temperature within the D-region is given by the NRLMSISE-00 model (Picone et al., 2002). The D-region ionosphere has the characteristic that all charged constituents are thermalized to the neutral temperature.

MSP are also influenced by electromagnetic radiation of sufficiently short wavelengths (as discussed in the following) from X-rays and hard UV up to the visible range. Negatively charged MSP can lose an electron due to photo detachment and neutral MSP can be photo-ionized. In this study we concentrate on nighttime conditions. Therefore the sun does not play a significant role, but due to the hydrogen layer in the upper atmosphere (geocorona), solar Ly-α radiation is resonantly scattered from the sunlit side into the dark side of the Earth. Section 3.2 shows how the electron photodetachment rates k_{12}^{P} as well as photo ionization rates k_{13}^{P} are calculated. These reaction rates are derived altitude and MSP size dependent and are derived under the assumption that Fe_2O_3-hematite is the composition of MSPs.

In our ionospheric model we use the altitude-dependent MSP size distribution from Megner et al. (2006) (see Fig. 4.4). Therefore all the described MSP reaction rate coefficients are derived size and height dependent. By doing so we can make statements on the influence of MSP on the charge balance in altitude range between 60 and 100 km. Due to the atmospheric circulation MSP are transported from the summer mesosphere to the winter stratosphere (Megner et al., 2008). As stated above, this study is considering

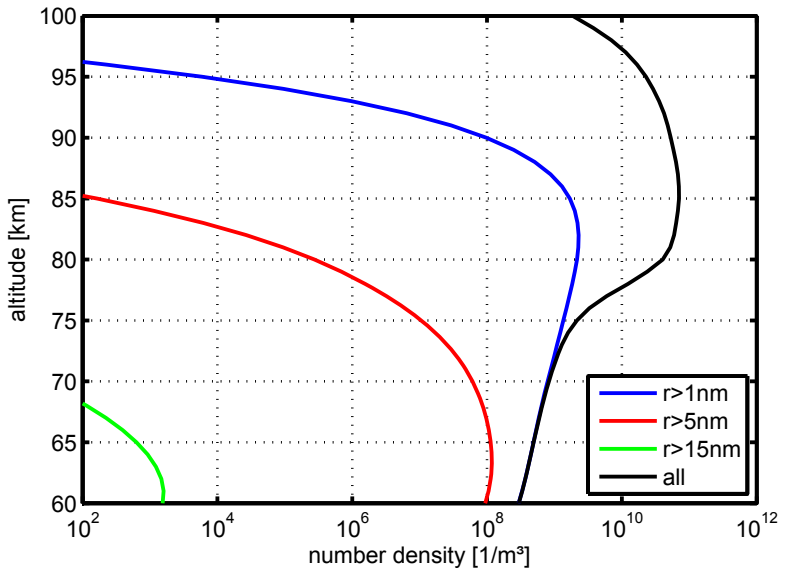

Figure 4.4: Sum of MSP number densities for particle sizes greater than 1 nm (blue), 5 nm (red) and 15 nm (green) and all MSP (black), from the model of Megner et al. (2006). Reprinted from Baumann et al. (2013).

September conditions motivated by the availability of MSP data. As it turns out, this time of the year is least sensitive to circulation effects such that the one-dimensional model results of Megner et al. (2006) can be used. For further study of different parts of the seasonal cycle it is necessary to use MSP distributions from Megner et al. (2008) to account for the meridional transport of MSP in the atmosphere. This will be done in future investigations.

The following rate equations for all six modelled constituents describe the reaction kinetics as treated in the model. The model itself solves these rate equations time dependently to reach a steady state by using the mathematical methods which are also used in the SIC model. The ion and electron densities in Fig. 4.2 and the neutral MSP densities for each size bin are used as initial values for the ionospheric model. The quantities in brackets denote the concentrations of the abovementioned six model constituents.

$$\frac{\partial[e^-]}{\partial t} = k_1^{\mathrm{S}} + k_4^{\mathrm{S}}[I^-] + k_{12}^{\mathrm{P}}[P_{\mathrm{n}}] + k_{13}^{\mathrm{P}}[P] - k_2^{\mathrm{S}}[e^-][I^+] - k_3^{\mathrm{S}}[e^-] - k_6^{\mathrm{C}}[P][e^-] - k_9^{\mathrm{C}}[P_{\mathrm{p}}][e^-] \tag{4.3}$$

$$\frac{\partial[I^+]}{\partial t} = k_1^{\mathrm{S}} - k_2^{\mathrm{S}}[e^-][I^+] - k_7^{\mathrm{C}}[P][I^+] - k_8^{\mathrm{C}}[P_{\mathrm{n}}][I^+] - k_5^{\mathrm{S}}[I^+][I^-] \tag{4.4}$$

$$\frac{\partial[I^-]}{\partial t} = k_3^{\mathrm{S}}[e^-] - k_4^{\mathrm{S}}[N_i n] - k_{10}^{\mathrm{C}}[P][I^-] - k_{11}^{\mathrm{C}}[P_{\mathrm{p}}][I^-] - k_5^{\mathrm{S}}[I^+][I^-] \tag{4.5}$$

$$\frac{\partial[P]}{\partial t} = k_8^{\mathrm{C}}[P_{\mathrm{n}}][I^+] + k_9^{\mathrm{C}}[P_{\mathrm{p}}][e^-] + k_{12}^{\mathrm{P}}[P_{\mathrm{n}}] + k_{11}^{\mathrm{C}}[P_{\mathrm{p}}][I^-] - k_6^{\mathrm{C}}[e^-][P] - k_7^{\mathrm{C}}[I^+][P] - k_{13}^{\mathrm{P}}[P] - k_{10}^{\mathrm{C}}[P][I^-] \quad (4.6)$$

$$\frac{\partial[P_{\mathrm{p}}]}{\partial t} = k_7^{\mathrm{C}}[I^+][P] + k_{13}^{\mathrm{P}}[P] - k_9^{\mathrm{C}}[P_{\mathrm{p}}][e^-] - k_{11}^{\mathrm{C}}[P_{\mathrm{p}}][I^-] \quad (4.7)$$

$$\frac{\partial[P_{\mathrm{n}}]}{\partial t} = k_6^{\mathrm{C}}[e^-][P] + k_{10}^{\mathrm{C}}[P][I^-] - k_8^{\mathrm{C}}[P_{\mathrm{n}}][I^+] - k_{12}^{\mathrm{P}}[P_{\mathrm{n}}]. \quad (4.8)$$

In the next section we present MSP model results for nighttime conditions in which the described in-situ measurements have been made. Additionally, for the later analysis of the model results we compare the reaction rates corresponding to the production and loss processes of the rate Eqs. (4.3)–(4.8) by using this nomenclature.

4.2.2 Nighttime results

In Sect. 4.1 we argued for an influence of MSP on the charge balance in the altitude region between 80 and 95 km based on the evidence from rocket-borne measurements. As a next step, these arguments will be tested with the simple ionospheric model including the MSP described above.

The geophysical conditions we have modelled here are for the 8 September at Andøya (69° N, 16° E), which is identical to the ECOMA-01 flight (Strelnikova et al., 2009). As mentioned above, this date allows us to analyze day and night conditions, while we concentrate on the nighttime results in this study. Eqs. (4.3)–(4.8) are solved time dependently with the initial conditions as shown in Figs. 4.3 and 4.4.

Figure 4.5 shows altitude profiles for all considered species. In the altitude region between 80 and 95 km negatively charged MSP take over the role of electrons and balance the positive charge of the positive ions to achieve quasineutrality. This means that we can confirm the suggestion from rocket-borne observations that MSP have a significant influence on the charge balance in that height region. In addition, parallel to the negative MSP, there are also positive MSP at all modeled altitudes, but the concentration of the latter is much smaller down to 75 km. Below that height negative and positive MSP surprisingly have the same densities. To interpret the results in Fig. 4.5, we show in Fig. 4.6 the MSP-related reaction terms as described in the rate Eqs.(4.6)–(4.8).

From Fig. 4.6, it is obvious that the neutral MSP capture rate of electrons is very important above 80 km, i.e., electrons attach very rapidly to the neutral MSP. This process is balanced by positive-ion capture through negative MSP, i.e., the recombination rate of negative MSP with positive ions is equally fast. This happens despite the fact that the reaction rate coefficients of ions captured by MSP are much smaller compared to electron-capturing coefficients. This contradiction can be explained by the very high concentrations of negative MSP and positive ions as shown in Fig. 4.5. Due to the fact that there is no additional electron production process in the MSP height, there is hardly any importance of electrons for the conservation of the charge balance here.

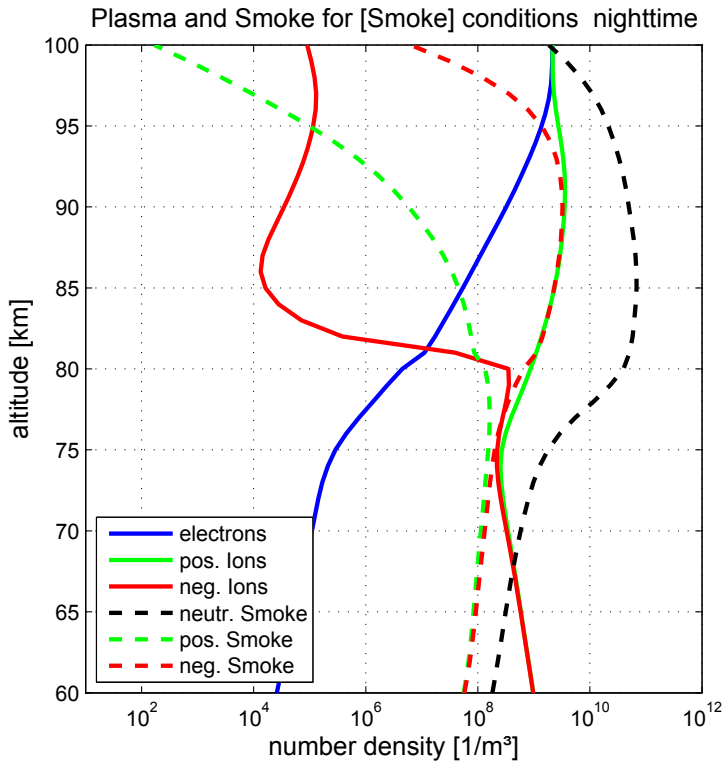

Figure 4.5: Height profiles of the six modelled species, electrons, positive ions, negative ions, neutral MSP, positive MSP and negative MSP. Reprinted from Baumann et al. (2013).

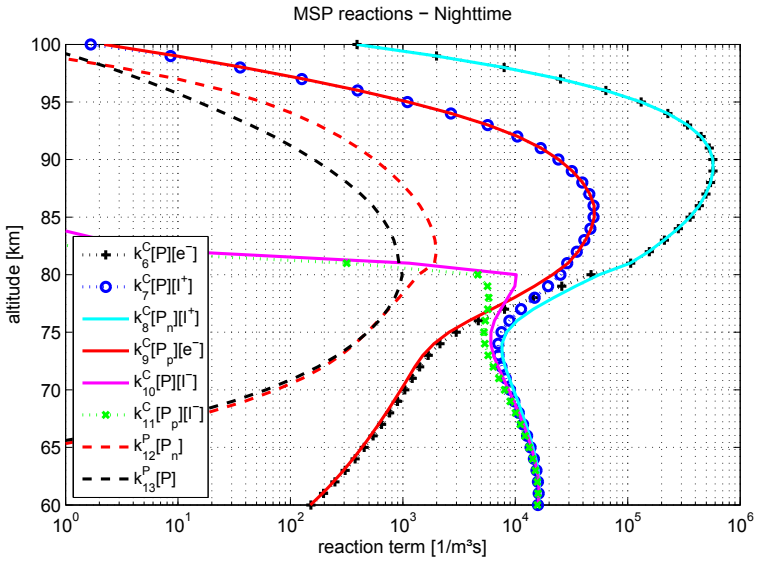

Figure 4.6: Height profiles of MSP photoreaction rates (dashed lines) and plasma capture rates by MSP (solid lines); compare legend entries with Equations 4.6–4.8. Reprinted from Baumann et al. (2013).

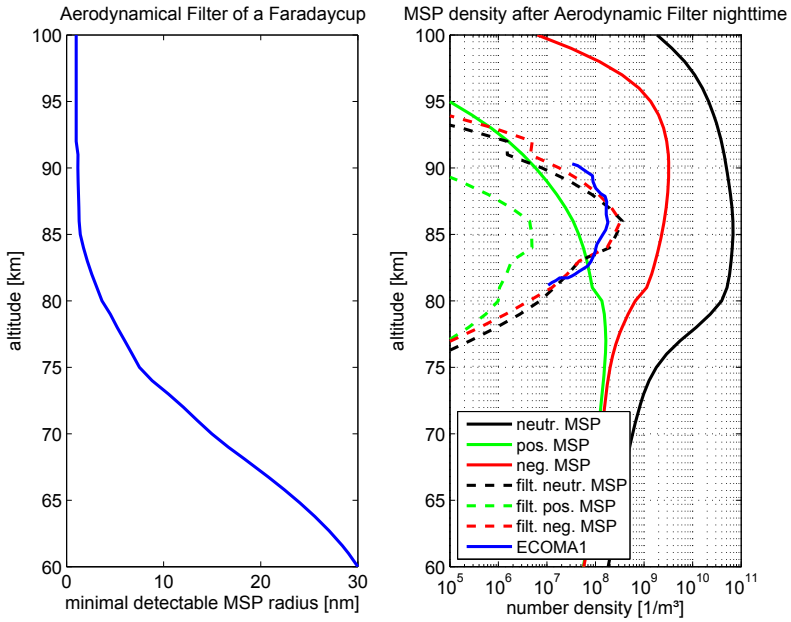

Figure 4.7: Left panel: aerodynamical filter that applies to Faraday cup measurements of MSP with a rocket trajectory typical for previous MSP measurements (Strelnikova et al., 2009) assuming a MSP mass density of $2\,\mathrm{g\,cm^{-3}}$, right panel: filtered neutral, positive and negative MSP densities (dashed lines) compared to the original MSP densities and ECOMA-1 data. Reprinted from Baumann et al. (2013).

Our model results also reveal that positively charged MSP can exist during the nighttime due to ion-capturing processes. Above 80 km the capture process of positive ions by neutral MSP is in balance with the capture of electrons by positively charged MSP. That leads to the substantial decrease of number densities of positively charged MSP in this altitude region (see Fig. 4.5) with peak number densities of $10^8\,\mathrm{m^{-3}}$ at ∼80 km. The photo reaction rates $k_{12}^{\mathrm{P}}[P_{\mathrm{n}}]$ and $k_{13}^{\mathrm{P}}[P]$ are not zero due to Ly-α from the geocorona, but compared to the capture rates they do not play a significant role.

Below 80 km the capture of negative ions by neutral and positively charged smoke is also possible. Between 75 and 80 km all capture processes of MSP lie within the same order of magnitude. Below 75 km the capture of electrons becomes insignificant and all rates for the capture of ions converge. This is the reason why the densities of negative and positive MSP are similar there, namely, that the equal densities of positive and negative ions and their similar mean ion masses in this region lead to similar capture rates by MSP (see Fig. 4.3 and Eqs. 3.1 and 3.3).

4.2.3 Comparison with experiments

In this section we compare our modelled MSP densities with the Faraday cup measurements on rockets. A direct comparison is not reasonable, since in-situ measurements with Faraday

cups tend to give a biased representation of the MSP density abundant in the atmosphere. During rocket flights the ensemble of MSP that can enter a Faraday cup is different from the real MSP ensemble. Aerodynamical effects filter the MSP that can reach the Faraday cup's electrode and create a current at the electrometer. The shock front which evolves around the payload prevents small particles from entering the detector (e.g., Horanyi et al., 1999; Rapp et al., 2005). Hedin et al. (2007) have derived from Direct Simulation Monte Carlo calculations around the rocket payload a distinct MSP radius that can reach a Faraday cup electrode for different altitudes. It has to be noted, that this filter curve depends on the altitude-dependent rocket speed and the geometry of the particular detector. This method has been used also by Strelnikova et al. (2009) to compare with the Faraday cup measurements for the ECOMA-1 flight. This particular filter curve is shown in Fig. 4.7 (left panel) and is used in this study. Therefore we can only compare our analysis with the ECOMA-1 data and to a certain extent with the other ECOMA flights, but not with different experimental setups. Note however, that the MASS experiment is designed to avoid aerodynamical filtering which can be seen in Fig. 2.5 (green line), i.e., the measured MSP density does not have a sharp edge below ∼78 km and can be compared to the unfiltered modeled data.

This filter function has been applied to the MSP densities derived by our model. By doing so we can achieve results that are comparable to measured MSP charge number densities. These filtered MSP densities are shown in Fig. 4.7 (right panel) together with the Faraday cup data from the ECOMA-1 flight. Please note that neutral MSP cannot be measured by a Faraday cup, we only show filtered neutral MSP densities for comparison.

It is obvious that the density peak lies in the altitude region 80–95 km where Faraday cups also measure peak densities. While the unfiltered model data shows a clear excess of the neutral MSP particles compared to the charged fraction, the filtered data show similar number densities of negatively charged MSP and neutral MSP. This can be explained by the fact that the smaller MSP, which are aerodynamically prevented from entering the Faraday cup detector, are unlikely to be charged. Above 90 km the filtered negative MSP even outnumber the neutral MSP. That can be explained by the fact that a larger fraction of MSP with sizes above 1 nm are charged negatively rather than being neutral.

Below 78 km the filtered negative and positive MSP densities are equal. This may contribute to the frequent observations of a very sharp lower boundary of charged MSP layers as seen in Fig. 2.5, since Faraday cups measure integrally negative and positive MSP density which cancels out on the electrode. However, the main effect here is the steep increase of detectable MSP sizes as seen in Fig. 4.7.

By directly comparing the ECOMA-1 data with our filtered MSP density we find a good agreement in all altitudes. The measured profile fits moderately to the filtered modelled data; even the peaks of the modeled and measured maximal negative MSP density match at 87 km, although the model overestimates the negative MSP density when comparing it to the measured density at the peak altitude. In the altitudes above and below 87 km, the model seems to overestimate the measured number density of negatively charged smoke. However, in general it can be said that there is a reasonable qualitative agreement between the modeled negative MSP densities and the in-situ observations, especially for the

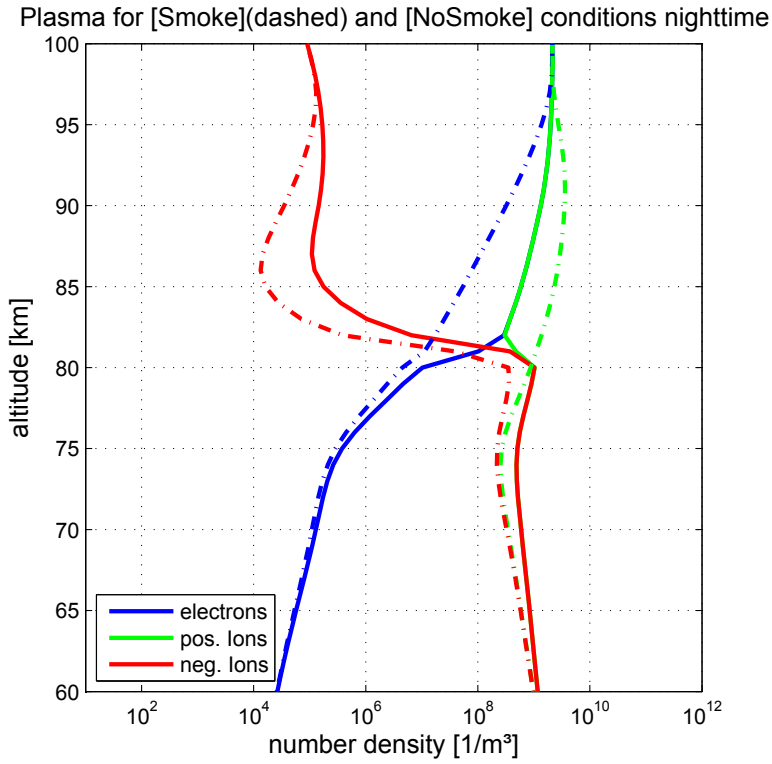

Figure 4.8: Height profiles of the plasma densities, for a model run with MSP (dashed lines) and without MSP (solid lines). Reprinted from Baumann et al. (2013).

ECOMA experiments.

4.3 Analysis of dominant plasma reactions

Now we concentrate on the influence of MSP on the plasma densities. To investigate this point, we performed another model run with identical initial condition, except that the MSP density has been set to zero. The reaction scheme of the model run without MSP is reduced, i.e., reactions concerning MSP are excluded. The remaining reactions are characterized by k_1^S-k_5^S. The comparison between the model run with and without MSP directly visualizes the influence of MSP on the D-region plasma and is shown in Fig. 4.8. The effect, suggested by Friedrich et al. (2012), that MSP act as an effective electron sink between 80 and 95 km is clearly reproduced by this simple ionospheric model. In addition, there are also unexpected differences in the ion densities between the model run with and without MSP. In the same altitude region where a significant electron density loss is observed, the MSP model results show a reduction of the negative ion density and an enhancement in the positive ion density. Below 80 km the situation changes somewhat. Here we find a reduction of all three plasma constituents due to the presence of MSP.

In the following, these changes in the charge balance (due to the presence of MSP) are

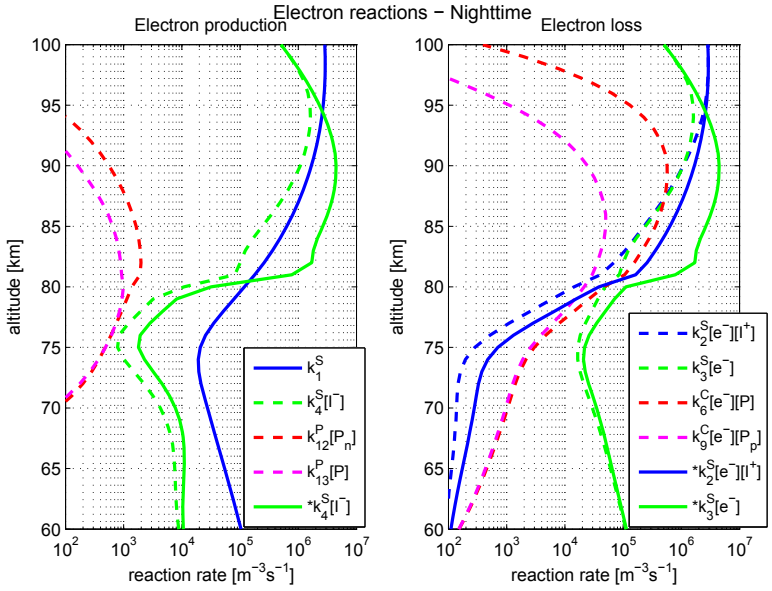

Figure 4.9: Altitude profiles of electron production and loss rates. Dashed lines show results of the model run with MSP, solid lines show results of the model run without MSP, see also Eq. 4.3. Reprinted from Baumann et al. (2013).

further analyzed by considering the production and loss processes in the rate equations for each plasma constituent. The reaction rates for electrons are shown in Fig. 4.9, for negative ions in Fig. 4.10, and for positive ions in Fig. 4.11. In all three figures we show the reaction rates of the model run with MSP (dashed lines) and without MSP (solid lines) together in one graph. Note that the reaction rates which represent the same processes in both model runs have the same color.

Figure 4.9 shows the modeled reaction rates for electron production and loss. Without MSP the main production processes of electrons are electron-ion pair production and the electron detachment from negative ions. This is balanced by electron attachment to neutrals and electron–positive ion dissociative recombination above 80 km. Below 80 km, the production is completely balanced by electron attachment to neutrals. Certainly the electron-ion pair production rate k_1^S, due to ionization, is independent of the presence of MSP. As stated above the MSP photo reactions are not very effective during the nighttime and therefore only few electrons are produced by these processes. The reduced electron density due to the presence of MSP accounts for the reduced negative ion density at the same time. Because of that, attachment of electrons to neutrals is reduced and at the same time the detachment process from negative ions is reduced. Below 80 km MSP do not have a significant influence on the electron processes anymore. The dominant electron sink in the altitude above 80 km is the electron capture by neutral MSP ($k_6^C[e^-][P]$), while the production of electrons is dominated by the ionization k_1^S. Without MSP presence, the dominant sinks and sources of electrons are the electron attachment to neutrals and the electron detachment from neutrals at altitudes below 80 km.

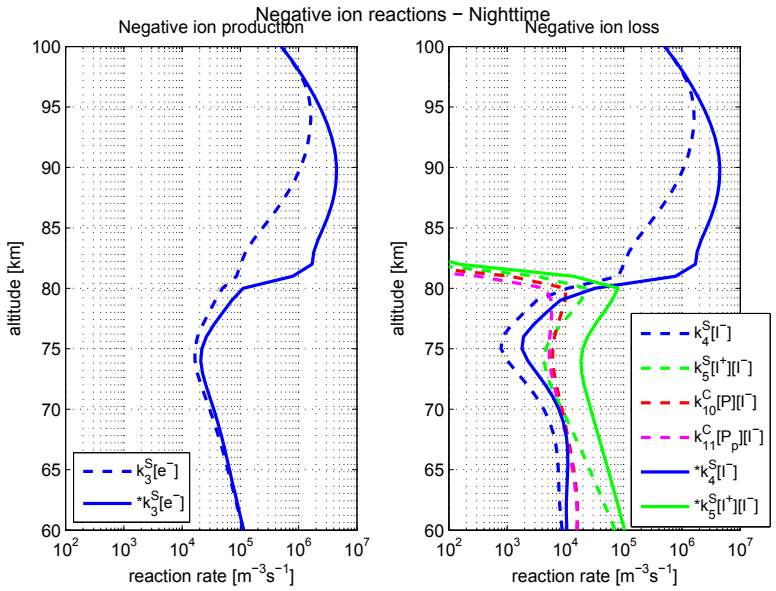

Figure 4.10: As in Fig. 4.9, but for processes involving negative ions, see also Eq. (4.5). Reprinted from Baumann et al. (2013).

The situation for negative ions is different although their existence is certainly coupled to the ambient electrons (see Fig. 4.10). There is a lack of negative ions above 80 km due to the reduced electron attachment. The density of negative ions is small compared to all other model components in that altitude region. Below 80 km the importance of negative ions grows and the presence of MSP leads to a decrease in negative ions there. While the production of negative ions are similar for both modeled cases, the loss processes are different. The capture of negative ions by MSP is more important than ion-ion recombination in that altitude region. The dominant sinks for negative ions are their capture by neutral and positively charged MSP ($k_{10}^{\mathrm{C}}[P][I^-]$, $k_{11}^{\mathrm{C}}[P_{\mathrm{p}}][I^-]$). In the case of MSP absence, ion-ion recombination dominates the reduction of negative ions.

In the end we discuss the influence of MSP on the positive ion density (see Fig. 4.11). The considerable increase of the positive ion density in the presence of MSP is an effect that has not been explicitly discussed for a MSP environment before. We note that ion enhancements have been discussed in Rapp and Lübken (2001) who, however, focussed on ice particle charging effects in the polar summer mesosphere. The model runs with and without MSP presence are easier to compare for the positive ion densities, since their production is given by the ionization rate k_1^{S}, which is not affected by MSP. Therefore we may concentrate on the loss processes only. There are two reactions that are related to the positive ion loss for both model runs. These are the dissociative recombination with electrons, which is important above 80 km, and the ion-ion recombination, which is significant below 80 km. It is obvious that both recombination processes are severely attenuated due to the presence of MSP. But the difference to the electrons and negative ions is that this attenuation leads to an increase of positive ions above 80 km and a reduction

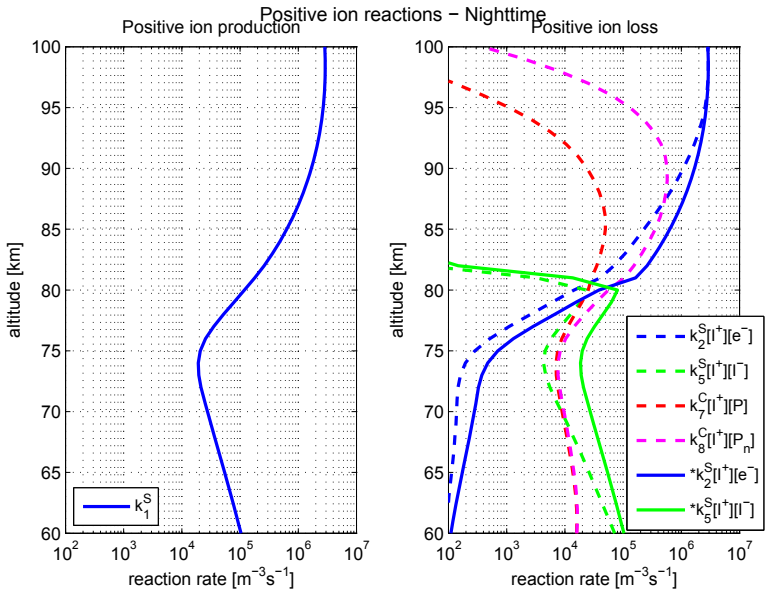

Figure 4.11: As in Fig. 4.9, but for processes involving positive ions, see also Eq. 4.4. Reprinted from Baumann et al. (2013).

below 80 km. The dissociative recombination with electrons is reduced due to the lack of electrons above 80 km, simultaneously the positive-ion capture of neutral MSP is important here. The reason for additional positive ions in the presence of MSP is the scavenging of electrons by MSP, which leads to the reduction of the dissociative recombination with electrons. This reduced recombination causes a gain of positive ions. Below 80 km we have the same situation as for the negative ions, i.e., additional loss processes due to positive-ion capture by MSP lead to a reduced density. In all, the dominant positive ion sinks are the positive-ion capture by positive MSP and neutral MSP (below 80 km only). Without the presence of MSP main sinks are the dissociative recombination with electrons (above 80 km) and the ion ion recombination (below 80 km).

4.4 Conclusions

We have investigated the influence of MSP on the charge balance in the D-region ionosphere. Both in-situ measurements and a one-dimensional ionospheric model were used to show a clear impact of MSP on the ionospheric composition of the D-region. As a major conclusion we may state that MSP are active charge carriers and are in fact important players in the charge balance of the D-region ionosphere.

The rocket-borne in-situ measurements of electron and positive ion density show a distinct difference from charge neutrality between 80 and 95 km. This difference can be explained by the ambient negatively charged MSP measured simultaneously with a Faraday cup. We addressed the influence of MSP on the D-region charge balance in a simplified ionospheric model with six components, i.e., electrons, positive and negative ions and neu-

tral and charged MSP. Plasma captured by MSP and photo reaction of MSP have been included in the reaction scheme, together with the standard ionospheric processes, e.g., ion-ion recombination etc. The model results point in the same direction as the experimental findings, namely that MSP play an important role in the charge balance of the D-region by capturing electrons and ions. By applying a filter function, which simulates the aerodynamical filtering of particles by the shock front around the Faraday cup, to the modelled MSP densities, we get particle densities in good general agreement with the experimental data, especially given the many uncertainties involved in both experiment and modelling. The model shows that the capture of plasma constituents by MSP is a dominant process. The model study also revealed that 80 km is a crucial boundary for the different capture processes. The electrons are captured very effectively by neutral MSP only above 80 km, while negative ions are captured by positive MSP and neutral MSP below 80 km. The capture of positive ions by MSP is an important process in the complete altitude range between 60 and 100 km and accounts for a fraction of positively charged MSP.

The model study revealed an increase of positive ions above 80 km in the presence of MSP. This increase has also been discussed by Rapp and Lübken (2001) in an environment of ice particles. So far we have not yet considered which influence MSP have on the composition of positive and negative ions (if any). By implementing MSP into the full ion-chemistry of the SIC model, we plan to identify such conceivable effects on the composition. In addition, future studies will also focus on MSP effects on the charge balance during daytime conditions. This will require close collaboration with lab experiments due to large uncertainties inherent in MSP-material dependencies on corresponding photoelectrical properties.

5 Meteor Smoke Impact on the Ion Chemistry

Aerosol particles of meteoric origin play an important role in the mesosphere and coinciding D-region ionosphere by influencing such diverse processes as the nucleation of mesospheric ice particles and the mesospheric water vapor distribution (e.g., Rapp and Thomas, 2006; Friedrich and Rapp, 2009, and references therein). Rosinski and Snow (1961) proposed the existence of meteoric vapor converted into particulate form within the mesosphere and stratosphere. Later modelling studies showed that these meteor smoke particles (MSPs) are formed in the mesopause region (Hunten et al., 1980) and are subject to atmospheric transport (Megner et al., 2008). These particles have been also studied by means of mass spectrometric in-situ measurements (Schulte and Arnold, 1992) and other rocket-borne techniques (e.g., Rapp et al., 2010), as well as by radar techniques (Strelnikova et al., 2007) and by satellite measurements (Hervig et al., 2009). There are also more recent studies which have identified the most probable composition of MSPs to be found in the group of metal oxides (FeO, MgO) and metal hydroxides (FeOH, MgOH) (Hervig et al., 2012; Rapp et al., 2012). An extensive review of meteoric metals in the mesosphere and the formation as well as composition of MSPs from a chemical point of view can be found in (Plane et al., 2015).

Insights into the composition of the D-region ionic components originates from rocket borne measurements with cryogenically pumped mass spectrometers (e.g., Narcisi and Bailey, 1965; Arnold and Krankowsky, 1971) and laboratory experiments provide the knowledge on ionization processes, ion reactions and electron-ion recombination (e.g., Mitra, 1981; Pavlov, 2014, and references therein). Combining both, ionospheric models helped to unfold the complex gas phase ion chemistry of the D-region (Turunen et al., 1996; Kazil et al., 2003; Winkler et al., 2009). However, these models do not yet consider the effects of MSPs in the ion chemistry.

This work concentrates on the influence of MSPs on the ion chemistry of the D-region ionosphere. Recent rocket-borne studies suggested that the D-region charge-balance is significantly influenced by MSPs (Friedrich et al., 2012). The observations suggest that MSPs act as a sink for D-region electrons leading to a depletion that can be reconciled by simplified ionospheric modelling (see Chap. 4 and Baumann et al., 2013; Plane et al., 2014; Asmus et al., 2015). In this manuscript, the influence of MSPs on the ion chemistry is studied in particular using the Sodankylä-Ion and Neutral Chemistry model (Verronen et al., 2005; Verronen, 2006).

Here, the diurnal variation of the charged MSP concentration and plasma concentration is studied for conditions at high latitudes. This chapter is structured as follows: Section 5.1

describes the SIC-model and the incorporation of MSPs and their interaction with the charged species. Section 5.2 covers the influence of MSPs on the D-region chemistry. Here, the diurnal variations of the D-region with the presence of MSPs is analysed and two case studies are performed. Within these two case studies, the behaviour of different positive and negative ion species in the presence of MSPs is investigated for dark and sunlit conditions in more detail. Section 5.2.3 covers a qualitative discussion of the uncertainties introduced by implementing MSP into the SIC model. MSPs have also an influence on minor neutral compontens of the atmosphere, which are discussed in Section 5.3. The conclusions of this study are drawn in Section 5.4.

Sections 5-5.2 have already been published within Baumann et al. (2015), only minor editorial changes have been applied here.

5.1 Model and Methods

5.1.1 SIC-Model

The present study uses the Sodankylä Ion and Neutral Chemistry (SIC) model which was originally only an ionospheric model (Turunen et al., 1996). We only show the basic principles of the current SIC model version here, a complete description is given elsewhere (Verronen et al., 2005; Verronen, 2006).

The SIC-model is a one-dimensional model with a coupled ion and neutral chemistry including vertical eddy transport of neutral species. Its chemical reaction scheme incorporates 43 positive ion species, 29 negative ion species and 32 neutral species. The model derives the concentrations of all individual ion components and 15 of the 32 neutral components. The rest of the neutral components are kept constant at defined concentrations. The NRLMSIS-00 model (Picone et al., 2002) is used to set the neutral background atmosphere at the modelled geographical location.

The SIC model includes all known ionization sources, i.e., galactic cosmic rays (GCR), solar irradiance and particle precipitation (electrons and protons). This study however, focusses on for undisturbed ionospheric conditions. Therefore, the ionization by electron precipitation and proton precipitation is turned off. Figure 5.1 shows the basic concept of the SIC model including input parameters, the external models mentioned above and the main SIC modules and how these are interconnected within SIC.

Since the GCR ionizes the neutral atmosphere only at lower altitudes, the photoionization is the major source of ionization at altitudes above 50 km. SIC derives the photoionisation rates for N_2, O_2, O, NO and $O_2(^1\Delta_g)$ leading to the primary ions N^+, $N_2{}^+$, O^+, $O_2{}^+$ and NO^+. The solar spectrum is taken from the Solar Irradiance Platform (SIP, former SOLAR2000 (Tobiska and Bouwer, 2006)).

The primary ions react with the neutral background atmosphere to form secondary ions, e.g., H_3O^+ cluster ions and NO^+ cluster ions. The free electrons produced by the photoionization can attach to neutral species and build negative ions, e.g., O_2^-, Cl^-. This is the case below 80 km, where the atomic oxygen concentration is low enough to not

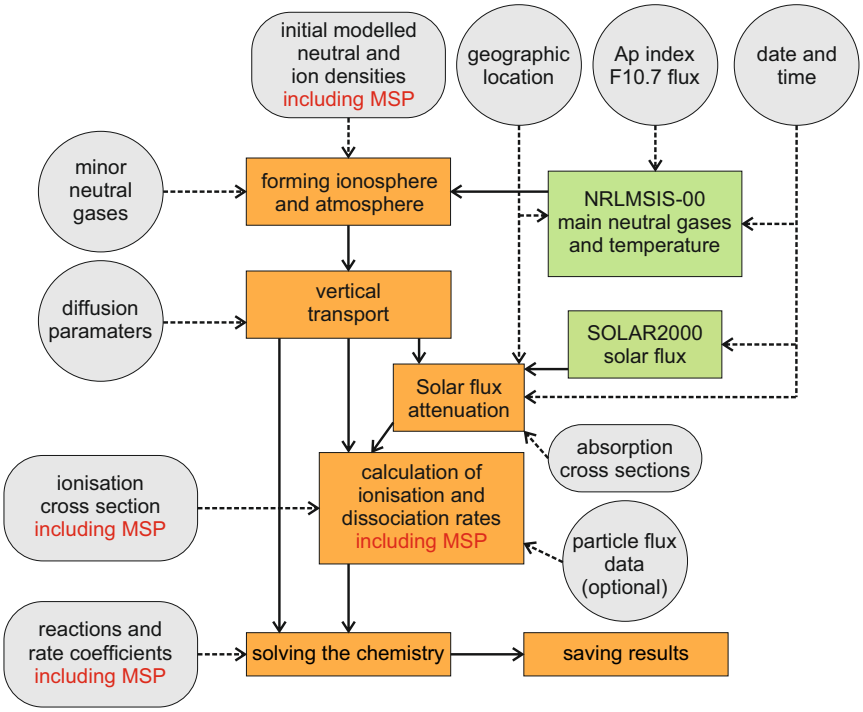

Figure 5.1: Schematic of the Sodankylä and Neutral Ion Chemistry model, with input parameters, external models and main SIC modules indicated by gray, green and orange boxes, changes due to implementation of MSP is shown in red. Data input visualized by dashed lines, internal data handling is shown by solid lines. Reprinted from Baumann et al. (2015) with permission of John Wiley and Sons.

significantly detach electrons from the negative ions.

In Fig. 5.2 the number concentrations of positive and negative ions are shown for nighttime and daytime conditions. The nighttime NO^+ profile is shifted upwards and has slightly lower number densities compared to the daytime. Since Lyman-α radiation scattered by the Earth's geocorona ionizes NO also during nighttime there is a remnant of NO^+. This also shifts the maximum ionization altitude of NO^+ upwards. In contrast, O_2^+ has a higher ionization energy than the photon energy of Lyman-α and nearly vanishes during nighttime by recombination with electrons. Reactions with these primary ions lead to the formation of cluster ions, e.g., $NO^+(H_2O)$ and $H^+(H_2O)_n$. Water cluster ions of the form $H^+(H_2O)_n$ are represented in the SIC model for up to n=8.

Also in the negative ion concentration there are changes from day to night, but they differ in detail from the behaviour of the positive ions. Mainly the composition of the negative ions changes from sunlit to unlit times, but these absolute number densities are similar at day and nighttime. This difference has two reasons. Firstly, there are no free electrons in the lower D-region during nighttime which leads to a loss of O_2^-, one of the primary negative ions. Secondly atomic oxygen also vanishes during night below 80 km due to the lack of sun light (not shown). That leads to an increase of CO_3^- because the loss processes, i.e., electron photo detachment and collisonal detachment with atomic oxygen,

are weakened. HCO_3^- is converted into Cl^- by subsequent reactions.

5.1.2 MSP as a new component

This section shows how MSPs have been implemented as an active component into the reaction scheme of the SIC model. Figure 5.1 indicates the modules and input parameters within the SIC model which have been adapted to achieve this implementation of MSPs. We have implemented four different processes involving MSPs into the SIC model. These are: plasma attachment to neutral MSPs, recombination of charged MSPs with plasma, detachment of electrons from negatively charged MSPs and photo ionization of neutral MSPs. Below, the derivation of the corresponding reaction rates is shown in detail.

In order to obtain size and height dependent information about the influence of MSPs on the D-region ion chemistry, we included the MSP size distribution for different altitudes from the model of Megner et al. (2006). The microphysical model of Megner et al. (2006) derives the concentrations of MSPs with sizes from 0.2 nm up to 40 nm for 30 to 100 km altitude. This microphysical model takes the meteoric mass input, the meteor ablation height, the vertical transport of MSPs by eddy transport and the coagulation of MSPs into account. The size distribution has about 30 size bins when using the original model configuration. For practical reasons and to keep the SIC model stable we have reduced this size distribution down to eleven size bins. Figure 5.3 shows this size distribution for an altitude of 90 and 60 km. At higher altitudes the number density of small particles is higher then the number of larger particles. That is because the MSPs are formed at ∼95 km. On their way down to lower altitudes the small particles sediment and coagulate to form bigger particles. Please note, that the width of the size bins increase exponentially, i.e., the first bin has a width of 0.12 nm while the eleventh bin has a width of 13 nm. These widths of the MSP size bins have been choosen due to the fact, that the coagulation kernel of the underlying microphysical model requires such size bin widths.

The size distribution used does not consider horizontal transport as indicated by the study of Megner et al. (2008). They made a transport experiment within their model scheme and identified the timescale of MSP transport from summer to winter pole induced by the meridional circulation to be in the order of 45 days. This horizontal transport is neglected in this study, since we only model the atmosphere for one single day. The time scale of meridional horizontal transport is thus much longer compared to the ionospheric processes which are subject of this study.

As a consequence of using eleven different MSP sizes the SIC model has been extended by 33 MSP components (neutral, singly charged positive and singly charged negative MSPs). Reaction rates for charging and recombination of the MSP components with each plasma components are derived for all eleven MSP sizes. The reactions and corresponding reaction rates of MSPs with the plasma components are discussed in detail in Baumann et al. (2013) and references therin. Nevertheless, we want to show the basic concepts of the involved processes and how they are included into the SIC-model.

For the interaction of electrons and the individual ions with MSPs we apply the aerosol charging formalism of Natanson (1960) which has been adapted for mesospheric aersolos

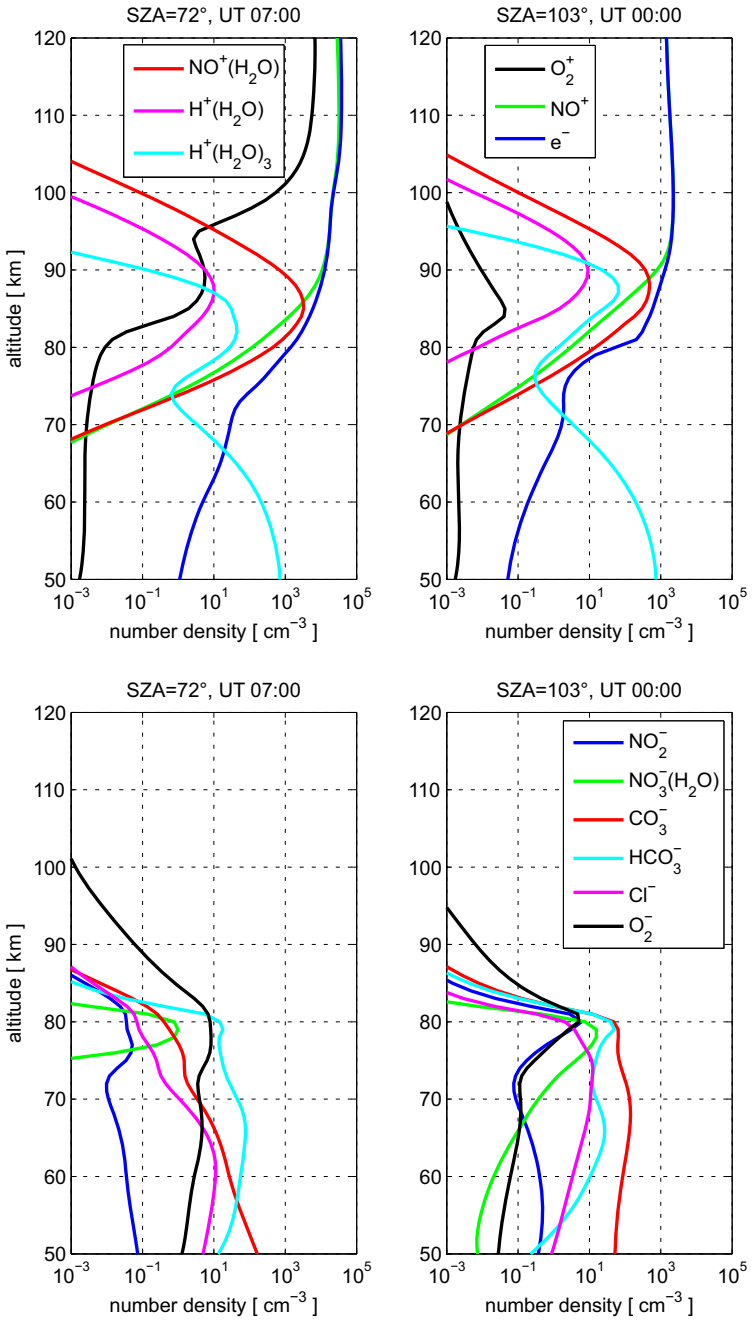

Figure 5.2: The number concentrations of the most abundant positive ions (top) and negative ions (bottom) for nighttime conditions (left panels) and daytime conditions (right panels), SIC model results from 8th September 2010 for the location of Andenes (69° N). Reprinted from Baumann et al. (2015) with permission of John Wiley and Sons.

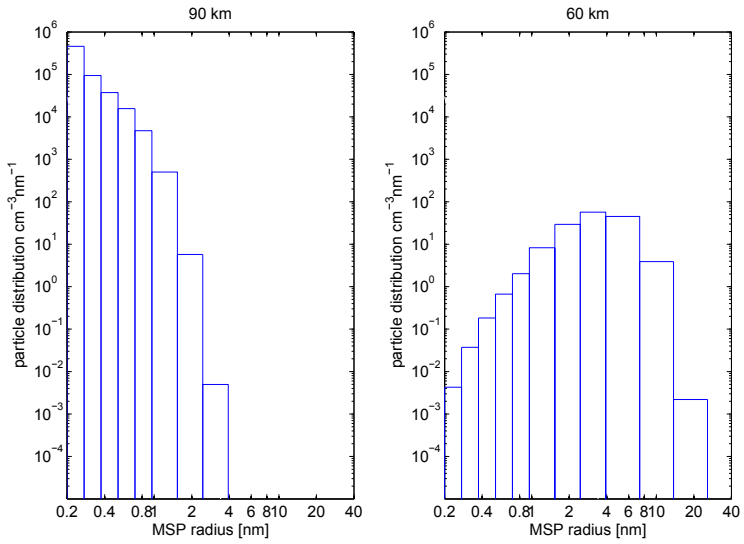

Figure 5.3: MSP size distribution for 90 km altitude (left) and 60 km altitude (right), from the micro physics model of Megner et al. (2006) which represents September conditions in the Arctic. Reprinted from Baumann et al. (2015) with permission of John Wiley and Sons.

by Rapp (2000). Section 3.1 takes a closer look on how $k_{charging}$ is derived. Here, Eq. 3.1 describes the attachment of ionspheric constituent to neutral MSP. This rate coefficient is a function of the mass of the attaching individual ionospheric species. For this study, $m_{e/i^+/i^-}$ is the mass of the positive (43 species), negative (29 species) ions and electron that can be captured by MSPs. Together with the eleven different MSP size components that leads to overall $(43+29+1)\cdot 11 = 803$ different reaction coefficients for the capture of plasma components. The attachment rate coefficient also depends on the temperature of electrons and ions wthin the D-region, which is given by the NRLMSISE-00 model (Picone et al., 2002).

In this study the maximum charged state of a MSP is restricted to one elementary charge. Higher charged states of MSPs are possible, but the charging reaction rates of already charged particles are orders of magnitude lower because the Coulomb forces block off plasma from reaching the equally charged MSPs. In addition, Rapp and Lübken (2001) showed that particles with radii below 10 nm cannot carry charges bigger then one elementary charge at all.

When charged MSPs exist, it is also possible that these charged MSPs collect an oppositely charged plasma component. That process leads to a recombination of the charge carriers. Also for this recombination process, the ion/electron is bound to the charged MSP and is therefore removed from the D-region. Equation 3.3 handles the recombination of charged MSPs with opositely charged plasma components within Sect. 3.1. The following recombination reactions can occur: electrons and negative ions can recombine with positively charged MSPs and positive ions can recombine with negatively charged MSPs. These combinations again lead to 803 different reaction rates which are derived at each

altitude.

Finally, we have also implemented photo reactions of MSPs, namely the photo ionization of neutral MSP and the photo detachment of electrons from negatively charged MSPs. This means, these processes are an additional source of free electrons. By assuming a MSP composition of hematite (Fe_2O_3), photoreaction rates are derived after Rapp (2009). A detailed derivation and how it is implemented within this study is shown in Sect. 3.2.

Photoionization and photodetachment reaction rates are derived for all eleven MSP sizes, leading to 22 MSP photo reactions. The solar flux data used for integration of equation (3.5) is given directly by the SIC model which uses the SOLAR2000 model data. The SIC model takes the attenuation of the solar flux within the atmosphere into account. For that, SIC derives the absorption of solar photons by the main components of the atmosphere and some minor species which are photoionized or photodissociated, i.e., O_2, N_2, O, Ar, He, NO, $O_2(^1\Delta_g)$, CO_2, O_3, NO_2, H_2O, H_2O_2, HNO_3, N_2O_5, and HNO_2. This derivation of the atmospheric attenuation results in the remaining solar flux corresponding to each modelled altitude bin (see Fig. 3.2).

All in all, 1628 reactions have been added to the SIC reaction scheme in order to implement eleven MSP size bins, which are derived for each modelled altitude bin. This already outnumbers the originally implemented reactions. The error introduced by the eleven bin size distribution is small since all relevant particle sizes ($< 10\,\text{nm}$) are well represented.

5.2 MSP influence on Ion Chemistry

To study the effects of MSPs on the D-region ion chemistry we have performed two SIC model runs. One model run has been set up including MSPs and the corresponding reactions as described in Section 5.1.2, i.e., the MSP-SIC run. The other SIC run uses the original reaction scheme and the MSP concentrations are set to zero, i.e., the Standard-SIC run . By doing that we can identify changes within the ion chemistry that are induced by the presence of MSPs. Both model runs represent quiet ionospheric conditions, i.e., with only solar radiation as ionization source, for high latitudes and September conditions. The correct functioning of the MSP-SIC model has been validated by comparing charge balance results with the simple ionospheric model of Baumann et al. (2013). In addition, we have performed MSP-SIC model runs with different time stepping (not shown) which show identical results.

We present model results of a complete day to study the diurnal variation of the charged MSP species and their influence on the ion species and the free electron concentration in the polar D-region ionosphere. After that two individual case studies are discussed in further detail. Here, the effects of MSPs on specific ion concentration and the associated chemical processes are analyzed in detail for night (SZA=103°) and day (SZA=72°).

5.2.1 Diurnal Variation

This section discusses the diurnal variations of negatively and positively charged meteoric smoke, as well as the relative differences between the MSP-SIC and Standard-SIC model runs of the electron density, of the sum of all positive ion concentrations and of the sum of all negative ion concentrations. Since the model has a time resolution of 5 min the terminator appears as steps in the MSP densities as well as in the relative differences of the plasma.

At first we want to discuss the negatively charged MSP concentrations. Figure 5.4 (a) shows a more or less contineous layer of negative MSPs between 80 and 100 km altitude. There are number densities of $\sim$1000 cm^{-3} during daytime that are reduced during dusk and dawn down to several 100 cm^{-3} and after that increases slightly again. Only during nighttime, when the sun is far enough below the horizon so that the D-region is not sunlit anymore, the negative MSP layer expands down to $\sim$55 km altitude. E.g., at 60 km altitude negative MSP number densities of 100 cm^{-3} exist. Electron attachment to neutral MSPs is very effective in the nighttime D-region (Baumann et al., 2013, and references therein).

The positively charged MSP abundance shows different characteristics as those of the negative one. There is a distinct layer of positive MSPs at lower altitudes, namely between 55 and 75 km (see Fig. 5.4 (b)). Number densities of up to several 100 cm^{-3} exist during daytime. Similar to the negative MSPs the positive MSP layer is slightly reduced during dusk and dawn. During nighttime the layer expands up to 90 km with number densities of about 100 cm^{-3}.

It has to be noted that the coexistence of negatively charged MSPs and positively charged MSPs at the same time in the same altitude during nighttime has been measured by rocketborne electro static deflection methods of Robertson et al. (2013). Also the dominance of positive MSPs at lower altitudes compared to the negative MSPs during daytime was shown in this study and hence supports our model results. However, the modeled ionospheric conditions do not match the exact conditions during the measurements.

Now, we want to consider the changes of the ions and electrons due to the presence of MSPs. Figure 5.4 (c), (d) and (e) show the relative difference between the MSP-SIC and the Standard-SIC model of electrons, positive ions and negative ions. Please note, that the difference of the sum of all positive and all negative ion model species between both model runs are shown here.

The electron difference shows a very strong diurnal variation. During sunlit times there is an 60 to 100 % enhancement of free electrons between 55 and 75 km, which coincides with the layer of positively charged MSPs at that time. The only possible explanation are MSP photoreactions, most likely photoionization, which is an additional source of free electrons. During dusk the electron enhancement nearly vanishes. At this time the optical path of solar photons within the atmosphere is greatly enhanced, which leads to the absorption (O_2, N_2) of photons with energies higher than 5 eV. Just after sunset in the D-region ($\sim$20:00 UT) the electron relative difference drops down to -80 %, indicating an effective electron attachment to neutral MSPs. This electron reduction expands to the altitude region between 70 and 95 km, which is not the complete layer thickness of negative MSPs

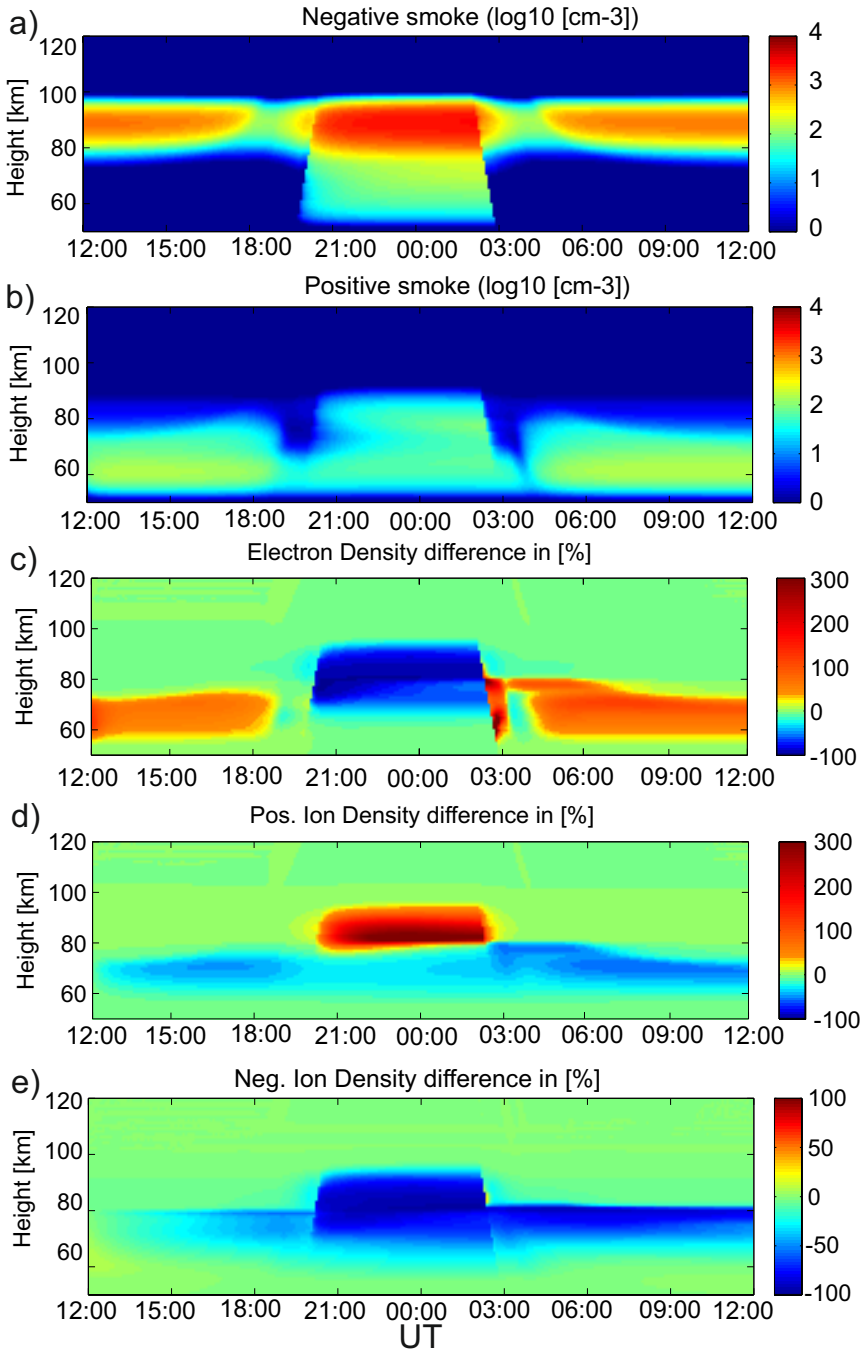

Figure 5.4: Diurnal Variation of the negative MSP (a) and positive MSP (b), also shown are the diurnal variations of the relative difference between a standard SIC-model run and the SIC run with MSP for the electrons (c), positive (d) and negative ions (e). Reprinted from Baumann et al. (2015) with permission of John Wiley and Sons.

during dark conditions. After sunrise ($\sim$ 3:00 UT) the electron reduction turns immediately into an enhancement of up to 300 %. This enhancement has its origin in the electron photodetachment from negative MSPs. A similar effect of immediate photodetachment of electrons just after sunrise has been discussed for the negative ions by e.g., Kazil (2002). In both cases the argument of a too long optical path of solar photons during sunrise does not hold, since also photons with much lower energy can detach electrons. These low energy photons, which are in the visible part of the solar spectrum, are hardly absorbed by the atmosphere and their solar flux is much higher than the UV photons with energies above 5 eV.

The influence of MSPs on the positive ion concentration is especially pronounced during nighttime. At this time there is an enhancement of positive ions for the MSP-SIC run compared to the Standard-SIC which reaches $\sim$300 %. This large enhacement can be explained by the reduced electron-ion recombination rate (Rapp and Lübken, 2001). This rate is greatly reduced due to the electron scavenging by the neutral MSPs. During daytime the positive ion density is marginally affected by MSPs. At altitudes 70$\pm$10 km the ion concentrations are reduced by 20 to 40 %, which is mainly due to the increased electron-ion recombination rate caused by the free electron enhancement here.

Negative ions are also effected by MSPs. Since negative ions only exist below $\sim$80 km (compare Fig. 5.2), effects shown as relative differences are only relevant below that altiude. Figure 5.4 (e) shows a $\sim$50 % reduction in negative ion density over the complete day. During daytime the reduction is located from 80 km down to 65 km. This reduction occurs despite the fact that the electron density is enhanced at lower altitudes during sunlit times. After sunset the loss of negative ions extend to higher altitudes. In practice there is no negative ion species of relevant number density, so that these relative changes have no physical meaning above 80 km. This reduction is related to the attachment of negative ion species to neutral and positively charged MSPs. Also the reduced abundance of free electrons during nighttime leads to lower production rates of negative ions.

In this section we only focus on the relative change in the sum of each positive and negative ions. The behavior of individual ions can differ significantly from the overall change of the sum of ions. Therefore, the next section discusses case studies to identify the chemical processes affected by the presence of MSPs.

5.2.2 Case studies of individual ions

This section examinates the influence of MSPs on groups of individual positive and negative ions for night (SZA=103°) and day (SZA=72°) conditions. The discussion of all individual ion components exceeds the scope of this article. Therefore, we choose ion species which show relevant changes, i.e., relative changes are bigger then 10 % and the absolute abundance of the species is higher than 1 cm^{-3} in the D-region. The ion species chosen also play an important role within the D-region ionosphere (Ferguson, 1979).

The positive ions considered here are: NO^+, $NO^+(H_2O)$, $H^+(H_2O)_n$. These ions are

connected by the following reactions:

$$NO + h\nu \longrightarrow NO^+ + e^- \quad \text{(R 5.1)}$$
$$NO^+ + H_2O + M \longrightarrow NO^+(H_2O) + M \quad \text{(R 5.2)}$$
$$NO^+(H_2O) + HO_x \longrightarrow H^+(H_2O) + NO_{x+1} \quad \text{(R 5.3)}$$

NO is ionized by sun light (R 5.1), then NO^+ can attach a water molecule (R 5.2). This water cluster can then react with a HO_x component to build positive water cluster ions (R 5.3).

These water cluster ions can grow by attaching additional water molecules in a tri-molecular reaction ((R 5.4)). There is also a collisional loss process which reduces the attached water molecules. The reaction rates of this reaction has been quantified by Lau et al. (1982).

$$H^+(H_2O)_n + H_2O + M \longrightarrow H^+(H_2O)_{n+1} + M \quad \text{(R 5.4)}$$
$$H^+(H_2O)_n + M \longrightarrow H^+(H_2O)_{n-1} + H_2O + M \quad \text{(R 5.5)}$$

The SIC model represents water clusters with ligand numbers of up to eight. In the interpretation of our results we will focus on water cluster ions with one, three and five ligands. Water cluster ions with higher ligand number do not exist at reasonable number densities.

The species O_2^-, Cl^-, $Cl^-(HCl)$ are considered for the negative ion species, which are connected via a reaction chain. The reaction rates can be found in Phelps (1969); Kazil (2002) and references therein.

$$O_2 + N_2 + e^- \longrightarrow O_2^- + N_2 \quad \text{(R 5.6)}$$
$$O_2^- + HCl \longrightarrow Cl^- + HO_2 \quad \text{(R 5.7)}$$
$$Cl^- + HCl + M \longrightarrow Cl^-(HCl) + M \quad \text{(R 5.8)}$$

O_2^- is a primary negative ion, which is build by a tri-molecular reaction with N_2 or O_2, i.e., neutral air. The Cl^- ion has many sources in addition to reaction (R 5.7). $Cl^-(HCl)$ is generated by the attachment of an additional HCl molecule to the Cl^- ion (R 5.8). The ion $Cl^-(HCl)$ is very long lived, since its only loss process ,except attachment/recombination with MSPs, is the detachment of HCl ligand in a reaction with O_2/N_2 (back reaction of (R 5.8)). This is also indicated by its high number density at lower altitudes. It has to be noted, that the negative ion chemistry is in general more entangled compared to the positive ion chemistry.

Night conditions

This section discusses the nighttime ion chemistry (SZA=103°, 00:00 UT). Figure 5.5 shows the charge balance (top), individual positive ion number density (middle) and negative ion number density (bottom). As seen in experimental data (Friedrich et al., 2012) and

model data (Baumann et al., 2013; Asmus et al., 2015) the charge balance is kept between 80 and 95 km by negative MSPs. This is represented in this study too. Here negative MSP densities equal the positive ion densities around absolute values of 3000 cm^{-3}. Below ∼80 km positive and negative MSPs tend to match up at number densities below 100 cm^{-3}.

When looking at the individual positive ions, one first notices that bigger ions exist at consequently lower altitudes. The highest number density of NO^+ occur at 95 km and above. In the MSP-SIC model run the number density shows a peak at 92 km at ∼2500 cm^{-3}. Also for the daughter ions of NO^+ the number densities are higher in the MSP model run compared to the Standard-SIC model run. This exceeds down to ∼80 km, where the excess of positive ions turns into a reduction of positive ions. Here the water cluster ions with ligand number higher than one are still abundant in reasonable number densities and can attach to neutral MSPs.

Negative ions exist only below 80 km, differences between the MSP-SIC run and the Standard-SIC model run are only visible here. The number densities of O_2^- and Cl^- are reduced down to 65 km, while the reduction of $CL^-(HCl)$ expands down to 55 km. O_2^- and Cl^- show a similar behaviour as the electron density , all of them drop in number density at lower altitudes. Only $Cl^-(HCl)$ is still abundant at number densities of several 100 cm^{-3}.

To give a quantification of the processes influenced by MSPs, Fig. 5.6 shows the relative differences between the MSP model run and the standard model run of all above discussed species in one panel. The electron density is strongly reduced in the MSP case, which is the main cause for the changes in negative and positive ion chemistry. In the first place, the electron scavenging reduces the electron-ion recombination as well as the production of negative ions by electron attachment to neutral species. Since the electron-ion recombination is reduced down to 80 km, additional positive ion can exist here. The enhancement is rather small for NO^+ with 50 %, which reacts fast with other neutral components to build secondary positive ions, but the enhancement of the positive ion density increases with ion size. The maximal enhancement for $NO^+(H_2O)$ and $H^+(H_2O)$ is 250 %, grows for $H^+(H_2O)_3$ to 2000 % and even raises to 7300 % for $H^+(H_2O)_5$. This successive growth of the water clusters is supported by the lacking electron-ion recombination, which is the main loss process for this group of ions. Only reaction (R 5.5) also reduces the growth of water cluster ions but is only of minor importance. Below 80 km, electron-ion recombination is not an important process in both model runs, i.e., the absolute density of free electrons is very low here. At these altitude only water cluster ions can still exist at reasonable number densities and are attached to neutral/negative MSPs resulting in their reduction of 30 %.

The change of negative ions is also strongly influenced by the nightly loss of electrons. The relative change of the primary ion O_2^- is nearly identical to the electron relative change. This is because the O_2^- production by electron attachment to O_2 is much faster than the O_2^- loss by O_2-attachment to MSP. This is no more the case for the relative changes of Cl^- and $Cl^-(HCl)$. Cl^- shows a higher reduction between 70 and 80 km and $Cl^-(HCl)$ reduction is higher in the complete altitude region compared to the relative change of the electron density. This additional reduction of both ion species has its origin in their attachment to MSPs. In addition the lack of free electron prevents the effective neutralization of positive MSP, which can exist at reasonable number densities. The recombination of positively

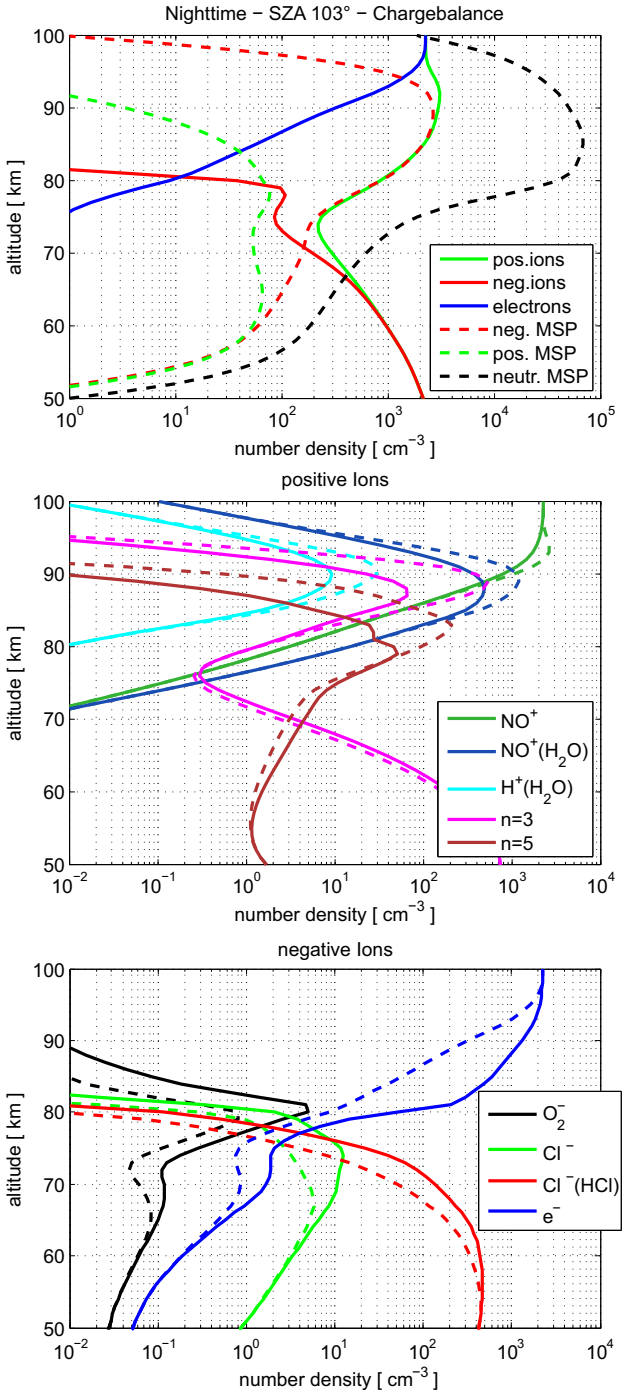

Figure 5.5: (Top) The D-region charge balance during 103° SZA with electron density and sum of all positive and negative ion concentration (solid) as well as sum of charged and neutral MSPs components shown (dashed) for the MSP-SIC model run, (Middle) relevant positive ion concentration for the Standard-SIC run (solid lines) and the MSP-SIC run (dashed lines), (Bottom) relevant negative ion density and electron density. Reprinted from Baumann et al. (2015) with permission of John Wiley and Sons.

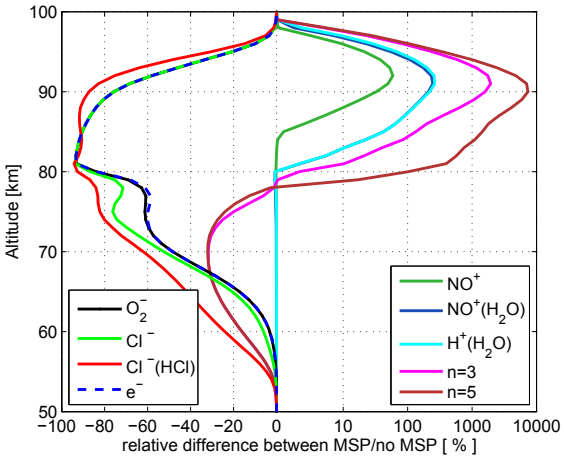

Figure 5.6: Relative difference of the ion and electron concentrations shown in Fig. 5.5 between the Standard-SIC run and the MSP-SIC run for an SZA of 103°, please note the logarithmic scale for the positive relative differences. Reprinted from Baumann et al. (2015) with permission of John Wiley and Sons.

charged MSP with negative ions is here an additional sink.

Day conditions

This section discusses the ion chemistry during daytime conditions (SZA=72°, 07:00 UT). Figure 5.7 shows the charge balance (top), individual positive ion number density (middle) and negative ion number density (bottom) for this time.

The charge balance during sunlit condition is only slightly influenced by the presence of MSPs. Due to the photodetachment of negative MSPs, which balances the electron attachment rate, negative MSP abundance is only 1000 cm^{-3} at 90 km despite the one order of magnitude higher electron density compared to the nighttime case. Because of the now effective photodetachment in sunlit conditions, the presence of MSPs does not lead to an effective scavenging of electrons anymore. The photodetachment is so effective, that below 75 km negative MSPs do not exist any longer. Moreover, shortwave solar radiation makes photoionization of MSPs possible, which leads to a number density of positively charged MSP in the order of 150 cm^{-3} at 60 km. As a result, there are localized layers of negative MSPs (90 km) and positive MSPs (60 km). To some extent this is even represented in the measurements of Robertson et al. (2013), despite the fact that the measurement were made under disturbed ionospheric conditions while the model represents quiet conditions only.

Since negative MSPs are only marginally involved in the charge balance , electron density does not change significantly above 80 km. Consequently, the positive ion chemistry does not change due to the presence of MSPs. Below 80 km, the water cluster ions with ligand number 3 and 5, which are still abundant there, exist at lower number densities. The electron density is enhanced in this height region, which can only be explained by

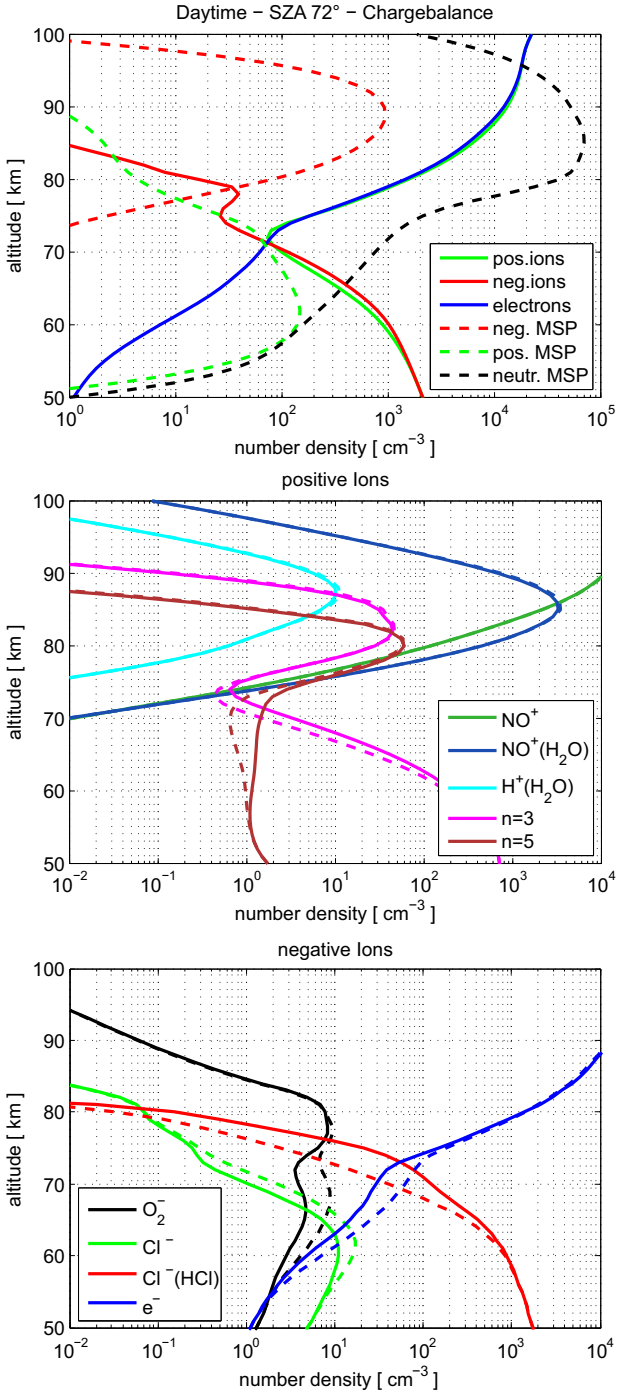

Figure 5.7: (Top) Charge balance of the MSP-SIC run, (Middle) positive ion and (Bottom) negative ion density as in Fig. 5.5 but for an SZA of 72°. Reprinted from Baumann et al. (2015) with permission of John Wiley and Sons.

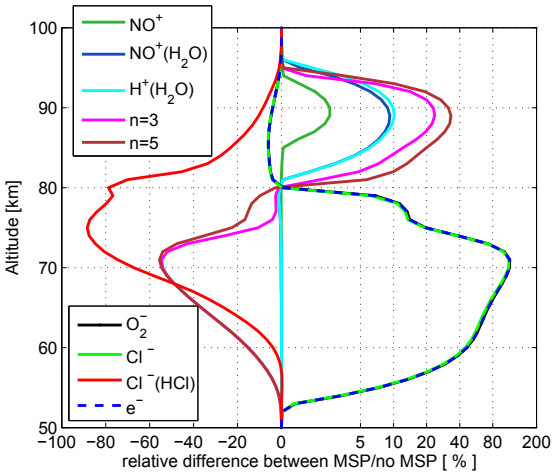

Figure 5.8: Relative difference of the individual ion and electron concentrations shown in Fig. 5.5 (b) and (c) between the Standard-SIC run and the MSP-SIC run for an SZA of 72°, please note the logarithmic scale for the positive relative differences. Reprinted from Baumann et al. (2015) with permission of John Wiley and Sons.

the photoionization of neutral MSPs. This higher abundance of free electrons leads to an increase of O_2^- production, which in turn also build more Cl^- ions. However, this enhancement does not pass over to the $Cl^-(HCl)$ concentration. On the contrary, $Cl^-(HCl)$ is similarly reduced as during nighttime.

Identically to the nighttime case study, Fig. 5.8 shows the relative differences between the MSP-SIC model run and the standard SIC model run for all above shown positive and negative ions for sunlit conditions. The electron density is reduced by 10 % at 90 km and enhanced by up to 120 % below 80 km. Both changes can be accounted to MSPs directly. The electron loss is due to electron attachment to neutral MSPs, the effect is rather small due to effective photodetachment. The enhancement occurs due to free electron production by photoionization of neutral MSPs.

The daytime behaviour of the electrons is as important as during the nighttime case. The minor reduction of electrons above 80 km increases the number densities of the positive ions in the same manner. The increase of NO^+ is below 5 %, but the abundance of $NO^+(H_2O)$ and $H^+(H_2O)_{1/3/5}$ rises consequently with number of water ligands and is ∼30 % for $H^+(H_2O)_5$. The same argumentation as in the nighttime case is also valid during daytime, i.e., reduced electron-ion recombination enhances the number densities of positive ions. Below 80 km the electron density is at higher levels increasing the electron ion recombination in this altitude region. As a consequence, the number density of water cluster ions reduces to 50 % of its original value, which means an additional reduction of 20 % compared to the nighttime case, where only ion attachment to neutral particles is important.

Negative ions are also affected by MSPs during daytime and the major driver of this change is the electron density, as it is for the positive ions. While O_2^- and Cl^- difference

directly follows the difference of electrons, the difference of $Cl^-(HCl)$ is completely decoupled from the electrons. The behaviour of $Cl^-(HCl)$ is only governed by the attachment to neutral and recombination positive MSPs since it is such a longlived ionic species. Both reaction rates are comparable to the only loss process of $Cl^-(HCl)$ (back reaction of (R 5.8)), because an excess of positive MSPs exists during daytime. The more short lived species O_2^- and Cl^- are completely coupled to the electron density which indicates that their attachment to MSPs is not significant here. It has to be noted, that there are also negative ion species that show a slightly different behavior. These species follow the electron governed behavior of O_2^- at higher altitudes and follow the MSP governed behavior of $Cl^-(HCl)$ at lower altitudes (not shown).

5.2.3 Discussion of Model Uncertainties

By implementing MSPs as an active component into the scheme of the SIC model we have introduced additional uncertainties into the model. These uncertainties originate from the microphysical and photoelectrical properties of MSPs which are not well known. The microphysical properties of MSPs are variables within the processes that link the D-region ionosphere to MSPs (shown in Sect. 5.1.2). This section covers a qualitative discussion of variable uncertainties and of their impact on the model results. Namely, the charging of MSPs and their photoelectric properties, the MSP number density and its size distribution itself as well as the influence of disturbed ionospheric conditions.

The charging of nanometersized MSPs by attachment of plasma was derived on the basis of classical electrodynamics (Natanson, 1960; Rapp, 2000), not taking into account quantum mechanical size effects. Plane et al. (2014) derived reaction rates from unimolecular kinetic theory for the electron attachment to a 0.25 nm MSP analogue and found a good agreement to the rates derived by the classical formalism which is used in this study. However, the exact nature of the size dependent charging efficiency $\gamma_{charging}$ is still unknown. As shown in an above section we have used a representation of this charging efficiency introduced by Megner and Gumbel (2009) who rely on laboratory measurements of water and carbon dioxide nanoparticles. This representation of $\gamma_{charging}$ avoids the charging of the smallest (0.2 nm) MSPs by attachment of plasma components. This is reasonable, since allowing all MSPs to be charged would remove all free electrons from the D-region which is not the case in reality. On the other hand, when increasing the charging treshold to larger MSP sizes reduces the influence of MSPs on the D-region as they become increasingly inactive.

Other important variables in our model study are the photoelectric properties of MSPs. We used the workfunction, electron affinity and complex refractive index of hematite (Fe_2O_3) to derive the photoionization and photodetachment rates. In the case of higher electron affinities and work function of the MSP material, the reaction rates would decrease because the integration of Equation (3.5) is carried out in a smaller wavelength band of the solar flux. Also the case of a more transparent material the ionization and photodetachment reaction would be reduced, because the corresponding crossections are smaller. Reduced photoreaction rates would result in a reduced number density of positively charged

particles. The less effective photodetachment of negatively charged particles would result in a growth of their abundance during daytime. The effects would change vice versa in case of a more opaque MSP material. Besides, Equation (3.5) represents a classical description of a quantum physical process. For an adequate representation of MSP photo processes laboratory measurements of photoelectrial properties of nanoparticles (MSP analogues) and an indepth quantum mechanical treatment of these processes are needed, but clearly beyond of this paper.

It also has to be noted that the magnitude of the effect shown here strongly depend on the number density of the MSPs. When decreasing the number of MSPs, the effects shown above should scale correspondingly. But when increasing the number of MSPs within the D-region there will be a distinct saturation effect, i.e., when all free electrons attach to the MSPs. Beyond sich large MSP number densities, a further increase of the MSP number density wouldn't lead to any additional change of the ionosphere.

In addition, this study represents the quiet ionosphere at auroral latitudes. In the presence of additional ionization due precepitation of energetic electrons and protons we expect that the number densities of positively and negatively charged MSPs would rise. Additional positive MSPs would be produced due to secondary electron emission induced by the precipitating electrons and protons. Also the number density of negatively charged MSPs would be enhanced due to the attachment of the additional free electrons during the elevated ionization period. This is because the MSP photo reactions are not affected by disturbed ionospheric conditions leading to a steady state at higher negative MSP number density.

For a more quantitative analysis of these uncertainties numerous sensitivity studies with the model are necessary. This is beyond the scope of this study and will be presented in a future study.

5.3 Indirect MSP influence on Minor Neutral Constituents

This section investigates how MSPs affect minor neutral components indirectly through their active role in the D-region ion chemistry. When treating the neutral components of the atmosphere, the SIC model divides them into two categories. The first category contains the major neutral constituents. These are molecular oxygen and nitrogen as well as argon, carbon dioxide, water vapor and some other species. The concentrations of the major neutral constituents are kept constant. These species are treated as reservoir gases within the SIC model, as they are highly abundant and their abundance does not change significantly due to ionospheric and atmospheric chemistry. The second group of components are the minor neutral constituents, e.g., ozone, reactive hydrogen (HOx) and reactive nitrogen (NOx) compounds. The SIC model treats these minor neutrals as interactive species, as production and loss mechanisms directly affect their number concentrations.

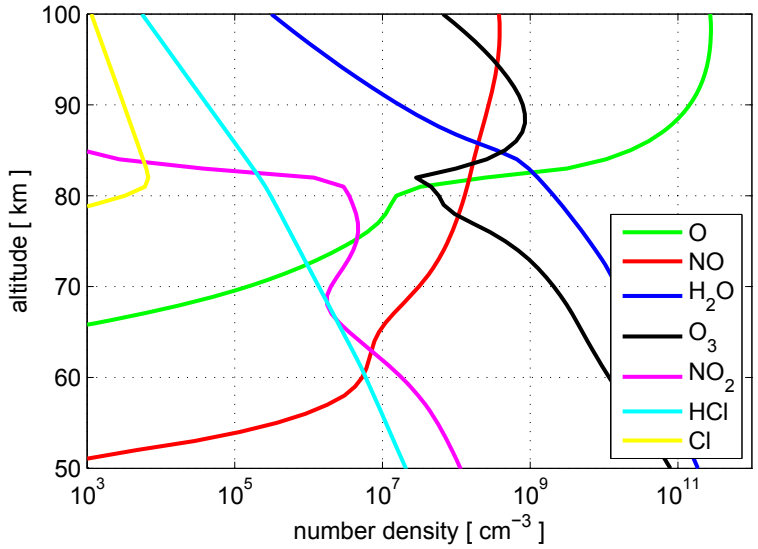

Figure 5.9: Number densities of minor neutral components within the SIC model for nighttime conditions: atomic oxygen, nitric oxide, ozone, nitrogen dioxide. The number densities of water vapor, hydrochloric acid and atomic chlorine are kept constant.

Figure 5.9 shows height profiles of minor neutral concentrations and water vapor. These components are related to the MSP-influenced neutral species through ion-neutral reactions. In the current SIC-model the wator vapor is treated as major constituent, i.e., the concentration is kept constant. Initial concentrations are derived from relating minor neutral mixing ratios to the absolute number density given by the NLRMSIS-00 model. The mixing ratios for the minor neutrals are taken from from Shimazaki (1971), while the water vapor mixing ratio has been adapted from Vardabas et al. (1998). The minor neutral constituents show a distinct day to night variation. For instance, photo chemical reactions are important for the formation of the hydroxyl (OH) radical.

In general, there are only two different ways how MSPs can act on the abundance of neutral components of the atmosphere. Firstly, the involvement of a neutral component within a ion-neutral reaction as a product or educt. This requires an educt ion whose abundance is reduced or enhanced due to the presence of MSPs (see Sect. 5.2). The educt ion species reacts with a certain neutral component to form a different ion and a different neutral component. Here, the educt neutral component or the product neutral component or both neutral components within the ion-neutral reaction can be affected by MSPs. Secondly, an already MSP-affected neutral component can alter a different neutral component within the standard neutral atmospheric chemistry (see Sander et al., 2003, and references therein).

When referring to changes or relative changes for a certain neutral component the same definition as in Sect. 5.2 is used. That is, the number concentrations of the MSP-SIC model run and the Standard-SIC run are compared to each other in order to identify changes in the atmospheric composition due to the presence of MSPs.

In addition, MSP induced changes within the neutral composition also follow a diurnal cycle similar as the ion composition. However, the changes in the neutral composition during daytime, dusk and dawn are in the order of 5 % percent and are therefore not considered here. Only during nighttime, when also the greatest changes in the ion chemistry occur (see Sect. 5.2.2), the neutral composition is changed significantly. Therefore, only nighttime conditions are investigated in more detail. Also the concentrations of the neutral constituents shown within Fig. 5.9 correspond to midnight local time.

The changes in minor neutral concentration can be directly induced by reactions including MSP-affected ions or via reactions with minor species that are effected from the presence of MSP. In contrast to Sect. 5.2, reaction rates are given here to better identify the relevant process. This is necessary, as the combination of the ion-neutral chemistry and neutral chemistry is very entangled.

The following describes the influences of MSPs on the concentration of HO_x compounds, nitrous acid, atomic and excited atmomic nitrogen and nitrogen trioxide.

5.3.1 Reactive hydrogen compounds

The left panel of Fig. 5.10 shows the concentration altitude profiles of atomic hydrogen (H), hydroxyl (OH) and hydroperoxyl (HO_2) for the MSP-SIC and standard-SIC model run. There is a slight reduction of the HO_x compounds in the MSP-SIC run within their local minimum between 55 and 65 km altitude. In the right panel of Fig. 5.10 the reduction between both model runs shows different values for the three HO_x compounds. While the relative reduction is smallest for OH with up to 10 %, it is already 15 % for HO_2 and nearly 20% for H. To find the reasons for this MSP-induced reduction of HO_x compounds, Fig. 5.10 also shows the concentrations and relative differences of the negative ions HCO_3^- and CO_3^- and the sum of all positive water cluster ions $H^+(H_2O)_n$.

These ion species have been chosen because they are closely related to the HO_x compounds in this altitude region. In addition, these ions have reasonably high number densities and are directly affected through MSPs in the same altitude region as the HO_x compounds. Figure 5.11 shows the transformation of one HO_x compound to another and how $H^+(H_2O)_n$, HCO_3^- and CO_3^- are connected. However, from Figs. 5.10 and 5.11 alone it is not possible to identify why the HO_x compounds exist at reduced concentrations in the MSP-SIC model run. The connection between these ions and the HO_x compounds is not clear from Figs. 5.10 and 5.11 alone.

To better identify the relevant reactions within Fig. 5.11, Tab. 5.1 lists the reaction rates derived by multiplying the concentration of the educts with the reaction rate coefficients. In case of a reaction like $A + B \xrightarrow{k} C + D$, the reaction rate reads k[A][B]. For the case of the HO_x compounds this has been done for 62 km altitude. Table 5.1 contains only the three rates for the formation of HO_x compounds from reactions involving ions and the three fastest transformation reactions of one HO_x-compound to another.

Two statements can be made from these reaction rates. Firstly, the production rate of HO_x compounds from reactions with ionic components is different for each of these

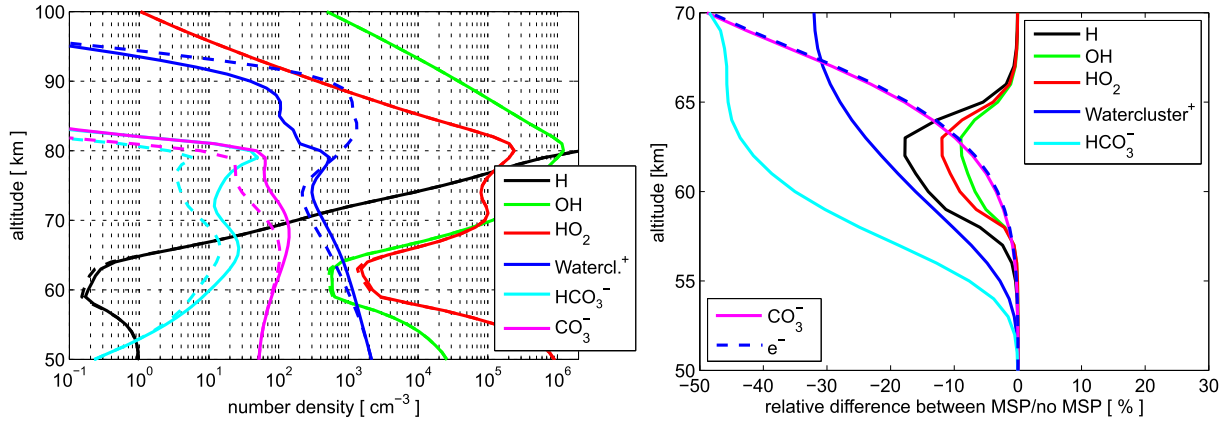

Figure 5.10: Left panel: number density height profiles of atomic hydrogen (H), hydroxyl (OH) and hydroperoxyl (OH_2), the sum positive watercluster ions (Watercl.$^+$), HCO_3^- and CO_3^- anions, dashed lines are MSP-SIC results, solid lines are Standard-SIC results. Right panel: relative differences of these species between the Standard-SIC and the MSP-SIC model run between 50 and 70 km altitude.

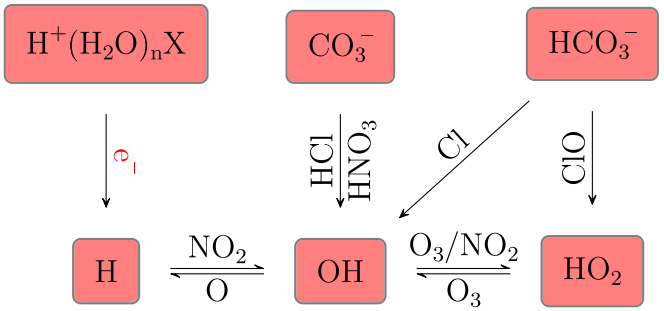

Figure 5.11: Detail of the reaction scheme of atmospheric radicals: atomic hydrogen (H), hydroxyl (OH) and hydroperoxyl OH_2. Components on the reaction arrows are the reaction partners. Only reactions are shown which include reaction partners with reasonable concentration at 60 km altitude, components in red boxes or red text indicate a reduced abundance due to active MSPs.

Table 5.1: Relevant reactions and their rates for production and loss of HO_x compounds including the production from ion-reactions at 62 km altitude.

Reaction	Rate [cm^{-3}s^{-1}]	Type
$H^+(H_2O)_nX + e^- \longrightarrow H + nH_2O + X$	$5 \cdot 10^{-4}$	H - Production
$CO_3^- + HCl \longrightarrow OH + Cl^- + CO_2$	$1.3 \cdot 10^{-2}$	OH - Production
$HCO_3^- + ClO \longrightarrow HO_2 + Cl^- + CO_2$	$2.4 \cdot 10^{-11}$	HO_2 Production
$H + NO_2 \longrightarrow OH + NO$	$2.1 \cdot 10^{-4}$	H-Loss, OH-Prod.
$OH + CO \longrightarrow H + CO_2$	$6.5 \cdot 10^{-2}$	OH-Loss, H-Prod.
$HO_2 + O_3 \longrightarrow OH + {}_2O_2$	$2.7 \cdot 10^{-2}$	HO_2-Loss, OH-Prod.
$OH + O_3 \longrightarrow HO_2 + O_2$	$2.0 \cdot 10^{-1}$	OH-Loss, HO_2-Prod.

reactive compounds. The production of OH from the reaction of CO_3^- with HCl occurs very often in this altitude region. The production of H from the recombination reaction of $H^+(H_2O)_n$ ions with electrons is two orders of magnitude slower, this is because of the small abundance of free electrons at 62 km during nighttime. The ionic production of HO_2 is not relevant at all. Secondly, when comparing the ionic production of HO_x compounds with their transformation reactions only the ionic production of OH is comparably fast to the OH production from the reaction of HO_2 with O_3. The ionic production of H and HO_2 is much slower compared to their production within the HO_x chemistry. The reactions of OH with CO and O_3 are the relevant production reactions for H and HO_2 respectively in this altitude region. Thus the lower abundance of OH manifests in a reduction of H and HO_2 via the HO_x chemistry.

In short, MSPs act on the OH concentration directly from the ion chemistry. The abundance of the CO_3^- ion is reduced and its reaction with HCl produces less OH between 55 and 65 km. The lower abundance of H and HO_2 in the MSP-SIC compared to the standard SIC run originates from this lower OH abundance and not directly from the ion chemistry.

HO_x compounds are important species in the ozone depletion, also within the mesosphere and lower thermosphere (e.g., Brasseur and Solomon, 2005, Pages 317-321). It can be expected that the reduced abundance of HO_x compounds in the MSP-SIC run also reduces the catalytic destruction of ozone. However, this cannot be observed in the model data, the ozone concentration does not change. The reason for that apparent contraction is that in this particular altitude and at midnight the concentrations of H, OH and HO_2 are too low in order to affect the abundance of ozone in a detectable way.

5.3.2 Nitrous acid

For nitrous acid (HNO_2) the situation is different compared to the HO_x compounds. In Fig. 5.12, the concentration of HNO_2 shows an increase between 80 and 90 km and a decrease between 60 and 70 km altitude in the MSP-SIC run compared to the standard SIC run. This is clearly visible in the relative differences of both model runs in the right panel, i.e., an increase of 120 % at 85 km and a decrease of 25 % at 65 km. Figure 5.12 also shows the species $NO^+(H_2O)_3$, NO_2^-, OH and NO_2 which react with HNO_2. OH is reduced around 65 km altitude which has been analyzed above. $NO^+(H_2O)_3$ is enhanced between 80 and 100 km, in the same altitude region as HNO_2 and a little bit above. The concentration of the NO_2^- ion is reduced over the whole altitude region. The abundance of NO_2 is not changed by the presence of MSPs, nevertheless it is also treated as a minor neutral within SIC.

Figure 5.13 shows the reaction scheme of HNO_2 with the other species of Fig. 5.12. This Figure has been divided into a 85 km part and a 65 km part, as the MSPs act differently on the abundance of HNO_2 in these altitudes. In the same manner as for the HO_x compounds, the rates for the reactions shown in Fig. 5.13 have been derived to better identify the origin of the different behavior of the HNO_2 species within the MSP-SIC model run. The analysis is first carried out for the 85 km HNO_2 enhancement (see rates in Tab. 5.2) and then for

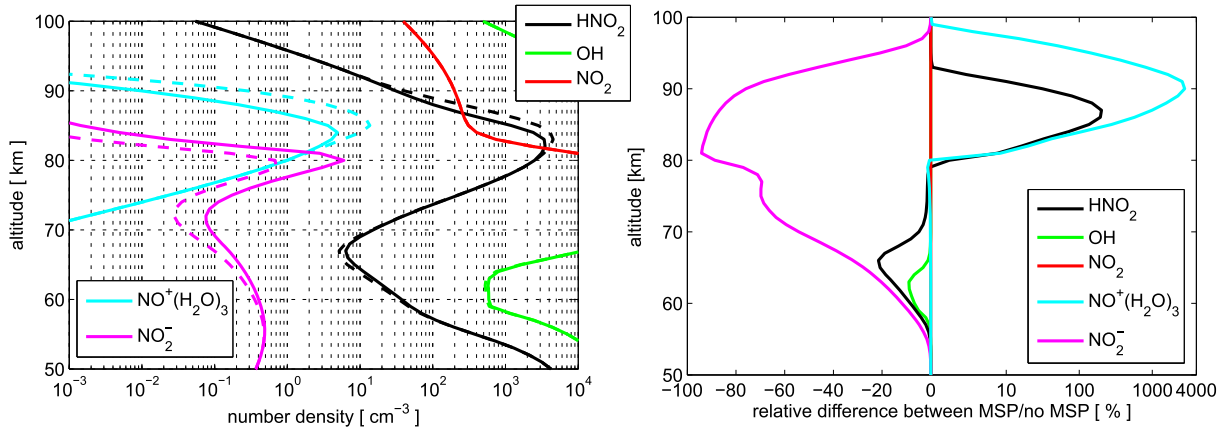

Figure 5.12: Left panel: number density height profiles of nitrous acid (HNO_2), hydroxyl (OH), nitrogen dioxide NO_2, the $NO^+(H_2O)_3$ cation and NO_2^- anion, dashed lines are MSP-SIC results, solid lines are Standard-SIC results. Right panel: relative differences of these species between the Standard-SIC and the MSP-SIC model run between 50 and 100 km altitude, notice the logarithmic scale of the positive values.

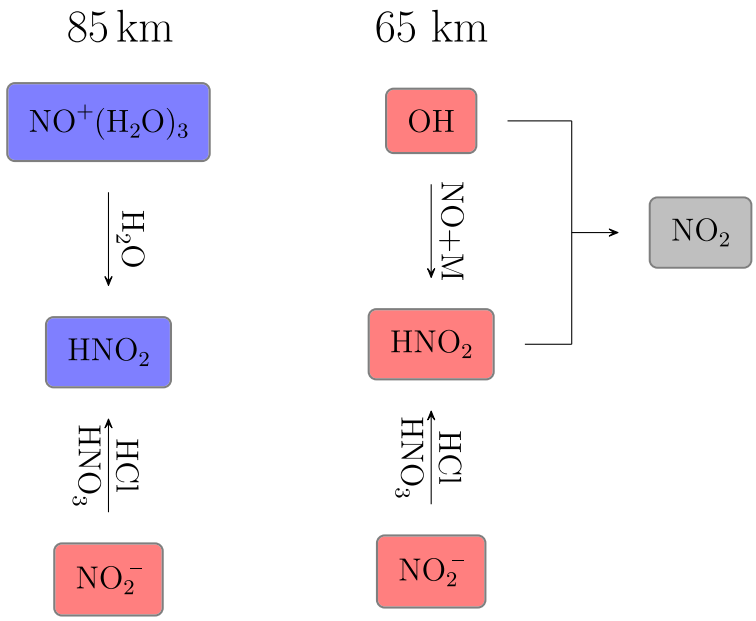

Figure 5.13: Reaction schemes for nitrous acid (HNO_2) at 65 and 85 km altitude. Only reactions are shown which include reaction partners with reasonable concentration at at these altitudes, components in red boxes indicate a reduced abundance due to active MSPs and respectively blue boxes indicate increased abundance.

Table 5.2: Relevant reactions and their rates for the production of HNO_2 at 85 km altitude.

Reaction	Rate [$cm^{-3}s^{-1}$]	Type
$NO^+(H_2O)_3 + H_2O \longrightarrow HNO_2 + H^+(H_2O)_3$	$5.7 \cdot 10^{-1}$	HNO_2-Prod.
$NO_2^- + HCl \longrightarrow HNO_2 + Cl^-$	$1.8 \cdot 10^{-8}$	HNO_2-Prod.
$NO_2^- + HNO_3 \longrightarrow HNO_2 + NO_3^-$	$5.9 \cdot 10^{-9}$	HNO_2-Prod.

Table 5.3: Relevant reactions and their rates for production and loss of HNO_2 at 65 km altitude.

Reaction	Rate [$cm^{-3}s^{-1}$]	Type
$NO_2^- + HCl \longrightarrow HNO_2 + Cl^-$	$5.6 \cdot 10^{-4}$	HNO_2-Prod.
$NO_2^- + HNO_3 \longrightarrow HNO_2 + NO_3^-$	$1.7 \cdot 10^{-6}$	HNO_2-Prod.
$OH + NO + M \longrightarrow HNO_2 + M$	$3.2 \cdot 10^{-5}$	HNO_2-Prod.
$OH + HNO_2 \longrightarrow NO_2 + H_2O$	$3.7 \cdot 10^{-8}$	HNO_2-Loss

the 65 km reduction (see rates in Tab. 5.3). In general, the only loss process of HNO_2 within SIC is its reaction with OH. As OH is not changing at 85 km, this reaction cannot be the reason for the higher abundance of HNO_2 here. This is not the case at 65 km where a reduction of OH coincides with the reduction of HNO_2.

The enhancement of HNO_2 at 85 km originates from the ionic reaction of $NO^+(H_2O)_3$ with water vapor, this is clear from Tab. 5.2. This positive ion is highly affected by the presence of MSP. Free electrons are bound to neutral MSPs and as a consequence electron-ion recombination is reduced and the concentration of $NO^+(H_2O)_3$ ions grows. The reactions involving NO_2^- cannot account for the greater abundance of HNO_2. Negative ions cannot exist at altitudes above 80 km and this is also the case for NO_2^-. In addition, its low abundance at 85 km is even lower than the abundance in the MSP-SIC run. The production of HNO_2 from the reaction of OH with NO and a joint component cannot account for the higher abundance of HNO_2 as OH and NO are not affected at 85 km.

For 65 km altitude the reaction rates concerning HNO_2 are shown in Tab 5.3. The fastest production rate for HNO_2 in this altitude is the ionic reaction of NO_2^- with HCl. This ion reacts also with HNO_3 but more than two orders of magnitude less frequent. The production of HNO_2 by the trimolecular reaction of OH with NO is much slower than the ion-neutral reaction. Therefore, one can state that the main reason for the reduction of HNO_2 in the altitude region around 65 km has its origin in the lower abundance of the NO_2^- ion. It is also visible from Tab. 5.3 that HNO_2 is not in an equilibrium state at 65 km during nighttime, as production and loss rates are not the same. This can occur under certain circumstances, as the SIC model derives the concentrations time dependent. In this case, the only loss process of HNO_2 is its reaction with OH. During nighttime OH is not produced via photodissociation and the remaining OH reacts with the highly abundant ozone more frequently (compare Tab. 5.1). Therefore the HNO_2 loss rate is rather small and cannot compete with the different production reactions at this time of day.

5.3.3 Atomic and excited atomic nitrogen

Atomic (N) and excited atomic nitrogen ($N(^2D)$) can only be found at higher altitudes, as these species are mainly produced by photoionisation and photodissociation of molecular nitrogen (N_2) from shortwave solar radiation. $N(^2D)$ and N are important radicals for nitric oxide in the altitude region above 80 km. Both species are involved in the production of NO by their reaction with O_2 but the ground state atomic oxygen can also destroy NO in a so called "cannibalistic reaction" (Brasseur and Solomon, 2005, Pages 351-355). When comparing the MSP-SIC to the Standard-SIC model run, MSPs decrease the concentrations of N and $N(^2D)$ between 80 to 95 km altitude (see Fig. 5.14). However, as nighttime conditions are analyzed, the abundance of both species is small. Especially the concentration of $N(^2D)$ is very low. During daytime the concentration of atomic nitrogen can reach $10^5\,cm^{-3}$ and excited atomic nitrogen reaches $1\,cm^{-3}$ at 90 km.

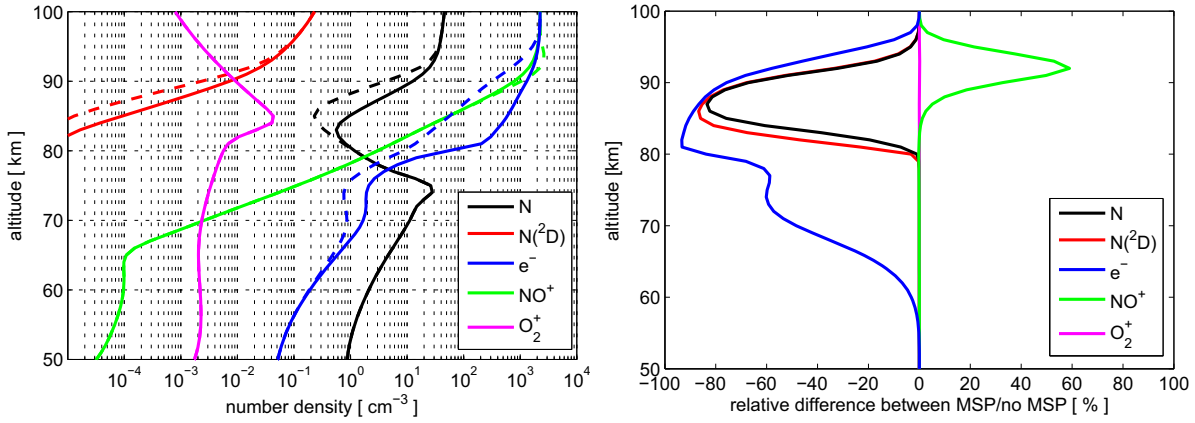

Figure 5.14: Left panel: number density height profiles of atomic nitrogen (N), excited atomic nitrogen $N(_2D)$, electrons (e^-), the NO^+ and O_2^+ ions, dashed lines are MSP-SIC results, solid lines are Standard-SIC results. Right panel: relative differences of these species between the Standard-SIC and the MSP-SIC model run between 50 and 100 km altitude.

The relative difference (right Panel of Fig. 5.14) between both model runs shows a reduction of 80 % for N and $N(^2D)$ in the MSP run. This substantial decrease is the motivation for a further analysis. Figure 5.15 shows the reaction scheme for N and $N(^2D)$ excluding photoreactions. From this scheme it is clear, that N^+ and N_2^+ ions do not play a role for the abundance reduction of N and $N(^2D)$. These ions nearly vanish at 90 km altitude during nighttime and they are not affected by MSPs. The higher abundant NO^+ ion seems to be the origin of the smaller abundance of N and $N(^2D)$. The reason has to be the electron ion recombination rate.

The reaction rates shown in Tab. 5.4 verify this assumption. Despite the higher abundance of NO^+ ions, the recombination of these ions with free electrons is reduced as the free electrons are scavenged by over 90 %. As a consequence, this reduced electron-ion recombination leads to the lower abundance of N and $N(^2D)$. Nevertheless, this electron ion recombination is still the fastest process in the Table. The other possible reaction rates

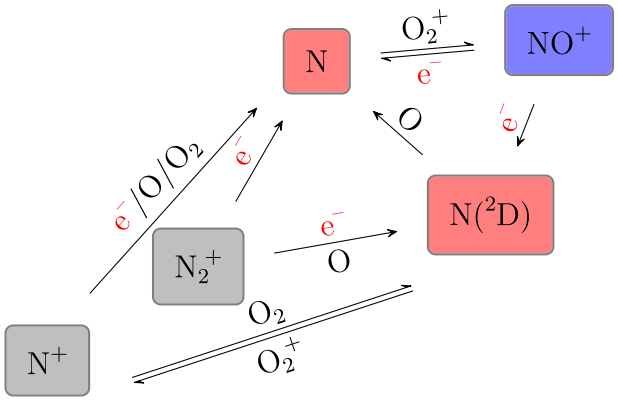

Figure 5.15: Reaction scheme for atomic nitrogen (N) and excited atomic nitrogen N($_2$D). Components in red boxes or red text indicate a reduced abundance due to active MSPs, respectively blue boxes indicate increased abundance and grey boxes indicate no abundance change.

for a lower abundance of N and N(^{2}D) are also shown in Tab. 5.4. The reactions of N with O_2^+ to form a NO^+ and the transformation of N(^{2}D) to N are both by far too slow to compete with the electron-NO^+ recombination.

Table 5.4: Relevant reactions and their rates for production and loss of N and N(^{2}D) at 91 km altitude.

Reaction	Rate [$cm^{-3}s^{-1}$]	Type
$NO^+ + e^- \longrightarrow N(^2D) + O$	$2.6 \cdot 10^{-1}$	N(^{2}D)-Prod.
$NO^+ + e^- \longrightarrow N + O$	$2.6 \cdot 10^{-1}$	N-Prod.
$N + O_2^+ \longrightarrow NO^+ + O$	$7.5 \cdot 10^{-12}$	N-Loss
$N(^2D) + O \longrightarrow N + O$	$9.4 \cdot 10^{-4}$	N(^{2}D)-Loss, N-Prod.

5.3.4 Nitrogen trioxide

Finally, nitrogen trioxide (NO_3) also belongs to the group of reactive nitrogen species (NO_y). From Fig. 5.16 it is also visible that NO_3 is affected by MSPs. Above 80 km, the concentration of NO_3 drops severely, but the abundance of NO_3 in the MSP-SIC run is greater than in the Standard-SIC run. The right panel of Fig. 5.16 shows a relative enhancement around 88 km altitude with a maximum value of around 30 %.

Figure 5.17 shows the reaction scheme of NO_3 including reaction partners which are MSP affected around 88 km altitude. The photoreactions cannot account for the higher abundance of NO_3, as nighttime conditions are considered. The numerous neutral reactions of NO_3 with various atmospheric constitutents form NO_2. These reaction cannot be the origin of the elevated abundance of NO_3, because the NO_2 species remains unchanged in the MSP-SIC run. In addition the ionic reaction of NO_2^- with ClO is also not the reason, since the negative ion is practically not existent at 88 km. Therefore it remains only the reaction of the $NO^+(H_2O)$ ion with OH_2, which is probably the source of the increased abundance of NO_3.

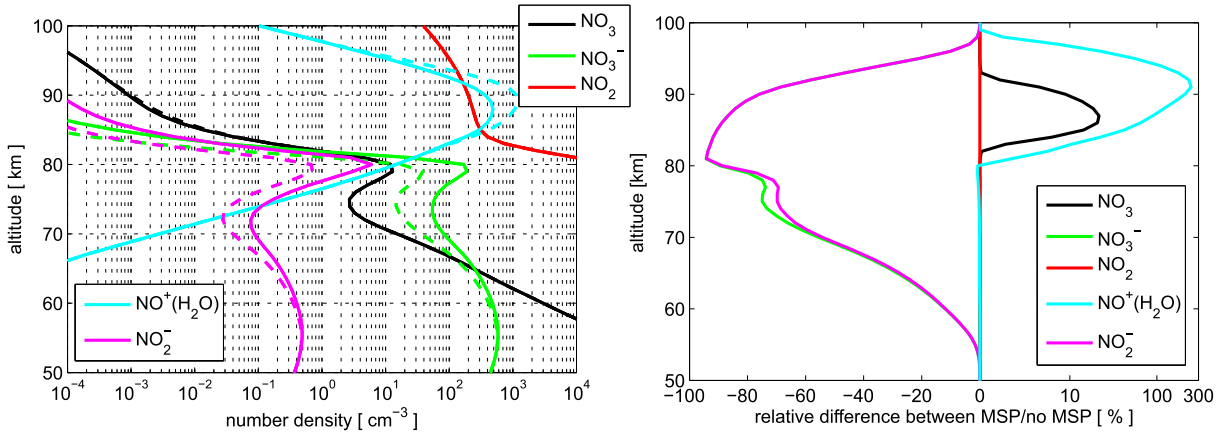

Figure 5.16: Left panel: number density height profiles of nitrogen trioxide (NO_3) and (NO_3) , the NO_3^- and NO_2^- negative ions and the $NO^+(H_2O)$ positive ion, dashed lines are MSP-SIC results, solid lines are Standard-SIC results. Right panel: relative differences of these species between the Standard-SIC and the MSP-SIC model run between 50 and 100 km altitude.

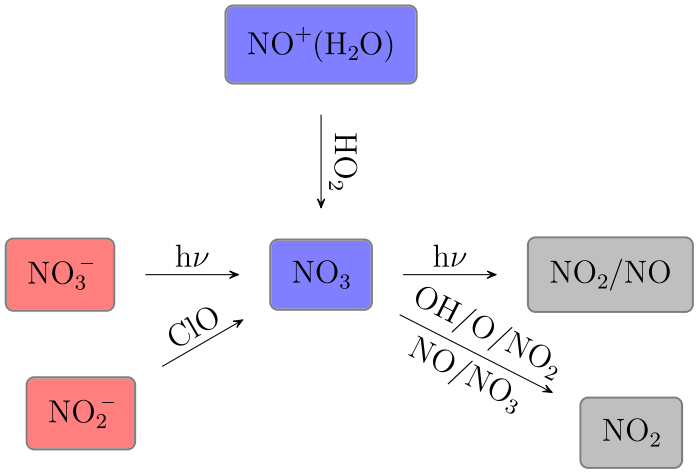

Figure 5.17: Reaction scheme for nitrogen trioxide (NO_3). Components in red boxes indicate a reduced abundance due to active MSPs, respectively blue boxes indicate increased abundance and grey boxes indicate no abundance change.

Table 5.5: Relevant reactions and their rates for production and loss of NO_3 at 88 km altitude.

Reaction	Rate [$cm^{-3}s^{-1}$]	Type
$NO^+(H_2O) + HO_2 \longrightarrow NO_3 + H^+(H_2O)$	$7.3 \cdot 10^{-4}$	NO_3-Prod.
$NO_2^- + ClO \longrightarrow NO_3 + Cl^-$	$6.9 \cdot 10^{-15}$	NO_3-Prod.
$NO_2 + O + M \longrightarrow NO_3 + M$	$1.6 \cdot 10^{-3}$	NO_3-Prod.
$NO_3 + O \longrightarrow NO_2 + O_2$	$2.5 \cdot 10^{-3}$	NO_3-Loss

For a better understanding of the underlying chemistry, Tab. 5.5 shows the derived rates of the reactions in Fig. 5.17. As expected above, the more abundant $NO^+(H_2O)$ in the MSP-SIC run leads to the enhancement of the NO_3 species via the reaction with HO_2. The trimloecular reaction of NO_2 with atomic oxygen (not shown in Fig. 5.17) is a by a factor of two faster production of NO_3 than this ionic reaction. However, this reaction cannot acount for the higher abundance of NO_3 in the MSP-SIC run, because the educts O and NO_2 are not affected by MSP. Furthermore, the production of NO_3 from the negative ion NO_2^- can be neglected at 88 km.

5.3.5 Summary

MSPs have an effect not only on the abundance of electrons and ions of the lower ionosphere but also on some neutral constituents of the mesosphere. This influence is induced via ion-neutral reactions within the D-region. There are also MSP influences on neutral species during daytime, but the induced changes are very small (some percent relative changes, or even below). The greatest influence can be seen during nighttime, when MSP also have the highest influences on the ion chemistry. Reactive hydrogen and reactive nitrogen are the main species which are affected by MSPs and have been analyzed in more detail.

Reactive hydrogen, i.e., HO_x compounds, are affected between 55 and 65 km and the abundance is reduced by 10 % for OH, 15 % for HO_2 and nearly 20 % for H. Here, OH is directly affected by ions and the HO_2 and H are indirectly affected via the HO_x chemistry. MSP affected reactive nitrogen, i.e., HNO_2, NO_3, and $N/N(_2D)$, shows disparate behaviour. These three species are not as reactivly connected with each other, as the HO_x compounds. That leads to the fact, that all three species are differently affected by MSP. In the case of HNO_2, the reaction of $NO^+(H_2O)_3$ with water vapor, leads to an enhancement of 120 % at 85 km. At 65 km altitude, the reaction of NO_2^- ions with HCl produce in the MSP-SIC run 25 % less HNO_2. The case of the 80 % reduced abundance of atomic nitrogen / excited atomic nitrogen at 90 km (Sect. 5.3.3) is different. Here, the reason is the reduced recombination of NO^+ with electrons. For NO_3, the results show an enhancement of 30 % around 88 km. The reason for that is the enhanced production due to the reaction of $NO^+(H_2O)$ with HO_2.

5.4 Conclusions

Aerosol particles from meteoric origin play an important role within the mesosphere and D-region ionosphere. This study has shown that MSPs not only have an impact on the charge balance but also alter the quiet D-region ion chemistry. This has been demonstrated by implementing MSPs as an active component into the reaction scheme of the SIC model. MSP size dependent plasma attachment reactions as well as photo detachment of negatively charged MSP and photoionization of neutral MSPs are the reactions which connect MSP to the standard ion chemistry.

It has been identified that the MSPs mainly affect the ion chemistry indirectly via the MSP induced changes of the electron density. During nighttime, electrons effectively attach to the neutral smoke between 80 and 100 km altitude, this process reduces the number of free electrons. Hence, electron - ion recombination occurs less frequently. As a consequence the abundance of positive ions grows, especially water cluster ions ($H^+(H_2O)_n$) can exist in a much higher abundance. This effect of mesospheric aerosols on the abundance of water cluster ions was previously discovered by Gumbel et al. (2003), albeit for mesospheric ice particles. We demonstrated in this study that also MSPs have an influence on the ion chemistry. This influence is not only limited to the cold summer mesopause, but also present during other seasons and altitudes. The increased abundance of heavy water cluster ions might also be important in the formation of nighttime Polar Mesospheric Winter Echoes (PMWE) at altitudes above 80 km (e.g., La Hoz and Havnes, 2008).

Primary negative ions (O_2^-) and many of the secondary negative ions (e.g., (Cl^-) behave similarly as the electron density, i.e., an overall reduction is observed between 60 to 90 km. On the contrary heavier ions, respectively ions which are formed after several ion-ion reactions, i.e., $Cl^-(HCl)$, are so long-lived, that attachment to MSPs is an important loss process. The attachment to neutral MSPs and the recombination with charged MSPs occurs especially at lower altitudes below 80 km. This is the case for both, negative as well as positive ions.

During daytime the D-region chemistry is also changed via the MSP influence on the electron density. In this case, electrons still attach to neutral MSPs but these electrons of the charged MSPs are easily photodetached by sunlight. As a consequence the positive ion chemistry is only sparsely influenced. At lower altitudes it can even occur that ionized MSPs can survive at reasonable number densities of hundreds per cubic centimeter. Hence, the electron density is enhanced here and causes an increase of short lived negative ions (O_2^-, (Cl^-)) and a reduction of positive water clusters due to enhanced electron-positive ion recombination. The behavior of the long-lived species $Cl^-(HCl)$ is different as it is similarly reduced during nighttime. This indicates again that the attachment to MSPs is an important loss process.

In addition to the analysis of the effect of MSPs on different ion species, also the influence of MSPs on neutral species has been analyzed. Severe changes in the neutral composition has been identified especially during nighttime. The affected species are the HOx compounds, nitrous acid (HNO_2), atomic and excited atmoc nitrogen and nitrogen trioxide. All of these species are defined as trace gase in the MLT region. A prerequisite for an MSP

influence on a neutral species is a relatively low concentration of these species. Only when this is the case the abundant ions and electrons, which are affected by MSPs, can act on the neutrals abundances. One single mechanism for all of the analyzed changes within the neutral components cannot be identified. For all four studied neutral components, a very specific reaction is responsible for the identified changes.

At this point it has to be noted that the composition and microphysical properties of MSPs are still not well known and demand further in-situ research as well as laboratory work. Both are important parameters within our model study and need to be quantified in order to enable better model comparisons with ionospheric measurements.

To achieve that goal, we propose Incoherent Scatter Radar (ISR) measurements of the D-region electron density during sunset and sunrise. Unfortunately, not all ISRs are capable of measuring the very low electron density in the D-region in the order of several $100\,\mathrm{cm}^{-3}$, which we expect at altitudes below 90 km. The above mentioned drop in electron density at a certain solar zenith angle is a signature for the existence of MSPs in the D-region and might be detactable only by the Arecibo ISR when observing on a regular basis. There has been an investigation by Anttila (2015) using EISCAT radar data to identify this electron density drop at high latitutdes. Unfortunately, this study was not able to identify this distinct diurnal variation in electron density at altitudes as low as 85 km. The reason for that is probably the limited sensitivity of the EISCAT radar which allow only the reliable measurement of electron densities as low as $10^2\,\mathrm{cm}^{-3}$. In addition, extra variability is induced into the high latitude D-region through energetic electron precipitation which is already visible in the different abundance of free electrons measured at Tromsø.

We already conducted model simulations for Arecibo conditions and the results are qualitatively similar to the here presented ones. We have also screened the MADRIGAL database (www.openmadrigal.org) for D-region electron-density measurements, which also contains the data of the Arecibo radar. Unluckily, the MADRIGAL database does not provide electron density measurements of the D-region in a quality that enables extensive D-region electron density comparisons with the SIC model considering MSP effects.We think that dedicated measurements of the electron density conducted during sunrise and sunset would make it possible to identify such an MSP effect and prove the existence of negatively charged MSPs. Especially the equatorial ionosphere with its sharper day to night transition would be a good subject of investigation to observe this effect.

These electron density measurements then has to be compared to dedicated SIC-modelled electron densities for the Arecibo site. Additional model restrictions, as the characterization of the background atmosphere by satellite measurements are necessary to make reliable statements on the conditions of the lower ionosphere with our model, i.e., nitric oxide,ozone profiles and temperature. This radar study would make it also possible to characterize the charging efficiency $\gamma_{charging}$ (see equation (3.2)) which is a crucial parameter within this study. This parameter is still not very well known but governs how severe the nighttime drop in electron density is.

6 Conclusions and Outlook

6.1 Conclusions

This thesis investigates the influence of meteoric smoke particles (MSPs) on the lower ionosphere. This topic has been approached by using different kinds of ionospheric models. The main motivation for this work has been the detection of charged mesospheric aerosols which have been identified to be meteor smoke particles. According to the hypothesis stated in Chap. 1, the charged MSPs have effects on the charge balance and ion chemistry of the D-region ionosphere. This hypothesis has been tested and the results of this work prove it right. The following paragraphs summarize these results and draw conclusions on the role of charged MSPs within the D-region.

As a first step, meteoric smoke particles have been included into a simplified ionospheric model that contains only six different species, namely free electrons, positive ions, negative ions and positively and negatively charged MSPs as well as neutral MSPs. These species undergo basic ionospheric reaction, e.g., photoionization and electron ion recombination, as well as MSP related reactions, e.g., electron/ion attachment to neutral MSP. This study is found in Chap. 4. By implementing MSPs into the reaction scheme of the Sodankylä Ion and Neutral Chemistry (SIC) model, the identification of the direct influence of MSPs on individual ion concentrations is possible. Chapter 5 includes an analysis of the diurnal variation of the abundance of charged MSPs, electrons and ions. In addition, this chapter includes an in-depth investigation of the behavior of individual ions due to the presence of MSPs during sunlit and dark conditions. Through ion-neutral reactions of ions, which are influenced by MSP, with neutral species, these species can also be affected by MSPs to some extent. Within Sec. 3.3 the possible effect of secondary electron emission from MSP is investigated. By applying a dusty plasma formalism from the astrophysics science community to MSPs within the D-region ionosphere it is possible to make reliable statements on the importance of this charging process for the charge state of MSPs.

Summing up, it can be stated that this work identified five findings regarding the explanation of the influence of meteoric smoke particles on the D-region. These are the following:

1. As many in-situ detections of charged MSPs have been carried out at high latitudes, it has been always the question if the charge state of the measured MSPs is to some extent changed by the energetic particle precipitation present at these geographic locations. The study of the secondary electron emission from MSPs in Sect. 3.3 revealed that this effect is indeed possible. However, the electron attachment to neutral MSPs and also photodetachment of electrons from negatively charged MSPs

are processes which are more than six orders of magnitude faster than the secondary electron emission from MSPs. Hence, this work confirms that the introduced error by not including this effect into ionospheric models is small and thus their results remain valid.

2. The model based investigation of the nightly D-region charge balance can reproduce the electron depletion and the coincident negatively charged MSP layer measured with rocketborne instruments at polar latitudes. The electron depletion reaches 80 % in the model run with included MSPs compared to the standard ionospheric model. In addition, after applying the aerodynamical filter of the in-situ Faraday cups to our modelled MSPs number densities it is even possible to reproduce Faraday cup measurements qualitatively.

3. The ion chemistry study revealed that MSPs have indeed an influence on the D-region. This influence has a different characteristic for each ion species during every time of the day. Main driver of this ion chemistry change is the big influence of MSPs on the abundance of free electrons. Especially during the nighttime the effect of electron scavenging by neutral MSPs is most important for the ion chemistry. This has two effects: above 80 km the lower abundance of electrons leads to a decrease in electron-ion recombination. As a consequence of the reduced loss mechanism, in particular positively charged water cluster ions can grow to a much bigger size and their number density increases by 200 % for small water clusters (e.g., one water molecule) up to more than 7000 % for big water clusters (e.g., five water molecules). Below 80 km, where also negative ions can exist, the lack of electrons leads to a reduced production of negative ions. In addition, direct attachment of ions to the surface of MSPs is only important in lower altitude regions. During daytime, the effective photodetachment of negative MSPs prevent the above mentioned scavenging of free electrons above 80 km. Below 80 km, the photo ionization of MSPs lead to an increase of free electrons. Therefore, shortlived ions as O_2^- can exist at higher concentrations but the abundance of long lived negative ions is reduced as their attachment to MSPs is effective sink.

4. In addition to the influence of MSPs on the ion chemistry, one can also identify an impact of MSPs on some minor components of the neutral atmosphere. These components are classified as trace gases. Main components as water vapor, oxygen and nitrogen abundance are not affected because of their large concentration compared to ion and MSP abundance. However, also the chemistry of the mesosphere is governed by the presence of reactive species like hydroxyl or nitric dioxide. The modelled difference of these reactive species is small compared to the MSP induced changes in the ion chemistry, e.g., the number densities of $H/OH/HO_2$ are reduced by 20/10/15 % due to the presence of MSPs.

5. The electron density is an ideal measure in order to quantify the influence of MSPs on the D-region. The modeling of the diurnal variation of the electron density re-

veals an abrupt day to night drop in electron density and a severe night to day increase. Quantifying this abrupt change of free electrons by means of Incoherent Scatter Radars (ISR) would reveal how severe the influence of MSPs on the D-region ionopshere is. An investigation of the electron density data from the EISCAT radar in Norway and their analysis, unfortunately, remain inconclusive. A distinct drop of the electron density from day to night and a significant increase during sunrise cannot be revealed by this radar. This is mainly caused by the insufficient sensitivity of the EISCAT radar and the presence of frequent ionospheric disturbances during energetic particle precipitation in northern Norway. However, this remains a worthwhile task when having access to more sensitive ISR radars.

In the following outlook, future work on the influence of MSPs on the D-region and phenomena in this altitude region which are significantly motivated by this thesis will be shortly introduced.

6.2 Outlook

Sensitive electron density measurements with Arecibo radar

In order to verify the effect of MSPs on the D-region electron density a successful proposal has been submitted to the National Astronomy and Ionosphere Center (NAIC) in Puerto Rico in order to acquire measurement time for the Arecibo radar. As described above not all ISR are capable of measuring the very low electron density of the D-region in the order of several $100\,cm^{-3}$, which we expect at altitudes below 90 km. The only ISR radar with sufficient sensitivity to cope with this low electron density is the Arecibo ISR. Arecibo is also unique for its location. Here, no particle precipitation is present to disturb the quiet time ionosphere and mask the MSP effect on the electron density.

The proposed measurements focuses on the verification of meteor smoke particle (MSP) induced effects on the D-region ionosphere using the Arecibo incoherent scatter radar. It is planned to conduct electron density measurement during sunset and sunrise. During that time of day, it is expected from results of this work, that there is a severe change in electron density. The electron density measurements then will be compared to specific SIC modelled electron densities for the Arecibo location. Additional model restrictions, as the characterization of the background atmosphere by satellite measurements are necessary to make reliable statements on the conditions of the lower ionosphere with the SIC model, e.g., nitric oxide, ozone profiles and temperature. This radar study enables the quantification of the electron scavenging by MSP and would make it possible to characterize the charging efficiency of MSPs. This parameter is still not very well known but governs how severe the nighttime drop in electron density is.

In-situ mass spectrometric measurements

Mass spectrometric investigations are essential to verify the influence of MSPs on the D-region ionosphere as shown in this work. For this goal, a rocketborne quadrupole ion mass spectrometer ROMARA (Rocket borne Mass spectrometer for Research in the Atmosphere) is under development at the DLR Institute of Atmospheric Physics. The instrument ROMARA is largely based on the earlier mass spectrometer of the working group of Prof. em. Frank Arnold from the Max Planck Institute for Nuclear Physics in Heidelberg (e.g., Arnold et al., 1977) and is supposed to be deployed in a rocket campaign in October 2017 that aims at explaining the PMWE radar phenomenon.

The ROMARA instrument is designed in a way that both positive and negative ions can be detected with masses of up to 2000 amu and with a height resolution of 2 km. This allows to infer the composition of the meteor dust particles within the D-region and illuminate their impact on the nature of PMWE radar echoes (compare Sect. 2.2.2).

Bibliography

Abbas, M. M., Tankosic, D., LeClair, A. C., and Spann, J. F. (2012). Charging of Dust Grains in Astrophysical Environments by Secondary Electron Emissions. *Astrophys. J.*, 756(1):41.

Amyx, K., Sternovsky, Z., Knappmiller, S., Robertson, S., Horanyi, M., and Gumbel, J. (2008). In-situ measurement of smoke particles in the wintertime polar mesophere between 80 and 85 km altitude. *J. Atmos. Sol.-Terr. Phys.*, 70:61–70.

Anderson, P. and Koons, H. (1996). Spacecraft charging anomaly on a low-altitude satellite in an aurora. *J. Spacecraft Rockets*, 33(5):734–738.

Anttila, M. (2015). The impact of meteor smoke particles on the D-region according to model simulations and experimental results. Bachelor Thesis.

Appleton, E. and Barnett, M. (1925). Local Reflection of Wireless Waves from the Upper Atmosphere. *Nature*, 115:333–334.

Arijs, E., Nevejans, D., and Ingels, J. (1987). Stratospheric positive ion composition measurements and acetonitrile detection: a consistent picture? *Int. J. Mass Spectrom.*, 81:15–31.

Arnold, F. and Krankowsky, D. (1971). Negative ions in the lower ionosphere: A Comparison of a model computation and a mass-spectrometric measurement. *J. Atmos. Terr. Phys.*, 33:1693–1702.

Arnold, F., Krankowsky, D., Marien, K. H., and Joos, W. (1977). A Mass Spectrometer Probe for Composition and Structure Analysis of the Middle Atmosphere Plasma and Neutral Gas. *J. Geophys.*, 44:125–138.

Asmus, H., Robertson, S., Dickson, S., Friedrich, M., and Megner, L. (2015). Charge balance for the mesosphere with meteoric dust particles. *J. Atmos. Sol.-Terr. Phys.*, 127:137 – 149. Layered Phenomena in the Mesopause Region.

Austin, L. and Starke, H. (1902). Ueber die Reflexion der Kathodenstrahlen und eine damit verbundene neue Erscheinung secundärer Emission. *Annalen der Physik*, 314(10):271–292.

Balcon, N., Payan, D., Belhaj, M., Tondu, T., and Inguimbert, V. (2012). Secondary electron emission on space materials: Evaluation of the total secondary electron yield from surface potential measurements. *IEEE T. Plasma Sci.*, 40(2):282–290.

Balsley, B. B., Ecklund, W. L., and Fritts, D. C. (1983). VHF Echoes from the High-Latitude Mesosphere and Lower Thermosphere: Observations and Interpretations. *J. Atmos. Sci.*, 40(10):2451–2466.

Bardeen, C. G., Toon, O. B., Jensen, E. J., Marsh, D. R., and Harvey, V. L. (2008). Numerical simulations of the three-dimensional distribution of meteoric dust in the mesosphere and upper stratosphere. *J. Geophys. Res.-Atmos.*, 113(D17):D17202.

Baumann, C., Rapp, M., Anttila, M., Kero, A., and Verronen, P. T. (2015). Effects of meteoric smoke particles on the D region ion chemistry. *J. Geophys. Res.-Space.*, 120(12):10,823–10,839.

Baumann, C., Rapp, M., and Kero, A. (2016). Secondary electron emission from meteoric smoke particles inside the polar ionosphere. *Ann. Geophys.*, 34(6):573–580.

Baumann, C., Rapp, M., Kero, A., and Enell, C.-F. (2013). Meteor smoke influences on the D-region charge balance: review of recent in situ measurements and one-dimensional model results. *Ann. Geophys.*, 31(11):2049–2062.

Benzenberg, J. and Brandes, H. (1800). Versuche die Entfernung, die Geschwindigkeit und die Bahnen der Sternschnuppen zu bestimmen. *Annalen der Physik*, 6:224–235.

Brasseur, G. P. and Solomon, S. (2005). *Aeronomy of the Middle Atmosphere*. Springer, third edition edition. ISBN 978-1-4020-3284-4.

Bruining, H. (1954). *Physics and Applications of Secondary Electron Emission*. Pergamon Press.

Burtscher, H., Scherrer, L., Siegmann, H. C., Schmid-Ott, A., and Federer, B. (1982). Probing aerosols by photoelectric charging. *J. Appl. Phys.*, 53(5):3787–3791.

Ceplecha, Z., Borovička, J., Elford, W. G., ReVelle, D. O., Hawkes, R. L., Porubčan, V., and Šimek, M. (1998). Meteor phenomena and bodies. *Space Sci. Rev.*, 84(3):327–471.

Chapman, S. (1931a). The absorption and dissociative or ionizing effect of monochromatic radiation in an atmosphere on a rotating earth. *Proc. Phys. Soc.*, 43(1):26.

Chapman, S. (1931b). The absorption and dissociative or ionizing effect of monochromatic radiation in an atmosphere on a rotating earth part II. Grazing incidence. *Proc. Phys. Soc.*, 43(5):483.

Chau, J. L., Strelnikova, I., Schult, C., Oppenheim, M. M., Kelley, M. C., Stober, G., and Singer, W. (2014). Nonspecular meteor trails from non-field-aligned irregularities: Can they be explained by presence of charged meteor dust? *Geophys. Res. Lett.*, 41(10):3336–3343.

Cheremisin, A. A., Shnipov, I. S., Horvath, H., and Rohatschek, H. (2011). The global picture of aerosol layers formation in the stratosphere and in the mesosphere under the influence of gravito-photophoretic and magneto-photophoretic forces. *J. Geophys. Res.-Atmos.*, 116(D19):n/a–n/a.

Cho, J. Y., Sulzer, M. P., and Kelley, M. C. (1998). Meteoric dust effects on D-region incoherent scatter radar spectra . *J. Atmos. Sol.-Terr. Phys.*, 60(3):349 – 357.

Chow, V. W., Mendis, D. A., and Rosenberg, M. (1993). Role of grain size and particle velocity distribution in secondary electron emission in space plasmas. *J. Geophys. Res.-Space.*, 98(A11):19065–19076.

Cziczo, D. J., Thomson, D. S., and Murphy, D. M. (2001). Ablation, Flux, and Atmospheric Implications of Meteors Inferred from Stratospheric Aerosol. *Science*, 291(5509):1772–1775.

Dawkins, E. C. M., Plane, J. M. C., Chipperfield, M. P., and Feng, W. (2015). The near-global mesospheric potassium layer: Observations and modeling. *J. Geophys. Res.-Atmos.*, 120(15):7975–7987.

Dhomse, S. S., Saunders, R. W., Tian, W., Chipperfield, M. P., and Plane, J. M. C. (2013). Plutonium-238 observations as a test of modeled transport and surface deposition of meteoric smoke particles. *Geophys. Res. Lett.*, 40(16):4454–4458.

Eidhammer, T. and Havnes, O. (2001). Size dependence of the mesospheric dust temperature and its influence on the noctilucent clouds and polar mesosphere summer echo phenomena. *J. Geophys. Res.*, 106:24831–24841.

Enell, C.-F., Hedin, J., Stegman, J., Witt, G., Friedrich, M., Singer, W., Baumgarten, G., Kaifler, B., Hoppe, U.-P., Gustavsson, B., Brändström, U., Khaplanov, M., Kero, A., Ulich, T., and Turunen, E. (2011). The Hotel Payload 2 campaign: Overview of NO, O and electron density measurements in the upper mesosphere and lower thermosphere. *J. Atmos. Sol.-Terr. Phys.*, 73:2228–2236.

Fang, X., Randall, C. E., Lummerzheim, D., Wang, W., Lu, G., Solomon, S. C., and Frahm, R. A. (2010). Parameterization of monoenergetic electron impact ionization. *Geophys. Res. Lett.*, 37(22):L22106.

Fehsenfeld, F. C., Ferguson, E. E., and Schmeltekopf, A. L. (1966). Thermal-Energy Associative-Detachment Reactions of Negative Ions. *J. Chem. Phys.*, 45:1844.

Feng, W., Marsh, D. R., Chipperfield, M. P., Janches, D., Höffner, J., Yi, F., and Plane, J. M. C. (2013). A global atmospheric model of meteoric iron. *J. Geophys. Res.-Atmos.*, 118(16):9456–9474.

Fentzke, J. T., Hsu, V., Brum, C. G. M., Strelnikova, I., Rapp, M., and Nicolls, M. (2012). D region meteoric smoke and neutral temperature retrieval using the poker flat incoherent scatter radar. *Geophys. Res. Lett.*, 39(21):L21102.

Fentzke, J. T. and Janches, D. (2008). A semi-empirical model of the contribution from sporadic meteoroid sources on the meteor input function in the MLT observed at Arecibo. *J. Geophys. Res.-Space.*, 113(A3):A03304.

Fentzke, J. T., Janches, D., Strelnikova, I., and Rapp, M. (2009). Meteoric smoke particle properties derived using dual-beam Arecibo UHF observation of D-region spectra during different seasons. *J. Atmos. Sol.-Terr. Phys.*, 71:1982–1991.

Ferguson, E. E. (1979). Ion-Molecule Reactions in the Atmosphere. In Ausloos, P., editor, *Kinetics of Ion-Molecule Reactions*, volume 40 of *NATO Advanced Study Institutes Series*, pages 377–403. Springer US.

Fowler, R. H. and Nordheim, L. (1928). Electron Emission in Intense Electric Fields. *Proc. R. Soc. Lond. A, Math. Phys. Sci.*, 119:173–181.

Frahm, R. A., Winningham, J. D., Sharber, J. R., Link, R., Crowley, G., Gaines, E. E., Chenette, D. L., Anderson, B. J., and Potemra, T. A. (1997). The diffuse aurora: A significant source of ionization in the middle atmosphere. *J. Geophys. Res.-Atmos.*, 102(D23):28203–28214.

Friedrich, M. and Rapp, M. (2009). News from the Lower Ionosphere: A Review of Recent Developments. *Surv. Geophys.*, 30:525–559.

Friedrich, M., Rapp, M., Blix, T., Hoppe, U.-P., Torkar, K., Robertson, S., Dickson, S., and Lynch, K. (2012). Electron loss and meteoric dust in the mesophere. *Ann. Geophys.*, 30:1495–1501.

Friedrich, M., Torkar, K. M., Hoppe, U.-P., Bekkeng, T.-A., Barjatya, A., and Rapp, M. (2013). Multi-instrument comparisons of D-region plasma measurements. *Ann. Geophys.*, 31(1):135–144.

Fuchs, N. (1963). On the stationary charge distribution on aerosol particles in a bipolar ionic atmosphere. *Geofisica pura e applicata*, 56(1):185–193.

Gabrielli, P., Barbante, C., Plane, J. M. C., Varga, A., Hong, S., Cozzi, G., Gaspari, V., Planchon, F. A. M., Cairns, W., Ferrari, C., Crutzen, P., Cescon, P., and Boutron, C. F. (2004). Meteoric smoke fallout over the Holocene epoch revealed by iridium and platinum in Greenland ice. *Nature*, 432:1011–1014.

Gardner, C. S., Liu, A. Z., Marsh, D. R., Feng, W., and Plane, J. M. C. (2014). Inferring the global cosmic dust influx to the Earth's atmosphere from lidar observations of the vertical flux of mesospheric Na. *J. Geophys. Res.-Space.*, 119(9):7870–7879.

Gelinas, L. J., Lynch, K. A., Kelley, M. C., Collins, S., Baker, S., Zhou, Q., and Friedman, J. S. (1998). First observation of meteoric charged dust in the tropical mesosphere. *Geophys. Res. Lett.*, 25:4047–4050.

Goertz, C. K. (1989). Dusty Plasmas in the Solar System. *Rev. Geophys.*, 27:271–292.

Gordley, L. L., Hervig, M. E., Fish, C., III, J. M. R., Bailey, S., Cook, J., Hansen, S., Shumway, A., Paxton, G., Deaver, L., Marshall, T., Burton, J., Magill, B., Brown, C., Thompson, E., and Kemp, J. (2009). The solar occultation for ice experiment. *J. Atmos. Sol.-Terr. Phys.*, 71(3â€“4):300 – 315.

Gumbel, J., Fan, Z. Y., Waldemarsson, T., Stegman, J., Witt, G., Llewellyn, E. J., She, C.-Y., and Plane, J. M. C. (2007). Retrieval of global mesospheric sodium densities from the Odin satellite. *Geophys. Res. Lett.*, 34(4):L04813.

Gumbel, J., Siskind, D. E., Witt, G., Torkar, K. M., and Friedrich, M. (2003). Influences of ice particles on the ion chemistry of the polar summer mesosphere. *J. Geophys. Res.-Atmos.*, 108(D8):8436.

Havnes, O., Gumbel, J., Antonsen, T., Hedin, J., and Hoz, C. L. (2014). On the size distribution of collision fragments of {NLC} dust particles and their relevance to meteoric smoke particles. *J. Atmos. Sol.-Terr. Phys.*, 118, Part B:190 – 198.

Havnes, O., Hoz, C. L., Biebricher, A., Kassa, M., Meseret, T., NÃ¦sheim, I., and Zivkovic, T. (2004). Investigation of the Mesospheric PMSE Conditions by Use of the New Overshoot Effect. *Physica Scripta*, 2004(T107):70.

Havnes, O. and Kassa, M. (2009). On the sizes and observable effects of dust particles in polar mesospheric winter echoes. *J. Geophys. Res.-Atmos.*, 114(D9):D09209.

Havnes, O., La Hoz, C., Rietveld, M. T., Kassa, M., Baroni, G., and Biebricher, A. (2011). Dust charging and density conditions deduced from observations of PMWE modulated by artificial electron heating. *J. Geophys. Res.-Atmos.*, 116:D24203.

Havnes, O., Trøim, J., Blix, T., Mortensen, W., Næsheim, L., Thrane, E., and Tønnesen, T. (1996). First detection of charged dust particles in the Earth's mesosphere. *J. Geophys. Res.*, 101(A5):10839–10847.

Heaviside, O. (1902). *Encyclopaedia Britannica*, volume 33, chapter Theory of Telegraphy, page 213. Encyclopaedia Britannica, Inc., 10 edition.

Hedin, A. E. (1991). Extension of the MSIS thermosphere model into the middle and lower atmosphere. *J. Geophys. Res.-Space.*, 96(A2):1159–1172.

Hedin, J., Giovane, F., Waldemarsson, T., Gumbel, J., Blum, J., Stroud, R. M., Marlin, L., Moser, J., Siskind, D. E., Jansson, K., Saunders, R. W., Summers, M. E., Reissaus, P., Stegman, J., Plane, J. M., and Horanyi, M. (2014). The MAGIC meteoric smoke particle sampler. *J. Atmos. Sol.-Terr. Phys.*, 118, Part B:127 – 144.

Hedin, J., Gumbel, J., and Rapp, M. (2007). On the efficiency of rocket-borne particle detection in the mesosphere. *Atmos. Chem. Phys.*, 7(14):3701–3711.

Hervig, M. E., Deaver, L. E., Bardeen, C. G., Russell III, J. M., Bailey, S. M., and Gordley, L. L. (2012). The content and composition of meteoric smoke in mesospheric ice particles from SOFIE observations. *J. Atmos. Sol.-Terr. Phys.*, 84-85:1–6.

Hervig, M. E., Gordley, L. L., Deaver, L. E., Siskind, D. E., Stevens, M. H., Russell, J. M., Bailey, S. M., Megner, L., and Bardeen, C. G. (2009). First Satellite Observations of Meteoric Smoke in the Middle Atmosphere. *Geophys. Res. Lett.*, 36:L18805.

Hoppel, W. A. and Frick, G. M. (1986). Ion–Aerosol Attachment Coefficients and the Steady-State Charge Distribution on Aerosols in a Bipolar Ion Environment. *Aerosol Sci. Tech.*, 5(1):1–21.

Horanyi, M., Gumbel, J., Witt, G., and Robertson, S. (1999). Simulation of rocket-borne particle measurements in the mesosphere. *Geophys. Res. Lett.*, 26(11):1537–1540.

Horanyi, M., Robertson, S., Smiley, B., Gumbel, J., Witt, G., and Walch, B. (2000). Rocket-borne mesospheric measurement of heavy charge carriers. *Geophys. Res. Lett.*, 26:1537–1540.

Hunten, D. M., Turco, R. P., and Toon, O. B. (1980). Smoke and Dust Particles of Meteoric Origin in the Mesosphere and Stratosphere. *J. Atmos. Sci.*, 37:1342–1357.

Janches, D., Heinselman, C. J., Chau, J. L., Chandran, A., and Woodman, R. (2006). Modeling the global micrometeor input function in the upper atmosphere observed by high power and large aperture radars. *J. Geophys. Res.-Space.*, 111(A7):n/a–n/a.

Jensen, E. J. and Thomas, G. E. (1991). Charging of mesospheric particles: Implications for electron density and particle coagulation. *J. Geophys. Res.-Atmos.*, 96(D10):18603–18615.

Kanaya, K., Ono, S., and Ishigaki, F. (1978). Secondary electron emission from insulators. *J. Phys. D Appl. Phys.*, 11(17):2425.

Katz, I., Mandell, M., Jongeward, G., and Gussenhoven, M. S. (1986). The importance of accurate secondary electron yields in modeling spacecraft charging. *J. Geophys. Res.-Space.*, 91(A12):13739–13744.

Kazil, J. (2002). *The University of Bern Atmospheric Ion Model: Time-dependent ion modeling in the stratosphere, mesosphere, and lower thermosphere.* PhD thesis, University of Bern.

Kazil, J., Kopp, E., Chabrillat, S., and Bishop, J. (2003). The Universiy of Bern Atmospheric Ion Model: Time-dependent modeling of the ions in the mesosphere and lower thermosphere. *J. Geophys. Res.*, 108:4432.

Kennelly, A. E. (1902). On the Elevation of the Electrically-Conducting Strata of the Earth's Atmosphere. *Electrical World and Engineer.*, 39:473.

Kero, A., Enell, C.-F., Kavanagh, A. J., Vierinen, J., Virtanen, I., and Turunen, E. (2008). Could negative ion production explain the polar mesosphere winter echo (PMWE) modulation in active HF heating experiments? *Geophys. Res. Lett.*, 35(23):L23102.

Kirkwood, S., Chilson, P., Belova, E., Dalin, P., Häggström, I., Rietveld, M., and Singer, W. (2006). Infrasound - the cause of strong Polar Mesosphere Winter Echoes? *Ann. Geophys.*, 24(2):475–491.

La Hoz, C. and Havnes, O. (2008). Artificial modification of polar mesospheric winter echoes with an RF heater: Do charged dust particles play an active role? *J. Geophys. Res.-Atmos.*, 113(D19):D19205.

Latteck, R. and Strelnikova, I. (2015). Extended observations of polar mesosphere winter echoes over Andøya (69°N) using MAARSY. *J. Geophys. Res.-Atmos.*, 120(16):8216–8226.

Lau, Y. K., Ikuta, S., and Kebarle, P. (1982). Thermodynamics and kinetics of the gas-phase reactions $H_3O^+(H_2O)_{n-1} + H_2O = H_3O^+(H_2O)_n$. *J. Am. Chem. Soc.*, 104(6):1462–1469.

Love, S. and Brownlee, D. (1993). A Direct Measurement of the Terrestrial Mass Accretion Rate of Cosmic Dust. *Science*, 262:550–553.

Lübken, F.-J., Strelnikov, B., Rapp, M., Singer, W., Latteck, R., Brattli, A., Hoppe, U.-P., and Friedrich, M. (2006). The thermal and dynamical state of the atmosphere during polar mesosphere winter echoes. *Atmos. Chem. Phys.*, 6(1):13–24.

Lynch, K. A., Gelinas, L. J., Kelley, M. C., Collins, R. L., Widholm, M., Rau, D., MacDonald, E., Liu, Y., Ulwick, J., and Mace, P. (2005). Multiple sounding rocket observations of charged dust in the polar winter mesosphere. *J. Geophys. Res.*, 110:A03302.

Marconi, G. (1902). A Note on the Effect of Daylight upon the Propagation of Electromagnetic Impulses over Long Distances. *Proc. R. Soc. Lond.*, 70:344–347.

Marsh, D. R., Janches, D., Feng, W., and Plane, J. M. C. (2013). A global model of meteoric sodium. *J. Geophys. Res.-Atmos.*, 118(19):11,442–11,452.

McKinley, D. W. R. (1961). *Meteor science and engineering.* McGraw-Hill.

Mechtly, E. A., Bowhill, S. A., Smith, L. G., and Knoebel, H. W. (1967). Lower ionosphere electron concentration and collision frequency from rocket measurements of Faraday rotation, differential absorption, and probe current. *J. Geophys. Res.*, 72(21):5239–5245.

Megner, L. and Gumbel, J. (2009). Charged meteoric particles as ice nuclei in the mesosphere: Part 2 A feasibility study. *J. Atmos. Sol.-Terr. Phys.*, 71:1236–1244.

Megner, L., Rapp, M., and Gumbel, J. (2006). Distribution of meteoric smoke - sensitivity to microphysical properties and atmospheric conditions. *Atmos. Chem. Phys.*, 6:4415–4426.

Megner, L., Siskind, D. E., Rapp, M., and Gumbel, J. (2008). Global and temporal distribution of meteoric smoke: A two-dimensional simulation study. *J. Geophys. Res.*, 113:D03202.

Meier, R. (1991). Ultraviolet spectroscopy and remote sensing of the upper atmosphere. *Space Sci. Rev.*, 58(1):1–185.

Meyer-Vernet, N. (1982). Flip-flop of electric potential of dust grains in space. *Astron. Astrophys.*, 105:98–106.

Mitra, A. (1981). Chemistry of middle atmospheric ionization - a review. *J. Atmos. Terr. Phys.*, 43(8):737 – 752.

Miyoshi, Y., Oyama, S., Saito, S., Kurita, S., Fujiwara, H., Kataoka, R., Ebihara, Y., Kletzing, C., Reeves, G., Santolik, O., Clilverd, M., Rodger, C. J., Turunen, E., and Tsuchiya, F. (2015). Energetic electron precipitation associated with pulsating aurora: EISCAT and Van Allen Probe observations. *J. Geophys. Res.-Space.*, 120(4):2754–2766.

Narcisi, R. S. and Bailey, A. D. (1965). Mass spectrometric measurements of positive ions at altitudes from 64 to 112 kilometers. *J. Geophys. Res.*, 70(15):3687–3700.

Natanson, G. L. (1960). On the theory of the charging of atmospheric aerosol particles as a result of capture of gas ions. *Sov. Phys. Tech. Phys.*, 5:538–551.

Neely, R. R., English, J. M., Toon, O. B., Solomon, S., Mills, M., and Thayer, J. P. (2011). Implications of extinction due to meteoritic smoke in the upper stratosphere. *Geophys. Res. Lett.*, 38(24):L24808.

Nicolet, M. and Aikin, A. C. (1960). The formation of the D Region of the Ionosphere. *J. Geophys. Res.*, 65(5):1469–1483.

Nishiyama, T., Sato, K., Nakamura, T., Tsutsumi, M., Sato, T., Kohma, M., Nishimura, K., Tomikawa, Y., Ejiri, M. K., and Tsuda, T. T. (2015). Height and time characteristics of seasonal and diurnal variations in PMWE based on 1 year observations by the PANSY radar(69.0°S, 39.6°E). *Geophys. Res. Lett.*, 42(7):2100–2108.

Opal, C. B., Peterson, W. K., and Beaty, E. C. (1971). Measurements of Secondary Electron Spectra Produced by Electron Impact Ionization of a Number of Simple Gases. *J. Chem. Phys.*, 55(8):4100–4106.

Osepian, A. and Kirkwood, S. (1996). High-energy electron fluxes derived from EISCAT electron density profiles. *J. Atmos. Terr. Phys.*, 58:479–487.

Pavlov, A. (2014). Photochemistry of Ions at D-region Altitudes of the Ionosphere: A Review. *Surv. Geophys.*, 35(2):259–334.

Pfister, W. (1967). Auroral Invesitgations by Means of Rockets. *Space Sci. Rev.*, 7:642–688.

Phelps, A. (1969). Laboratory studies of electron attachment and detachment processes of aeronomic interest. *Can. J. Chem.*, 47(10):1783–1793.

Picone, J. M., Hedin, A. E., Drob, D. P., and Aikin, A. C. (2002). NRLMSISE-00 empirical model of the atmosphere: Statistical comparisons and scientific issues. *J. Geophys. Res.-Space.*, 107(A12):SIA 15–1–SIA 15–16.

Plane, J. M., Saunders, R. W., Hedin, J., Stegman, J., Khaplanov, M., Gumbel, J., Lynch, K. A., Bracikowski, P. J., Gelinas, L. J., Friedrich, M., Blindheim, S., Gausa, M., and Williams, B. P. (2014). A combined rocket-borne and ground-based study of the sodium layer and charged dust in the upper mesosphere. *J. Atmos. Sol.-Terr. Phys.*, 118, Part B(0):151 – 160.

Plane, J. M. C. (2003). Atmospheric Chemistry of Meteoric Metals. *Chem. Rev.*, 103:4963.

Plane, J. M. C. (2004). A time-resolved model of the mesospheric Na layer: constraints on the meteor input function. *Atmos. Chem. Phys.*, 4(3):627–638.

Plane, J. M. C. (2012). Cosmic dust in the Earth's atmosphere. *Chem. Soc. Rev.*, 41:6507–6518.

Plane, J. M. C., Feng, W., and Dawkins, E. C. M. (2015). The Mesosphere and Metals: Chemistry and Changes. *Chem. Rev.*, 115(10):4497–4541.

Plane, J. M. C., Gómez-Martín, J. C., Feng, W., and Janches, D. (2016). Silicon chemistry in the mesosphere and lower thermosphere. *J. Geophys. Res.-Atmos.*, 121(7):3718–3728.

Rapp, M. (2000). Capture rates of electrons and positive ions by mesospheric aerosol particles. *J. Aerosol Sci.*, 31:1367–1369.

Rapp, M. (2009). Charging of mesospheric aerosol particles: the role of photodetachment and photoionization from meteoric smoke and ice particles. *Ann. Geophys.*, 27:2417–2422.

Rapp, M., Hedin, J., Strelnikova, I., Friedrich, M., Gumbel, J., and Lübken, F.-J. (2005). Observations of positively charged nanoparticles in the nighttime polar mesosphere. *Geophys. Res. Lett.*, 32:L223821.

Rapp, M., Latteck, R., Stober, G., Hoffmann, P., Singer, W., and Zecha, M. (2011). First three-dimensional observations of polar mesosphere winter echoes: Resolving space-time ambiguity. *J. Geophys. Res.-Space.*, 116:A11307.

Rapp, M. and Lübken, F.-J. (2001). Modelling of particle charging in the polar summer mesosphere: Part 1-General results. *J. Atmos. Sol.-Terr. Phys.*, 63(8):759–770.

Rapp, M. and Lübken, F.-J. (2004). Polar mesosphere summer echoes (PMSE): Review of observations and current understanding. *Atmos. Chem. Phys.*, 4(11/12):2601–2633.

Rapp, M., Plane, J. M. C., Strelnikov, B., Stober, G., Ernst, S., Hedin, J., Friedrich, M., and Hoppe, U.-P. (2012). In situ observations of meteor smoke particles (MSP) during the Geminids 2010: constraints on MSP size, work function and composition. *Ann. Geophys.*, 30:1661–1673.

Rapp, M. and Strelnikova, I. (2009). Measurements of meteor smoke particles during the ECOMA-2006 campaign: 1. Particle detection by active photoionization. *J. Atmos. Sol. Terr. Phys*, 71:477–485.

Rapp, M., Strelnikova, I., and Gumbel, J. (2007). Meteoric smoke particles: Evidence from rocket and radar techniques. *Adv. Space Res.*, 40:809–817.

Rapp, M., Strelnikova, I., Strelnikov, B., Hoffmann, P., Friedrich, M., Gumbel, J., Megner, L., Hoppe, U.-H., Robertson, S., Knappmiller, S., Wolff, M., and Marsh, D. R. (2010). Rocket-borne in situ measurements of meteor smoke: Charging properties and implications for seasonal variation. *J. Geophys. Res.*, 115:D00I16.

Rapp, M. and Thomas, G. E. (2006). Modeling the microphysics of mesospheric ice particles: Assessment of current capabilities and basic sensitivities. *J. Atmos. Sol.-Terr. Phys.*, 68:715–744.

Rees, M. H. (1969). Auroral electrons. *Space Sci. Rev.*, 10(3):413–441.

Rees, M. H. (1989). *Physics and Chemistry of the Upper Atmosphere*. Cambridge University Press.

Rees, M. H., Stewart, A. I., and Walker, J. C. G. (1969). Secondary electrons in aurora. *Planet. Space Sci.*, 17(12):1997 – 2008.

Reeves, G. D., Spence, H. E., Henderson, M. G., Morley, S. K., Friedel, R. H. W., Funsten, H. O., Baker, D. N., Kanekal, S. G., Blake, J. B., Fennell, J. F., Claudepierre, S. G., Thorne, R. M., Turner, D. L., Kletzing, C. A., Kurth, W. S., Larsen, B. A., and Niehof, J. T. (2013). Electron Acceleration in the Heart of the Van Allen Radiation Belts. *Science*, 341(6149):991–994.

Reid, G. C. (1990). Ice particles and electron "bite-outs" at the summer polar mesopause. *J. Geophys. Res.-Atmos.*, 95(D9):13891–13896.

Rietmeijer, F., Corte, V. D., Ferrari, M., Rotundi, A., and Brunetto, R. (2016). Laboratory analyses of meteoric debris in the upper stratosphere from settling bolide dust clouds. *Icarus*, 266:217 – 234.

Robertson, S., Dickson, S., Horanyi, M., Sternovsky, Z., Friedrich, M., Janchez, D., Megner, L., and Williams, B. (2013). Detection of Meteoric Smoke Particles in the Mesosphere by a Rocket-borne Mass Spectrometer. *J. Atmos. Sol.-Terr. Phys.*, 118:161–179.

Robertson, S., Horanyi, M., Knappmiller, S., Sternovsky, Z., Holzworth, R., Shimogawa, M., Friedrich, M., Torkar, K., Gumbel, J., Megner, L., Baumgarten, G., Latteck, R., Rapp, M., Hoppe, U.-P., and Hervig, M. E. (2009). Mass analysis of charged aerosol particles in NLC and PMSE during the ECOMA/MASS campaign. *Ann. Geophys.*, 27:1213–1232.

Rohatschek, H. and Horvath, H. (2010). Magneto-photophoresis and mesospheric particles. *J. Geophys. Res.-Atmos.*, 115(D24):D24208.

Rosinski, J. and Snow, R. H. (1961). Secondary particulate matter from meteor vapors. *J. Meteorol.*, 18:736–745.

Russell, J. P., Ward, W. E., Lowe, R. P., Roble, R. G., Shepherd, G. G., and Solheim, B. (2005). Atomic oxygen profiles (80 to 115 km) derived from Wind Imaging Interferometer/Upper Atmospheric Research Satellite measurements of the hydroxyl and greenline airglow: Local time–latitude dependence. *J. Geophys. Res.*, 110:D15305.

Russell III, J. M., Bailey, S. M., Gordley, L. L., Rusch, D. W., Horanyil, M., Hervig, M. E., Thomas, G. E., Randall, C. E., Siskind, D. E., Stevens, M. H., Summers, M. E., Taylor, M. J., Englert, C. R., Espy, P. J., McClintock, W. E., and Merkel, A. W. (2009). The Aeronomy of Ice in the Mesosphere (AIM) mission: Overview and early science results . *J. Atmos. Sol.-Terr. Phys.*, 71:289 – 299.

Sander, S. P., Friedl, R. R., Golden, D. M., Kurylo, M. J., Huie, R. E., Orkin, V. L., Moortgat, G. K., Ravishankara, A. R., Kolb, C. E., Molina, M. J., , and Finlayson-Pitts, B. J. (2003). *Chemical Kinetics and Photochemical Data for Use in Stratospheric Modeling: Evaluation number 14*. JPL Publication 02-25, Jet Propulsion Laboratory, California Institute of Technology, Pasadena, USA.

Saunders, R. W. and Plane, J. (2011). A photo-chemical method for the production of olivine nanoparticles as cosmic dust analogues. *Icarus*, 212:373–382.

Saunders, R. W. and Plane, J. M. C. (2006). A laboratory study of meteor smoke analoques: Composition, optical properties and growth kinetics. *J. Atmos. Sol.-Terr. Phys.*, 68:2182–2202.

Schmidt-Ott, A., Schurtenberger, P., and Siegmann, H. C. (1980). Enormous Yield of Photoelectrons from Small Particles. *Phys. Rev. Lett.*, 45:1284–1286.

Schulte, P. and Arnold, F. (1992). Detection of upper atmospheric negatively charged microclusters by a rocket-borne mass spectrometer. *Geophys. Res. Lett.*, 19:2297–2300.

Shimazaki, T. (1971). Effective eddy diffusion coefficient and atmospheric composition in the lower thermosphere. *J. Atmos. Terr. Phys.*, 33(9):1383–1401.

Strelnikova, I. and Rapp, M. (2013). Statistical characteristics of PMWE observations by the EISCAT VHF radar. *Ann. Geophys.*, 31(2):359–375.

Strelnikova, I., Rapp, M., Raizada, S., and Sulzer, M. (2007). Meteor smoke particle properties derived from Arecibo incoherent scatter radar observations. *Geophys. Res. Lett.*, 34:L15815.

Strelnikova, I., Rapp, M., Strelnikov, B., Baumgarten, G., Brattli, A., Svenes, K., Hoppe, U.-P., Friedrich, M., Gumbel, J., and Williams, B. P. (2009). Measurements of meteor smoke particles during the ECOMA-2006 capaign: 2. Results. *J. Atmos. Sol.-Terr. Phys.*, 71:486–496.

Thrane, E. V. and Grandal, B. (1981). Observations of fine scale structure in the mesosphere and lower thermosphere. *J. Atmos. Terr. Phys.*, 43:179–189.

Tobiska, W. K. and Bouwer, S. D. (2006). New developments in SOLAR2000 for space research and operations. *Adv. Space Res.*, 37(2):347 – 358.

Tobiska, W. K., Woods, T., Eparvier, F., Viereck, R., Floyd, L., Bouwer, D., Rottman, G., and White, O. (2000). The SOLAR2000 empirical solar irradiance model and forecast tool. *J. Atmos. Sol.-Terr. Phys.*, 62(14):1233–1250.

Triaud, A. H. (2013). n-k data for Fe_2O_3. Website. http://www.astro.uni-jena.de/Laboratory/OCDB/oxsul.html.

Turunen, E., Matveinen, H., Tolvanen, J., and Ranta, H. (1996). *STEP Handbook of Ionospheric Models*, chapter D-region ion chemistry model, pages 1–25. SCOSTEP Secretariat.

Turunen, E., Verronen, P. T., Seppälä, A., Rodger, C. J., Clilverd, M. A., Tamminen, J., Enell, C.-F., and Ulich, T. (2009). Impact of different energies of precipitating particles on NOx generation in the middle and upper atmosphere during geomagnetic storms. *J. Atmos. Sol.-Terr. Phys.*, 71(10-11):1176 – 1189.

Vardabas, I. M., Carver, J. H., and Taylor, F. W. (1998). The role of water-vapour photodissociation on the formation of a deep minimum in mesopause ozone. *Ann. Geophys.*, 16:189–196.

Verronen, P. T. (2006). *Ionosphere-atmosphere interaction during solar proton events*. PhD thesis, University of Helsinki (Available at http://urn.fi/URN:ISBN:952-10-3111-5).

Verronen, P. T., Seppälä, A., Clilverd, M. A., Rodger, C. J., Kyrölä, E., Enell, C.-F., Ulich, T., and Turunen, E. (2005). Diurnal variation of ozone depletion during the October-November 2003 solar proton events. *J. Geophys. Res.-Space.*, 110(A9):A09S32.

Voigt, C., Schlager, H., Luo, B. P., Dörnbrack, A., Roiger, A., Stock, P., Curtius, J., Vössing, H., Borrmann, S., Davies, S., Konopka, P., Schiller, C., Shur, G., and Peter, T. (2005). Nitric Acid Trihydrate (NAT) formation at low NAT supersaturation in Polar Stratospheric Clouds (PSCs). *Atmos. Chem. Phys.*, 5(5):1371–1380.

Vondrak, T., Plane, J. M. C., Broadley, S., and Janches, D. (2008). A chemical model of meteoric ablation. *Atmos. Chem. Phys.*, 8(23):7015–7031.

Vostrikov, A. and Dubov, D. (2006a). Absolute cross sections of electron attachment to molecular clusters: Part I. Formation of $(CO_2)_N^-$. *Tech. Phys.*, 51(5):540–547.

Vostrikov, A. and Dubov, D. (2006b). Absolute cross sections of electron attachment to molecular clusters. Part II: Formation of $(H_2O)_N^-$, $(N_2O)_N^-$, and $(N_2)_N^-$. *Tech. Phys.*, 51(12):1537–1552.

Walch, B., Horányi, M., and Robertson, S. (1995). Charging of dust grains in plasma with energetic electrons. *Phys. Rev. Lett.*, 75(5):838.

Weigel, R., Volk, C. M., Kandler, K., Hösen, E., Günther, G., Vogel, B., Grooß, J.-U., Khaykin, S., Belyaev, G. V., and Borrmann, S. (2014). Enhancements of the refractory submicron aerosol fraction in the Arctic polar vortex: feature or exception? *Atmos. Chem. Phys.*, 14(22):12319–12342.

Wilms, H., Rapp, M., and Kirsch, A. (2016). Nucleation of mesospheric cloud particles: Sensitivities and limits. *J. Geophys. Res.-Space.*, 121:2621–2644.

Winkler, H., Kazeminejad, S., Sinnhuber, M., Kallenrode, M.-B., and Notholt, J. (2009). Conversion of mesospheric HCl into active chlorine during the solar proton event in July 2000 in the northern polar region. *J. Geophys. Res.-Atmos.*, 114(D1):D00I03.

Wood, D. M. (1981). Classical Size Dependence of the Work Function of Small Metallic Spheres. *Phys. Rev. Lett.*, 46:749–749.

List of Figures

List of Tables

Danksagung

Am Ende möchte ich mich bei den Menschen bedanken, die mit Rat und Tat dazu beigetragen haben, dass diese Arbeit fertig wurde. Das ist zu aller erst Professor Markus Rapp, der meine Arbeit ermöglicht hat. Aber nicht nur das, nach den unzähligen gemeinsamen Unterredungen konnte ich Probleme lösen, von denen ich zunächst dachte, sie seien unlösbar. Ich möchte mich auch bei Professor Jörg Gumbel bedanken, der zugestimmt hat ein Gutachten über diese Arbeit zu erstellen.

For the invaluable support in all situation during my visits at the Sodankylä Geophysical Observatory and help via EMail, Antti Kero deserves my sincere thanks. In addition, I want to thank the persons involved in the SGO-IPA collaboration. This collaboration allowed me to use the SIC model which is the basis of this thesis. These persons are Esa Turunen, Pekka T. Verronen, and Carl-Frederik Enell, thank you very much.

Bei folgenden Menschen möchte ich mich besonders bedanken, denn Sie haben mir geholfen wissenschaftliche Probleme zu lösen. Das sind: Milla Anttila, Ingo Sölch, Greta Stratmann und Henrike Wilms, vielen Dank dafür.

Bei Hans Schlager möchte ich mich bedanken, dass ich Teil seiner Abteilung sein konnte. Bei Tina möchte ich mich für die angenehme Büroatmosphäre bedanken und bei Heinfried für seine Geduld mit mir im Labor. Außerdem möchte ich allen Kollegen der Abteilung danken, insbesondere denen, die regelmäßig mit zum 15:00 Kaffee gekommen sind.

Ein besonderer Dank gilt den Jungs der WG in der Pfundmayerstraße, ohne deren Unterstützung und Verpflegung ich nicht so weit gekommen wäre. Das waren Fabian, Adam und Christian und sind noch Clemens und Flavio, vielen Dank. Ich möchte mich in dem Sinne auch bei Gerrit bedanken.

Zum Schluss möchte mich auch bei meinen Eltern bedanken, deren immerwährende Unterstützung mich bis zum Ende dieser Arbeit getragen hat.